DESIGN OF PROTEIN-NANOMATERIAL HYBRIDS AS TOOLS FOR SENSING, IMAGING AND BIOELECTRONICS

Elena López Martínez

2022

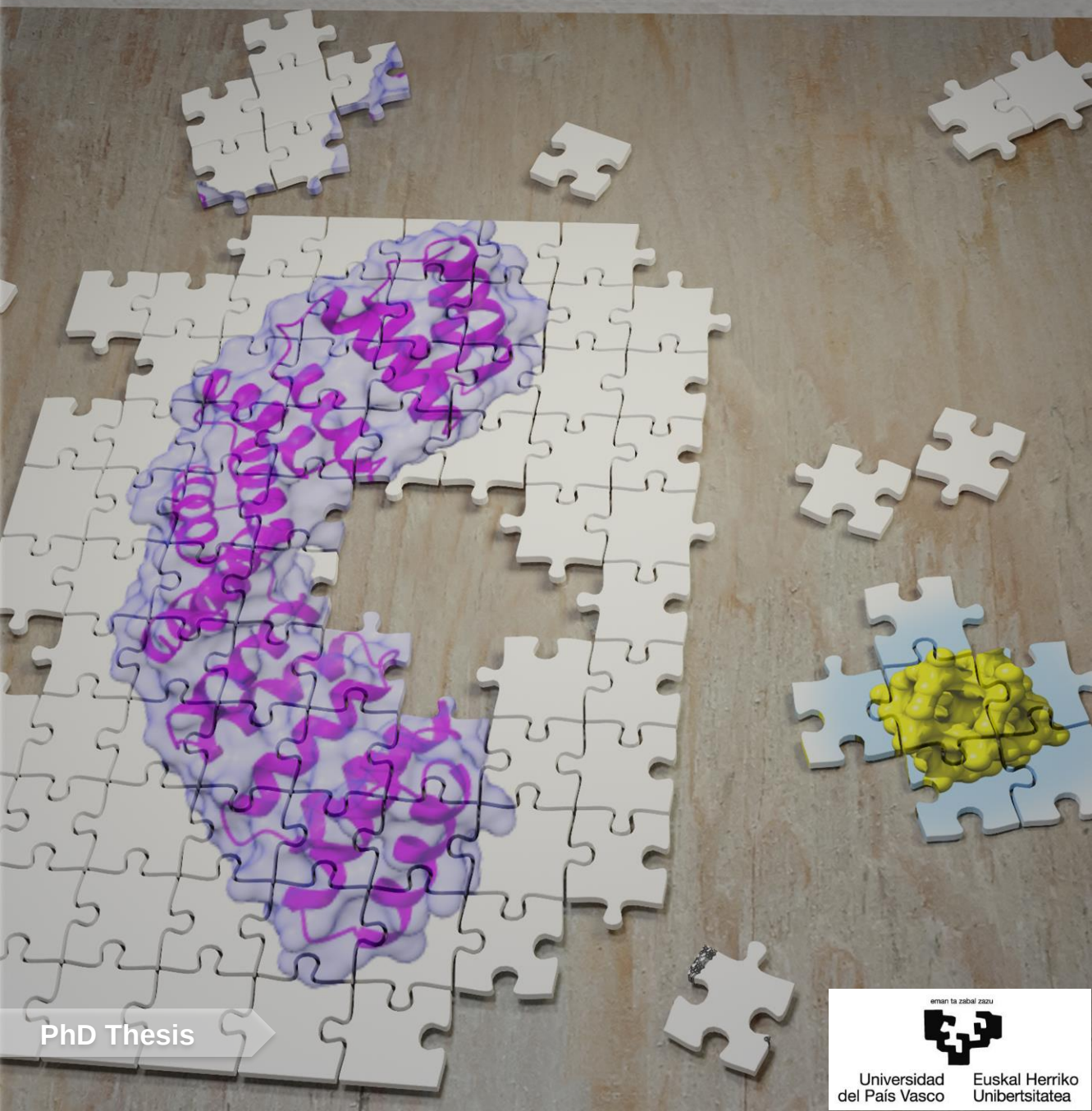

PhD Thesis

eman ta zabal zazu

Universidad del País Vasco

Euskal Herriko Unibertsitatea

DISEÑO DE HÍBRIDOS PROTEÍNA-NANOMATERIAL COMO HERRAMIENTAS PARA SENSÓRICA, IMAGEN Y BIOELECTRÓNICA

Tesis doctoral presentada por:

Elena López Martínez

Para optar al grado de Doctor en Biología Molecular y Biomedicina por la Universidad del País Vasco-Euskal Herriko Unibertsitatea

Tesis dirigida por:

Prof. Aitziber L. Cortajarena

Dr. Carlos Sanchez-Cano

Donostia - San Sebastián, Marzo 2022

eman ta zabal zazu

Universidad del País Vasco Euskal Herriko Unibertsitatea

DESIGN OF PROTEIN-NANOMATERIAL HYBRIDS AS TOOLS FOR SENSING, IMAGING AND BIOELECTRONICS

Ph.D. Thesis presented by

Elena López Martínez

For the degree of Doctor in Molecular Biology and Biomedicine by
Universidad del País Vasco-Euskal Herriko Unibertsitatea

Thesis supervisors:

Prof. Aitziber L. Cortajarena

Dr. Carlos Sanchez-Cano

Donostia - San Sebastián, March 2022

eman ta zabal zazu
Universidad del País Vasco
Euskal Herriko Unibertsitatea

FUNDING AGENCIES

This thesis work was funded by the Spanish Ministry of Science and Innovation (BES-2017-079646), the grant MDM-2017-0720 funded by MCIN/AEI/ 10.13039/501100011033, and the European Research Council grants ERC-CoG-648071-ProNANO and ERC-PoC-841063-NIMM.

LIST OF PUBLICATIONS

1) Tuning the optical properties of Au nanoclusters by designed proteins. **E. Lopez-Martinez***, D. Gianolio, S. Garcia-Orrit, V. Vega-Mayoral, J. Cabanillas-Gonzalez, C. Sanchez-Cano, A.L. Cortajarena. *Adv. Optical Mater*. 2022, 10, 2101332.

2) Sensors based on metal nanoclusters stabilized on designed proteins. A. Aires, **E. Lopez-Martinez***, A.L. Cortajarena. *Biosensors* 2018, 8, 110.

3) Engineering multifunctional metal/protein hybrid nanomaterials as tools for therapeutic intervention and high-sensitivity detection. A. Aires, D. Maestro, A.R. Palanca, **E. Lopez-Martinez**, I. Llarena, K. Geraki, C. Sanchez-Cano, A.V. Villar, A.L. Cortajarena. *Chem. Sci.*, 2021, 12, 2480-2487

4) Engineering conductive protein films through nanoscale self-assembly and gold nanoparticles doping. S.H. Mejias, **E. Lopez-Martinez***, M. Fernandez, P. Couleaud, A. Martin-Lasanta, D. Romera, A. Sanchez-Iglesias, M. R. Osorio, J.M. Abad, M.T. Gonzalez, A.L. Cortajarena. *Nanoscale*, 2021,13, 6772-6779

5) Biomarker sensing platforms based on fluorescent metal nanoclusters. M.V. Romeo, **E. Lopez-Martinez***, J. Berganza-Granda, F. Goñi-de-Cerio, A.L. Cortajarena. *Nanoscale Adv.*, 2021, 3, 1331-1341. Review.

6) Engineered protein hybrids open new horizons as biologic medicines and diagnostic tools. K.B. Uribe, E. Guisasola, A. Aires, **E. Lopez-Martinez**, G. Guedes, I. Saselli, A.L. Cortajarena. *Acc. Chem. Res.* 2021, 54, 22, 4166–4177. Review.

***** First author or first co-author

TABLE OF CONTENTS

RESUMEN

Las proteínas son biomoléculas con una gran diversidad de funciones en la naturaleza. Pueden ser definidas como pequeñas nano-estructuras que trabajan en las células, ya que son una de las soluciones que la evolución ha encontrado para realizar tareas en escalas micro y nanométricas, como transformar materia y energía mediante procesos metabólicos u otorgar de estructura a las células. Son biomoléculas especialmente versátiles, cuya estructura y función suelen encontrarse estrechamente relacionadas.

Por todo ello, los científicos llevan décadas dedicados a diseñar proteínas nuevas y a modificar y mejorar las proteínas ya existentes. Hay varias estrategias que pueden seguirse para ello, como el diseño *de novo*, la miniaturización, el diseño racional o la reutilización de proteínas para usos diversos y diferentes del original. Entre las estrategias de diseño posibles, el uso de pequeñas proteínas modulares se posiciona como una alternativa eficiente y poco costosa para diseñar la nueva generación de herramientas nanotecnológicas. Mediante el diseño modular se pueden combinar proteínas como pequeños bloques de construcción, que además pueden ser modificados y funcionalizados para construir herramientas multifunción, siguiendo el modelo de una navaja suiza.

Las proteínas de repetición son una buena opción para el diseño modular, ya que se trata de un sistema simplificado, basado en módulos pequeños, en el que cada unidad sólo interacciona con los módulos adyacentes. También se pueden insertar, eliminar o reemplazar módulos manteniendo la estructura general de la proteína. Una de las familias de proteínas de repetición más estudiadas son las TPR, del inglés '*tetratricopeptide repeat'*, a partir de las cuales se generó una secuencia consenso (CTPR). Las CTPR tienen características muy interesantes para su uso en ingeniería de

proteínas, ya que de los 34 amino ácidos que forman un módulo CTPR sólo 7 son necesarios para mantener el plegamiento correcto, lo que las hace óptimas para realizar cambios y mutaciones en la secuencia sin alterar la estructura. Además, diferentes módulos se pueden combinar formando una proteína con distintas funcionalidades. Asimismo, las características de las CTPR han permitido que se usen como base para diferentes biomateriales, como films de proteína con propiedades ópticas o actividad enzimática.

Los nanomateriales inorgánicos, como por ejemplo las nanopartículas o los nanocristales fotoluminiscentes, son un avance crítico en el control de la materia en la nano-escala. Desde el comienzo de las ciencias coloidales a finales del siglo XIX, se ha desarrollado una miríada de nanopartículas metálicas con diferentes tamaños, composiciones, formas y propiedades. La composición de los nanomateriales metálicos hace que éstos presenten propiedades interesantes, como por ejemplo electromagnetismo y actividad catalítica. Estos atractivos nanomateriales pueden combinarse con biomoléculas, en particular con proteínas, para diseñar híbridos coloide-biomoleculares, con interesantes propiedades como la fotoluminiscencia, la radiación de calor, la conducción tanto protónica como electrónica, o la actividad catalítica. La parte proteica a su vez otorga estabilidad, controla el crecimiento de cristales metálicos ejerciendo de 'plantilla molecular', puede ser donador o aceptor de energía y reconoce otras biomoléculas de manera específica. Por consiguiente, la combinación de nanoestructuras metálicas y proteínas es una excelente oportunidad para desarrollar biomateriales y nano-herramientas con buena biocompatibilidad. En este sentido, el diseño de proteínas para su conjugación o coordinación con nanoestructuras metálicas tiene objetivos ambiciosos en campos como la biomedicina (combinar terapia y diagnóstico, mejorar formulaciones de medicamentos, realizar nuevas terapias), la óptica (sondas para imagen avanzadas, plasmónica,

sensórica) y el cuidado medioambiental (conversión energética, biorremediación, control de calidad, eficiencia industrial). Por todo ello, la biología molecular, el diseño de proteínas y la nanotecnología abren un nuevo campo en el que las proteínas y los nanomateriales metálicos pueden ser sintéticamente modificados y diseñados para expandir sus funciones y dar solución a problemas en diferentes ámbitos, como por ejemplo el medio ambiente o la biomedicina.

En esta tesis se propone: 1) desarrollar híbridos conjugados de nanomaterial-proteína, empleando la fotoluminiscencia y el carácter metálico de nanoestructuras como las nanopartículas y nanocristales metálicos; 2) diseñar híbridos basados en usar proteínas CTPR modificadas con residuos que coordinan metales para aplicaciones específicas en sensórica, imagen y bioelectrónica. Para cumplir estos dos objeticos generales, esta tesis se divide en 5 capítulos en los que se exploran diferentes usos de los híbridos basados en proteínas CTPR.

En el **primer capítulo** se expone el marco teórico en el que está planteada la tesis. Se establece la importancia de las proteínas, cómo es su estructura y cómo pueden modificarse y funcionalizarse para intentar resolver problemas científico-técnicos. También se explora el mundo de los nanomateriales metálicos y qué relación tiene con las proteínas, tanto en la naturaleza como en el laboratorio. Por último, se detalla el origen, la estructura y las características de las proteínas CTPR, centrándose en su uso como proteína modelo en el desarrollo de nuevos nanomateriales.

En el **segundo capítulo** se explora el diseño de CTPRs para construir híbridos proteína-nanocristal con propiedades luminiscentes. Anteriormente se había descrito el diseño de CTPR para formar nanocristales fotoluminiscentes de oro *in situ*, en el que la proteína actúa de platilla molecular para controlar el crecimiento y estabilización del

nanocristal. Sin embargo, varias preguntas surgen de estos trabajos, siendo la más importante el papel que juega la proteína en la aparición de la fotoluminiscencia. En el capítulo 2 se aborda esta pregunta usando técnicas espectroscópicas avanzadas que permiten conocer el mecanismo fundamental de la emisión de los nanocristales, como la espectroscopía de rayos X basada en radiación sincrotrón y estudios foto-físicos basados en espectroscopía de fotoluminiscencia resuelta en el tiempo. Para ello, se caracterizan nanocristales de oro no fotoluminiscentes conjugados a proteínas CTPR dotadas con diferentes residuos de coordinación metálica. La caracterización permite conocer las propiedades ópticas que emergen de los nanocristales cuando se conjugan a las proteínas mediante los residuos de coordinación apropiados. El trabajo de definir los fundamentos de la fotoemisión en los nanocristales conjugados a proteínas, elaborado en este capítulo, redunda en una mejor comprensión de estos fenómenos fotoluminiscentes, un conocimiento útil para el desarrollo posterior de herramientas basadas en híbridos nanocristal-proteínas.

En el **tercer capítulo** se inspecciona el uso de híbridos nanocristal-proteína como sensores ambientales. En él se explicita el diseño de proteínas CTPR que pueden formar *in situ* nanocristales de oro, plata y cobre y se evalúa su empleo para la detección de cambios en parámetros ambientales como la temperatura, la detección de iones metálicos o la detección de especies reactivas de oxígeno, basado en cambios en su fotoluminiscencia. Entre los tres tipos de nanocristales metálicos empleados, los nanocristales de plata detectaron especies reactivas de oxígeno, los de oro fueron los mejores en la detección de iones metálicos y los tres tipos desempeñaron una detección robusta de la temperatura.

Las capacidades de unión a ligando de las proteínas son un atractivo para aplicaciones biotecnológicas, por lo que en el **cuarto capítulo** se diseñan

y examinan proteínas CTPR con pequeños péptidos añadidos genéticamente que cuentan con propiedades de unión a diferentes estructuras celulares. Si además se agregan módulos de unión a metales al diseño, se pueden desarrollar híbridos proteína-nanocristal con propiedades luminiscentes que pueden usarse como sondas para identificar orgánulos celulares de manera correlativa en microscopía óptica de fluorescencia y en imagen de mapas elementales, como la fluorescencia de rayos-X (XRF). En este capítulo se evalúan diferentes variantes de híbridos nanocristal-CTPR diseñadas para identificar el núcleo, la mitocondria, y el retículo endoplasmático utilizando XRF y microscopía confocal de fluorescencia. Los resultados obtenidos permiten aseverar que los híbridos NC-proteína son, por un lado, detectables en células utilizando XRF, y, por otro lado, que pueden emplearse en microscopía de fluorescencia para identificar orgánulos como las mitocondrias. Aunque los resultados obtenidos son preliminares, son un primer paso para el desarrollo de herramientas de bio-imagen correlativa basada en sondas proteicas diseñadas para tal fin.

El desarrollo histórico de materiales conductores está ligado a los metales. En el **quinto capítulo** se indaga en el diseño de proteínas CTPR para producir biomateriales conductores. Para ello se combinan dos estrategias: la ingeniería de proteínas para conjugar nanopartículas de oro de manera controlada en las proteínas CTPR y el auto-ensamblaje dirigido de las proteínas conjugadas para formar películas proteicas. Este enfoque permite controlar nanométricamente la distribución de las nanopartículas de oro dentro de la película proteica, lo que mejora cuatro órdenes de magnitud la conductividad de este biomaterial.

En conclusión, los estudios realizados en esta tesis son una demostración del empleo sinérgico del diseño de proteínas modulares y la síntesis de

nanoestructuras metálicas para desarrollar nuevas herramientas híbridas con aplicaciones nanotecnológicas en diversos campos.

SUMMARY

Proteins are biomolecules with a huge role diversity in nature. They can be defined as miniature nanostructures working inside cells, since they are one of the solutions that evolution came with for carrying out tasks at micro- and nano-scales, such as matter and energy transformation thought metabolic processes or providing structures to cells. Proteins are especially versatile biomolecules, in which their structure and function are often closely related.

For all this, scientists have been dedicated for decades to design new proteins, as well as modify and improve the already existing ones. There are several strategies that can be followed for protein design, such as de novo design, miniaturization, rational design and protein scaffold repurposing. Among the possible design strategies, the employment of small modular proteins is rising as an efficient and cost-effective alternative to design the next generation of nanotechnological tools. Through modular design, small proteins can be combined as building blocks that can further be modified and functionalized to build multifunctional tools, following a Swiss knife model.

Repeat proteins are a good choice for modular design, since they are a simplified system, based on small building blocks, in which the modules only interact with adjacent ones. Modules can also be inserted, deleted and replaced keeping the overall protein structure. One of the most studied repeat protein families are the tetratricopeptide repeats (TPR), of which a consensus sequence was developed (CTPR). CTPR proteins have interesting features for protein engineering, given that only 7 out of their 34 amino acids per repeat is needed to maintain the correct TPR fold, leaving plenty of space for changes and mutations of the sequence. Besides, modules can be combined, building a protein with different functionalities.

Furthermore, CTPR features have allowed their use as base for different biomaterials, such as protein films with optical properties or enzymatic activity.

Inorganic nanomaterials, such as nanoparticles or photoluminescent nanoclusters, are a critical milestone in the control of matter at the nanoscale. From the begging in of the colloidal sciences at the end of the XIX century, a myriad of nanoparticles with different shapes, sizes, compositions and properties have been developed. The composition of metallic nanomaterials provides interesting properties, such as electromagnetism or catalytic reactivity. These attractive nanomaterials can be combined with biomolecules, particularly proteins, to design colloidal-biomolecular hybrids with interesting properties such as photoluminescence, heat radiation, electronic and protonic conduction or catalytic activity. The protein half confers stability, templates the nanocluster growth, can be an energy donor or acceptor and specifically recognizes other biomolecules. Therefore, the combination of metallic nanostructures and proteins is an excellent opportunity to develop biomaterials and nano-tools with good biocompatibility. In this sense, protein design for conjugation or coordination of metallic nanostructures has ambitious objectives in fields such as biomedicine (theranostics, drug-delivery, new therapies), optics (advanced imaging probes, plasmonics, sensing), and environmental care (energy conversion, bioremediation, quality control, industrial efficiency). For these reasons, molecular biology, protein design and nanotechnology open a new field in which proteins and metallic nanomaterials can be synthetically modified and design to expand their functions and resolve problems in different scenarios, from environmental care to biomedicine.

This thesis work proposes two main objectives: 1) developing conjugated hybrids protein-nanomaterial, employing the photoluminescence and metallic character from nanostructures such as nanoparticles and metal nanocluster; 2) design hybrids based on engineered CTPR modified with metal-coordinating residues for tailored applications in sensing, imaging and bioelectronics. In order to achieve these two objectives, this thesis work is divided in 5 chapters in which different uses for hybrid CTPR protein-nanomaterials are explored.

In the **first chapter** the theoretical background in which this thesis lies is exposed. The importance of proteins, how it is their structure, and how can be further modified and functionalized to solve scientific-technical problems is established. The world of metallic nanomaterials and their relationship with proteins, both in nature and in the laboratory, is also explored. Finally, the origin, structure and features of CTPR protein are detailed, focusing on their role as a protein model to develop novel nanomaterials.

In the **second chapter**, CTPR protein design to build protein-nanocluster hybrids with photoluminescent properties is explored. CTPR protein design for *in situ* growing photoluminescent gold nanoclusters was previously described, in which the protein templates the nanocluster and stabilizes it once it is formed. However, several questions arise here, the most important of them being the role that the protein plays in the photoluminescent appearance. In chapter 2, this question is tackled using advanced spectroscopic techniques that deep in the fundamental mechanism of photoemission in nanoclusters, such as synchrotron-based X ray spectroscopy and photophysical studies based on time-resolved photoluminescent spectroscopy. Toward this aim, non-photoluminescent gold nanoclusters conjugated to CTPR proteins with different metal coordinating residues are characterized. The characterization allows to understand and tune the optical properties arising when the nanoclusters

are conjugated to the proteins by means of the correct choice of coordination residues. The work developed in this chapter, results in a better understanding of photoluminescent phenomena in protein-nanocluster hybrids, a valuable knowledge for further develop of hybrid-based tools.

In the **third chapter**, the use of nanocrystal-protein hybrids as environmental sensors is inspected. Here, the design of CTPR proteins that stabilize gold, silver and copper nanocrystals *in situ* is described, and their use for the detection of changes in environmental parameters such as temperature, detection of metal ions or detection of reactive species of oxygen is evaluated based on changes in their photoluminescence. Among the three types of metal nanocrystals employed, silver nanocrystals detected reactive oxygen species, gold nanocrystals were the best at metal ion detection, and all three types performed robust temperature sensing.

The ligand-binding capabilities of proteins are attractive for biotechnological applications, so in the **fourth chapter**, CTPR proteins with genetically added small peptides different cellular structures binding capabilities are designed and examined. If metal-binding modules are also added to the design, protein-nanocrystal hybrids with luminescent properties can be developed and used as probes to identify cellular organelles in correlative fluorescence light microscopy and elemental map imaging, such as X-ray fluorescence. (XRF). In this chapter, different variants of nanocrystal-CTPR hybrids designed to identify the nucleus, mitochondria, and endoplasmic reticulum are evaluated using XRF and confocal fluorescence microscopy. The results obtained show that NC-protein hybrids are detectable inside cells using XRF and they can be employed in fluorescence microscopy to identify organelles such as the mitochondria. Although the results obtained

are preliminary, they are a first step for the development of correlative bioimaging tools based on protein probes designed for this purpose.

The historical development of conductive materials is linked to metals. The **fifth chapter** investigates the design of CTPR proteins to produce conductive biomaterials. Two strategies are combined for this: protein engineering to conjugate gold nanoparticles in a controlled way to CTPR proteins, and directed self-assembly of the conjugated proteins to form protein films. This approach allows nanometric control of the distribution of gold nanoparticles within the protein film, which improves the conductivity of this biomaterial by four orders of magnitude.

In conclusion, the studies carried out in this thesis are a demonstration of the synergistic use of modular protein design and the synthesis of metallic nanostructures to develop new hybrid tools with nanotechnological applications in several fields.

1.INTRODUCTION

1.1. Proteins get it done: the elegant evolution solution for working at the nanoscale

All known living organisms are made of cells, the basic unit of life, which are self-standing and auto-organized identities. In general, cells have three main needs:

1. Infrastructure, to have compartments in their cellular interior that can sustain different chemical environments.
2. Information management, for organizing, replicating, and transmitting heritable and non-heritable information.
3. Communication, within themselves and the environment for resource exploitation, survival, and cooperative behavior, which can be compared with work in a physical sense.

Although many biomolecules can perform several of these roles, generally speaking, different types of biomolecules have become specialized in each need: nucleic acids store and encode genetic information, lipids compose the lipidic bilayer of biological membranes which allows compartmentalization, and proteins are the biomolecular machines that perform work in cells, for instance in metabolic networks converting matter and energy into useful supplies for cells. Evolution through natural selection is the mechanism that provokes the shape and function of living matter. In particular, for cells and their components, evolution is to blame for the structure and machinery, shaping biomolecules under selective pressure for millions of years[1]. Thus, proteins are a solution that evolution came with for working, storing, managing waste and toxins, moving, signaling, and interacting with the inner cell and outer environment.

Proteins are a type of biopolymers formed by monomers called amino acids. Amino acids assemble in an array, forming a polypeptide chain. There are

20 natural amino acids encoded directly in the universal genetic code, which are called canonical amino acids (Figure 1.1), that take part in polypeptide chains, each one of them with particular features that allow interactions with other molecules and with the other amino acids in the polypeptide chain in order to fold properly into a functional protein. Apart from the canonical amino acids, there are other natural amino acids such us selenocysteine and pyrrolysine that can be incorporated in proteins, and others that are not part of proteins, such as the neurotransmitter gamma-aminobutyric acid or GABA, and synthetic ones that can be chemically engineered to add new functionalities not seen in nature[2]. There is usually an intimate relationship between form and function in the world of proteins, so the amino acids that make a protein and its structure determine the protein function. As an example of this delicate relationship, let us look at collagen, a protein composed of a triple helix. The amino acid glycine appears in every three residues, which provides a slight kink that favors a rope-like triple-helical conformation. This particularity stands for collagen robustness, stiffness, and flexibility, all critical features for its structural function in animal organisms. However, this rule is not followed by intrinsically disordered proteins (IDP) and prions, which are proteins without a defined structure. Although their biological role is still under discussion, some of them present transient shapes, which could function as reversible signaling messengers in cells [3,4].

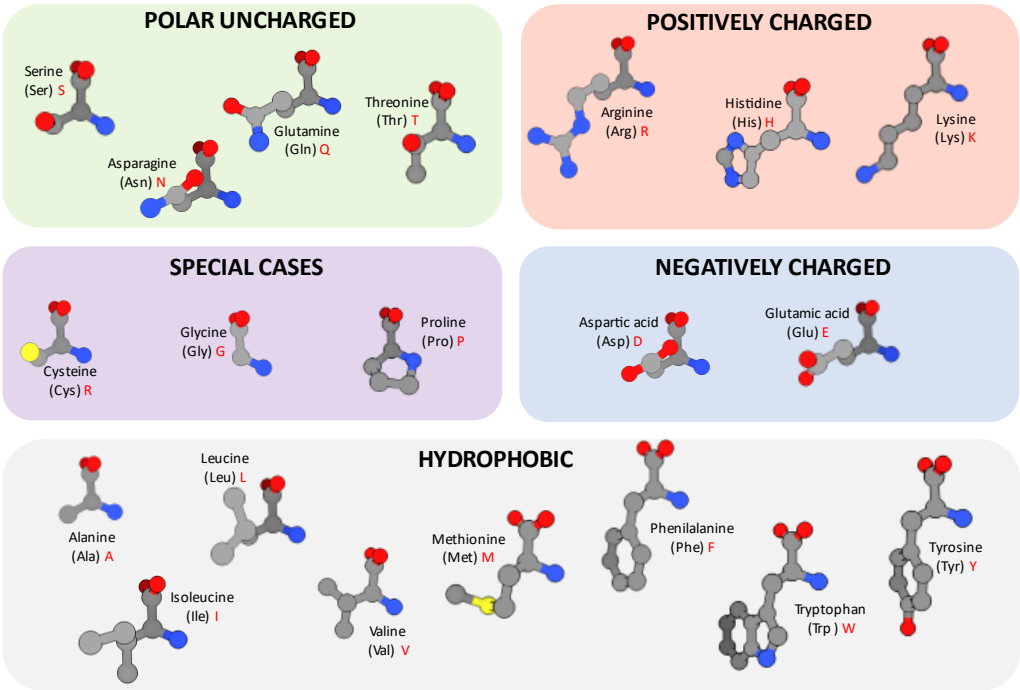

Figure 1.1. Canonical amino acids. Scheme with the canonical amino acids, classified by the charge of their side chains.

Natural proteins are a marvelous source of inspiration for biotechnologists, since they are nanometric tools that can be studied, redesign, and tinkered in order to extend their original functions or completely repurpose them. It is important to take in account the significant role of molecular forces on the protein folding and their function, such as attraction and repulsion forces (Van der Waals, steric repulsion, or hydrogen bonds)[5]. (Figure 1.2).The aqueous medium in which living matter develops is also influential, since water interaction with biomolecules is a driving force of the assembly of many cell components and the formation of different shapes and assemblies, such as globular proteins or biological membranes[6]. Moreover, water molecules can actively participate in long-range water-mediated contacts and dominate the dynamics of biomolecules[7,8].

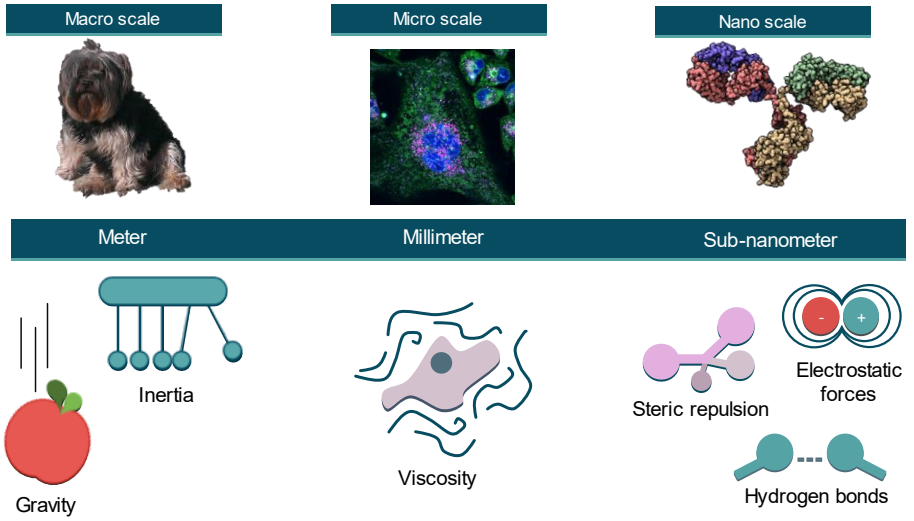

Figure 1.2. Forces at different scales. Upper: a dog, a fluorescence image of a HeLa cell and a molecular model of immunoglobulin G (IgG), correspond to objects in different size scales. All forces shape matter at these scales, nonetheless, each scale is dominated by a predominant type of forces, such as gravity and inertia in the macro scale, viscosity at the microscale, and molecular repulsion and attraction forces in the sub-nanometer scale.

In conclusion, proteins are versatile biomolecules shaped through evolution to become the best candidates among biomolecular plans for being the main workhorse in the nanoscale. Proteins get the cell work done, indeed.

1.2. Hybrid nanomachines: proteins conjugate inorganic molecules in nature.

The chemistry of life is based primarily on carbon, nitrogen, oxygen, phosphorus, hydrogen, and sulfur. However, cells often need other elements to work correctly, some of them as prevalent as calcium or sodium

or as scarce as molybdenum or selenium. For example, calcium is an essential element for a myriad of biological functions, from the assembly of nanostructures that give rise to several cellular architectures (such as the carbonate structure of diatoms), to being involved in its cationic form in many critical physiological processes (like muscular movement). Other examples of cornerstone elements are sodium and potassium, whose concentrations inside and outside the cell constitute the basis for keeping an electric potential across biological membranes.

The mechanism in which two molecules (one of them being a biomolecule) are linked is called bioconjugation. There are many other examples of bioconjugates in living organisms. Magnetostatic bacteria, for example, produce magnetic nanoparticles using protein templates for orienting themselves along Earth's magnetic field[9]. Other natural composites, such as bone or nacre, emerged from self-assembly mechanisms and hierarchical organization of proteins with inorganic nanostructures[10]. The wide variety of architectural motifs and functions derived from proteins combined with inorganic molecules serves as awe-inspiring examples of complex natural assemblies (Figure 1.3).

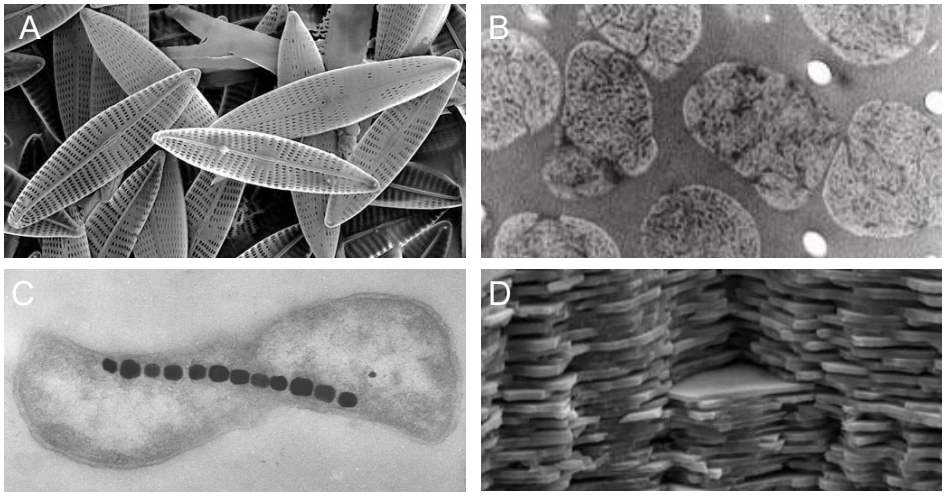

Figure 1.3. Structural diversity from bioconjugate inorganic-organic assemblies. A) Diatom shells are composed of silica, polysaccharides, and proteins such as silaffins, which have a crucial role in the biomineralization process of these microscopic algae. B) Granules from mussel byssi are composed of proteins containing DOPA groups that coordinate iron and vanadium, conferring the outstanding anchoring properties to mussels. C) The magnetostatic bacteria *Magnetospirillium magneticum* forms magnetite crystals inside membranous organelles (magnetosomes) that orient them in geomagnetic fields. D) Mollusca nacre comprises aragonite platelets interdigitated with elastic proteins like lustrin. This assembly makes the material resilient and robust.

1.3. On the importance of metals in biology: natural and artificial metalloproteins.

Among the trace elements mentioned before, metals are a fascinating and commonly occurrent group that is essential to perform structural and precise chemical work within living organisms (Figure 1.4). Proteins often present amino acids with specific chemical groups to coordinate and

interact with metals located in structural pockets[11,12]. In particular, enzymes are a type of proteins involved in performing chemical work, and often, enzymes require other elements (i.e., inorganic cofactors) for correct functioning. For example, iron-sulfur clusters are necessary for the redox reactions that permit the electron transfer in mitochondria and chloroplasts, and require being deeply buried in the protein to avoid interaction with the aqueous medium[13]. Enzymes that present metal ions as cofactors are called metalloenzymes, and in general, proteins that bind metals are so-called metalloproteins.

Natural proteins can bind to different metallic elements, such as zinc, iron, copper, cobalt, magnesium, or nickel[14]. Biological functions carried out by metalloproteins depend on the correct choice of metal, the number of metallic atoms and its geometry, as well as the ligands that coordinate it into the protein core (the so-called first sphere of coordination) while the surrounding protein residues that fine-tune the environment around the metal center configure the second coordination sphere[15], that expand on functional capabilities such as redox potential, pH sensitivity or charge distribution. Among the functions native metalloproteins perform both *in vivo* as well as *in vitro* are hydrolysis, oxidoreduction, peroxidation, or reduction (among other catalytic activities) of metabolic substrates, as well as gene management and expression. Remarkably, molecular biology combined with physicochemical nanoscience open a new field in which proteins and inorganic nanocomposites can be synthetically engineered to expand new functions and fulfill old and novel needs alike.

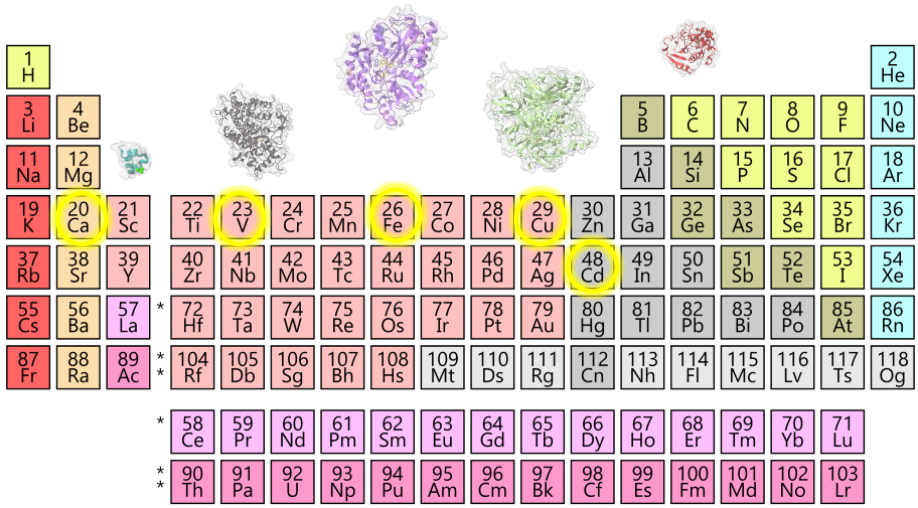

Figure 1.4. Proteins coordinating metals. Proteins can coordinate different metals such as Ca in calcite in the case of osteocalcin (blue protein), V in the case of vanadium peroxidase (grey), Fe for the formation of magnetosomes by MamC (purple), ceruloplasmin coordinates Cu (green protein), and sea algae use Cd with cadmium carbonic anhydrase (red protein).

Putting proteins aside, the development of metallic nanocomponents has been a critical milestone in controlling matter at the nanoscale. Since the beginning of colloidal science, originated from the studies on the interaction of gold nanoparticles with light carried out by Michael Faraday[16], a plethora of metal nanoparticles with different metallic compositions [17], shapes[18,19], sizes[20], and properties[17,21,22] have been developed. Metals and metallic derivatives stand as an important source of physicochemical reactivities and phenomena, in the form of catalysis or a wide range of electromagnetic properties. Moreover, these attractive nanomaterials can be combined with biomolecules, particularly metalloproteins, to design hybrid colloidal-biological molecules with properties given by the metallic nanocomponent, such as photoluminescence, heat radiation, electronic or protonic

conduction, magnetism, plasmonic resonance, or catalytic activity. In contrast, the protein can act as a template, tune the growth of the metallic crystal, recognize other biomolecules or take an active role as donor or acceptor of energy (photons if the protein is photoreactive, or electrons if it has catalytic or conductive properties). Thus, combining both the inorganic and protein elements in the design of biomaterials is an excellent opportunity to establish new nanotechnology with enhanced biocompatibility. In this sense, careful protein design for metal coordination or conjugation is becoming an exciting activity, with ambitious objectives in socially-impacted fields such as biomedicine (drug-delivery[23], theranostic[24], therapy[25]), optics (improved imaging techniques[26], plasmonics[27], sensing[22]) and environmental care (energy conversion[28], bioremediation[29], quality control[30], industrial efficiency[31]).

Inorganic nanomaterials are not the only engineerable objects in the nanoscale. Molecular biology and biophysics have made possible to not only rely on natural proteins, but also design them. Scientists have made use of several strategies for the design of metalloproteins. *De novo* design is one of the most common strategies followed[32,33], in which a protein is constructed from scratch using computational or first-principles approaches. However, it is a time-consuming strategy and challenging to implement in complex proteins, especially when tackling protein stability or allosteric functions[34]. Nature has been an excellent source of inspiration for developing artificial metalloproteins, so the redesign of native protein scaffolds is another exciting strategy that highly constricts the degrees of freedom, setting a more approachable option. For example, ferritin is a natural protein implicated in the transport and storage of iron[35] but has been redesigned to bind other metals and thus be a biomolecular template for the growth of metallic nanoparticles[36,37]. Natural scaffold redesign is a safe option when exploring the stability constraints, since some particular

structures seem to have a higher tolerance to mutations without changing their fold, which could explain their ubiquity across protein families with diverse functions and origins[38,39]. This approach has been used for developing multiple metalloprotein functions, such as storage and transport[40], sensing[41], or catalysis[42,43]. Another exciting strategy consists of miniaturizing the protein system[44], since simplifying the protein scaffold aids in the protein fold and stability, a strategy that has been implemented, for example, in the design of iron-sulfur metalloproteins[45]. Furthermore, combining these design approaches with other techniques, such as molecular biology and chemical biology, allows site-directed mutagenesis to introduce non-natural or non-coded amino acids and to use non-native metal choices, enlarging the repertoire of natural functions[46,47]. For example, a zinc finger protein with a non-canonical citrulline that modifies its avidity for A-T base pairs[48], or the modification of heme groups in myoglobin for the degradation of industrial dyes[49].

The metallic nature of metalloproteins also bears advantages in their characterization. Characterizing the metal part of metalloproteins is crucial in a goal-oriented protein engineering process. The protein engineer must direct their efforts towards the metal center and the coordination spheres to develop a functional protein that meets the requirements imposed in the design process[38,50,51]. Several metal-based spectroscopic and imaging techniques can be used, such as XPS, ICP, XRF, or XAS[52,53]. The combination of these techniques provides information about the elemental composition, amount, localization, and chemical species determination of metals inside a biological sample, such as cells.

Other aspects related to the size and nature of proteins have to be considered when approaching protein design. A protein has different structural conformations, and significant thermal fluctuations or signals from the immediate environment direct the switching between those structural

conformations (for example the conformational changes upon ligand binding). However, proteins have to be sufficiently robust to maintain its integrity and structure when enduring the average thermal fluctuations of its medium. In general, and always dependent of their biological role, proteins need intrinsic stabilization via residue contacts, but not as many that they cannot switch between conformations. The hydrophobic effect plays a significant role in providing internal stabilization, directing the organization of the water molecules towards the hydrophilic residues and relegating the hydrophobic residues to the core of the protein, driving the protein folding[54].

Currently, one of the main problems in the protein field is the so-called protein folding problem[55], which questions first how an amino acid sequence encodes a specific 3D conformation among all the possible conformations, and second, how proteins fold so quickly (usually from microseconds to seconds[56–58]). The concept of the folding funnel[59,60] or its more modern form, the folding energy landscape[61], visually explores the conformational kinetic pathways that a polypeptide chain navigates to fold in a particular structure or the energetic barriers present between the possible structural conformations. Some conformations are preferred because they have an energy minimum, which appears in the energy landscape as a pit or funnel. Using computational methods for defining folding funnels and optimizing those conformational pathways has proved helpful in the *de novo* design of protein sequences[62]. In the near future, the possibilities of designing proteins may expand immensely as the protein folding problem is tackled with the help of artificial intelligence (AI) and machine learning (ML). For example, several neural networks trained with the protein structures deposited in the Protein Data Bank (PDB)[63] can now predict the structure that a particular amino acid sequence will yield[64,65]. As these computational technologies further develop in the future, the design

of proteins based on AI or ML-suggested folds and sequences would be an exciting new venue for biotechnologists working across all fields[66–68].

The new takes on protein engineering with computational power are promising and have already yielded thrilling protein designs; however, ditching *de novo* design and focusing on more accessible approaches can be genuinely beneficial in cost and efficiency. The use of small protein modules arises as a more straightforward and reachable alternative for designing the next generation of protein tools. Modularity has been widely used in many engineering fields as an intelligent strategy to make complex systems manageable and decrease production costs[69], also appearing in natural protein assemblies for the same reasons (i.e., viral capsids[70], RNA binding proteins[71], or enzymes[72]). With a modular approach, small protein building blocks can be tinkered, combined, and functionalized to develop different protein tools.

Repeat tandem proteins appear in genomes due to episodes of genetic duplications, in which the segments can later diverge to accommodate new functions[73] (Figure 1.5). Repeated domains are observed in 50% of proteins, with a much higher occurrence in eukaryotes[74]. This natural phenomenon can be replicated synthetically to design repeat tandem proteins. Consensus protein design has been helpful for the design of repeat proteins[75]. In this approach, the sequence alignment allows identifying the conserved amino acids and the space between them that define the fold. This technique has the advantage of quick identification of beneficial mutations; however, it can be difficult to avoid the phylogenetic bias accompanying evolution and the diversity of that particular set of homologous proteins[76]. One of the most critical advantages is that modules in repeat proteins interact only with their neighboring repeats in the protein array, narrowing the complexity of the long-range contacts that contributes to define the fold in globular proteins. Moreover, repeat units can be

inserted, deleted, or replaced with other units, and the overall protein structure will be maintained as long as the units interact by compatible interfaces between them. In particular, designed repeat proteins appear as an exciting choice to display custom metal coordination sites.

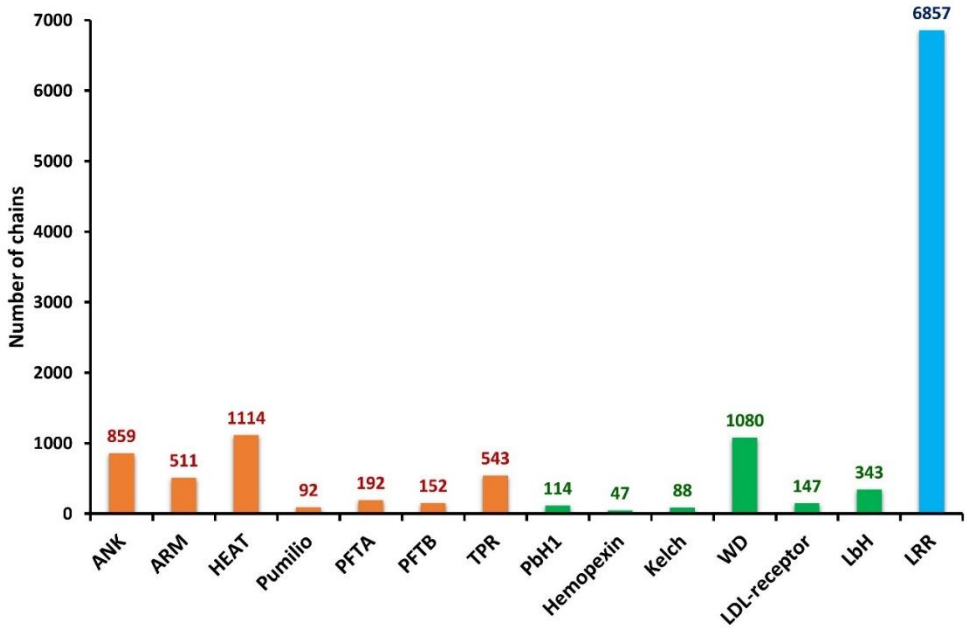

Figure 1.5. Repeat protein families. The number of annotated chains within the Known Protein Repeat Families group, the abbreviations correspond to the structural repeat motifs named, from left to right: ankyrin (ANK), armadillo (ARM), HEAT, pumilio, protein prenyltransferase alpha subunit (PFTA), protein prenyltransferase beta subunit (PFTB), tetratricopeptide repeat (TPR), parallel beta-helix 1 (PBH1), hemopexin-like repeats (Hemopexin), Kelch repeat (Kelch), WD-40 or beta-transducin (WD), low-density-lipoprotein receptor (LDL-receptor), left-handed beta-helix (LbH), leucine-rich repeats (LRR). Taken from the Database of Structural Repeats in Proteins or DbStRiPs [77] (https://bioinf.iiit.ac.in/dbstrips/stats.html).

Several well-known repeat protein families have been engineered using the consensus protein design approach, such as ankyrins (ANK)[78], armadillo repeats (ARM)[79,80], leucine-rich repeats (LRR)[81], or tetratricopeptide repeats (TPR)[75] (Figure 1.6). The latter presents a robust protein scaffold and interesting features for protein modification, thus being an exceptional choice for protein engineering without the cumbersome protein stability problem discussed before.

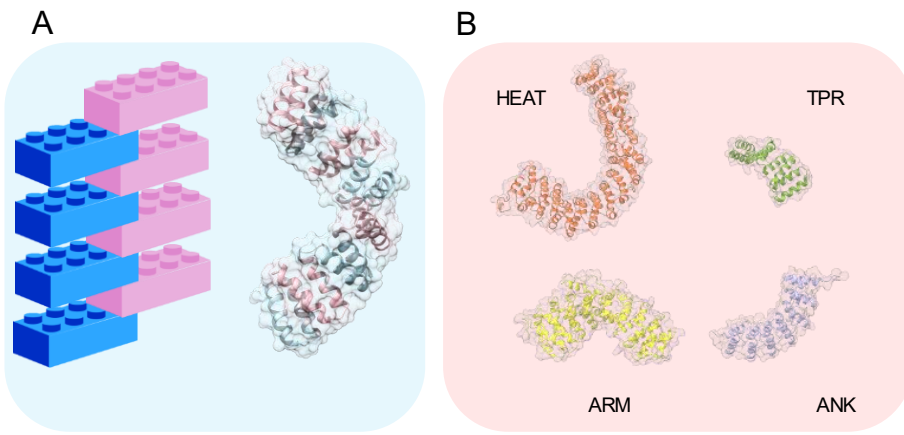

Figure 1.6. **Repeat protein scaffolds.** A) Repeat proteins are arrays of building blocks with the same motif repeated, similar to Lego blocks assemblies. B) some of the most common repeat motifs in nature are HEAT repeats (orange), TPR repeats (green), Armadillo repeats (yellow), and ankyrin repeats (blue).

1.4. CTPR proteins as an ideal model for protein tinkering.

CTPR (consensus tetratricopeptide repeat) are small repeat proteins designed from the alignment of sequences from the TPR (tetratricopeptide repeat) family. The TPR structural motif is a well-established protein fold

consisting of 34 amino acids in which only seven residues hold the key to maintaining the chain's helix-turn-helix identity, forming a completed α-solenoid when the array has eight repeats. The TPR family is implicated in protein-protein interactions, serving as natural scaffolds that guide interactions between different protein domains. For example, the Hsp70/Hsp90 organizing protein (Hop) carries three TPR domains with 3 repeats each, one of which binds the C-terminal region of Hsp70 while the other TPR domain binds the C-terminal of the Hsp90 protein[82]. Other proteins that carry natural TPR domains in their structures are nucleoprotein TPR (a component of the nuclear pore complex) or even sensing proteins on charge of bacterial immunity[83].

The consensus TPR sequence obtained is an ideal building block that can be genetically combined in tandem to establish arrays with a superhelical structure, forming a CTPRn in which n stands for the number of repeats in a given array. The TPR fold in CTPR proteins is maintained by the action of 8 conserved hydrophobic residues involved in the inter- and intra-repeat interactions that give rise to the overall protein structure. This aspect opens the door for virtually substituting the other non-conserved 26 amino acids in the CTPR sequence, which in combination with the possibility of modifying each of the repeats in the CTPRn array unveils a perfect opportunity for designing novel functionalities and ligand-binding capabilities in an engineered protein platform, while maintaining a predictable and stable protein fold (Figure 1.7). In fact, this approach has been already employed for the development of different CTPR-based materials, that were bioconjugated with different molecules such as single-wall carbon nanotubes (SWCNTs) or porphyrins[84], as well as the formation of ordered CTPR protein films with optical[85] or enzymatical activity[86].

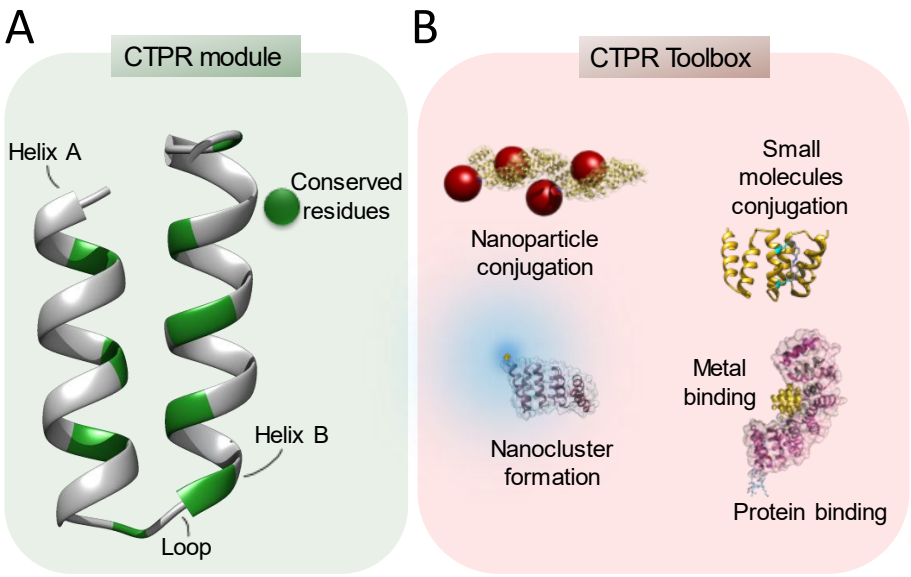

Figure 1.7. CTPR proteins are versatile for different applications. A) CTPR module consists of 34 amino acids forming a helix-turn-helix structure. The conserved residues are shown in green. B) Using CTPR modularity and versatility, we can create a toolbox of different functionalities that can be combined to form tailored bionanomachines.

1.5. General Objectives

Inspired by both natural or synthetic metalloproteins and repeat proteins, this thesis aims to develop hybrid protein-metal conjugates exploiting the photoluminescence and metallic character of metal nanostructures, and apply them in sensing, imaging, and bioelectronics. The design approach uses consensus-designed tetratricopeptide repeats modified with metal coordinating residues. In previous works, engineered CTPR proteins with metal coordinating residues have been thoroughly employed to *in situ* template photoluminescent NCs[87,88] and quantum dots[89]. However, more in-depth work is needed in understanding the physicochemical nature of the

photoluminescence from protein-metal nanoclusters, as well as an exploration of possible applications of such hybrid protein-metal biomaterials. Therefore, the stated hypothesis is that repeat proteins can be finely engineered in conjugation with metal nanoelements for their use in tailored applications. In particular, this thesis work focuses on using CTPR proteins, which are simple modular repeat protein blocks, to coordinate metallic nanoelements such as metal nanoclusters and gold nanoparticles following these objectives:

1. **Design of stable nanocluster-protein hybrids with optimized luminescent properties**. Scaffolding of multiprotein complexes is the most common function of TPR proteins in nature[90]. Since the first design of a consensus TPR (CTPR) sequence, many efforts have been made to explore CTPRs as scaffolds of nanomaterials. Previously, it has been shown that by controlling the self-assembly of CTPR proteins and modifying their sequences, such proteins can be used as templates for metallic nanomaterials[87–89,91–96]. This is an exciting approach to develop biomaterials that hold metal-driven activity, such as catalysis, sensing, conductivity, or fluorescence. In this case, CTPR proteins play a template role in the *in-situ* formation and stabilization of the metal nanoclusters, but little is known about their implication in the nanocrystal formation. Several open questions arise here, such as the contribution of the protein ligand to the emerging optical properties of the nanocluster and the possible coupling between the protein structure and the nanocluster's integrity. One way to tackle this problem is to use the same protein scaffold with different residues in the metal coordination positions. The experiments performed to elucidate the protein role in the emerging photoluminescence from the nanoclusters are developed in Chapter 2.

2. **Design of photoactive nanocluster-protein hybrids that hold a specific environmental-sensing response.** The possibilities of metallic nanoclusters conjugated to CTPR proteins have led us to explore different applications, one of those being the use of the photoluminescence of the nanoclusters for sensing different environmental stimuli, such as temperature, pH, the presence of other metal species, or reactive oxygen species. For this purpose, a CTPR protein with a metal-binding site exposed to the solvent was designed. Several metallic salts were tested for the nucleation of nanoclusters, including silver, copper, and gold. After synthesizing the metal nanocluster, the different protein-metal hybrids were evaluated as sensors through changes in photoluminescence when exposed to differences in temperature, pH, or the presence of molecules. The protein-nanocluster sensors proved useful in the detection of copper, ROS species and temperature changes, as detailed in Chapter 3.
3. **Design of nanoclusters-protein hybrids for cellular and bioimaging applications**. The specific molecular recognition that biomolecules as proteins possess is an attractive feature to explore for bioimaging applications. For that reason, several CTPR proteins have been engineered by adding short peptides to their sequence that hold specific binding or targeting functions with a main objective in mind: design of improved imaging bio-probes for X-Ray Fluorescence and optical microscopy. There is currently a lack of reliable tools to simultaneously image different subcellular structures with precision in X-Ray Fluorescence Nanoprobe. Several approaches have been taken that hold substantial flaws for imaging *in vivo*. This project channels this necessity onto a solution based on an engineered CTPR protein-metal nanocluster hybrid that contains a signal peptide to target a specific organelle structure (*i.e.*, nucleus, endoplasmic reticulum, or mitochondria). CTPR proteins can be used as template scaffolds for the

synthesis of photoluminescent nanoclusters of different non-biological metallic nature (such as Ni, Co, or Au). They could be used to simultaneously probe different organelles and perform correlative imaging between metal-based imaging techniques (such as XRFN) and fluorescence microscopy. This project is extensively detailed and discussed in Chapter 4.

4. **Design of CTPR protein scaffolds as templates for the stabilization and organization of gold nanoparticles to produce electroconductive biomaterials.** Historically, metallic materials have been widely used for electric conductivity. The pursuit of an electroconductive biomaterial has led us to take advantage of the bottom-up approach that CTPR proteins offer, given that CTPR proteins self-assemble forming highly ordered protein films. Thus, doping the protein film with gold nanoparticles could endow electroconductivity properties to a protein-based film. Ordering the gold nanoparticles finely onto the protein film could also enhance the electroconductive efficiency, so a CTPR protein was engineered to finely tune the ordered attachment of 4 gold nanoparticles per protein. This yielded an electroconductive biomaterial, which surprisingly can also have electroconductivity without gold doping. This project is fully discussed in Chapter 5.

2.GENERATION OF LUMINESCENT METAL NANOCLUSTERS ON ENGINEERED PROTEINS

2.1. State of the art

2.1.1. Biomineralization: inorganic materials with biomolecular templating

Biomineralization is the natural process in which living organisms create inorganic structures by assembling inorganic ions, such as Ca, Si or metals, through different biomolecules, including proteins and peptides. Inorganic composites from biological origin, such as nacre or coral reefs, present interesting differences from their non-biosynthesized counterparts (for example, ceramics or concrete). In particular, the complexity and order of bio-composites emerged in the form of super assemblies, and their morphology and size are issues that have attracted the interest of material chemists and biologists alike. The presence of proteins as components of these organic-inorganic biomaterials was the first clue highlighting the key role of biomolecules in such ordered and complex assemblies. In particular, proteins and peptides can direct the controlled growth of inorganic materials in biological organisms.

In a seminal review, Stephen Mann highlighted the importance of molecular recognition in the process of nucleation of inorganic elements within living organisms and envisioned the technological potential derived from understanding and controlling the interactions between biomolecules and inorganic composites[97]. Inspired by nature, one of the first works exploring a controlled biomineralization *in vitro* consisted in the controlled growth of calcite crystals' using a protein extract obtained from sea urchins[98]. This work proved the role of proteins in the spatial regulation and assembly of complex materials, since a distinctive crystal different from the inorganic forms of calcite was formed, as well as the potential benefits of using a simpler and more economic synthesis to generate tailored biomaterials without the burdens derived from working *in vivo* (usually more expensive

and complex, and less scalable protocols). After that, proteins have been considered a powerful biological template for the synthesis of nanocomposites, as shown in the pioneer works using ferritin as a protein cage for the biomineralization of different inorganic materials[99], including iron sulfide[100]. Being ferritin a natural iron-storage protein, it makes a good starting point for developing genetically engineered mutants to synthesize different inorganic structures[101]. Afterwards, the need of finding not only natural metal-binders but also novel engineered metal-binding protein and peptide sequences fueled the expansion of combinatorial approaches in biomimetics, such as peptide display, phage display, and cell-surface display[102–106]. These techniques are used for screening protein or peptide variants looking for the fittest mutant to perform a certain function, in this case, specific metal binding. Such brand-new peptides were genetically fused to cage-shaped proteins to bind and reduce metal ions inside the cavities of the ferritin[101,107]. In addition, other biological 3D assemblies have been used for the templating of complex inorganic structures, such as virus crystals[108], bacterial protein crystals[109], amyloid fibers[110], or virus-based nanowires[111,112].

On top of the metal-binding sequences, the synthesis of inorganic materials using proteins or peptides depends deeply on the metal of choice and the chemistry used to template the metallic nanostructure. Many efforts have been directed towards understanding and emulating biomineralization on proteins, natural or synthetic. In general, the approach for such synthesis consists in the coordination of metal ions on specific residues within the polypeptide chain, and then the reduction of metals using strong reducing agents such as $NaBH_4$[113], NaOH[114], or milder buffer systems[37]. The exquisite molecular recognition given by the diversity of functional groups in amino acids, with the special mention of carboxylic acids, amines, imidazole, phenol, and sulfhydryl groups, makes possible a huge plethora

of metal-binding possibilities. Some of the metals used with this method include Pt[115,116], Pd[108,117], Co[118], Ag[119], Cu[120] and TiO_2[106]; although this thesis will primarily focus on gold nanoclusters (AuNCs).

2.1.2. Metal Nanoclusters

Metal nanoclusters (NCs) are inorganic materials that have been widely used in sensing, biomedicine, and optics due to their interesting physical and chemical characteristics, including their outstanding optical properties. NCs consist of grouped metal atoms confined in a small space, typically below 2 nm in diameter, such that the continuous metallic band disappears and discrete energy levels start to emerge[121]. The nature of the emergent quantum energy levels confers NCs molecule-like properties, responsible for their optical peculiarities, among other characteristics.

NCs can be inorganically synthesized or can be templated by biomolecules. Their shape, structure, and the coordinated ligands determine their features, such as size-dependent photoluminescence (PL)[122]. In this sense, the coordination of NCs with biomolecules is an emerging area of research since such biomolecular capping can endow multiple capabilities to the nanoclusters, including biocompatibility, stability in biological media, and biotic functionality (electron donors or antennas in redox processes[123]), resulting in hybrid bionanomaterials with a plethora of potential applications[124].

2.1.3. Proteins as *in situ* NCs templates

After the pioneer paper of Xie *et al.* describing the first AuNCs grown directed by a protein[114], the most used method for the synthesis of AuNCs on proteins consist in the coordination of Au(III) ions, usually provided in the form of chloroauric acid, on reactive amino acids; followed by the reduction

to Au(0) at a high pH, often adding strong reducing agents as NaOH or $NaBH_4$[125]. However, some other milder reductants, such as ascorbic acid, have been used to achieve a partial[126] or total reduction[87,92].

Several peptides and proteins can be used for the capping and stabilization of metal NCs, which affect their optical properties and the interaction with living matter through a specific interplay[128]. Among them, the tripeptide glutathione (GSH) and proteins such as ovalbumin (OVA) or bovine serum albumin (BSA) are the most used, mainly for the *in situ* growth of NCs. However, in the case of GSH-stabilized nanoclusters, other methods can be used apart from the bottom-up Au(III) reduction[129]. In particular, the use of GSH on pre-synthesized gold nanoparticles allows an etching process[130] that can help to homogenize a polydisperse population with the size focusing effect[122]. Another available method comprises thermal reduction at high temperatures, which can be used only on high thermostable systems based on single amino acids[131] or peptides such as GSH[125].

Previous works have been essential to understand how Au nanocrystals grow on proteins and how proteins can be designed to optimize the desirable nanocluster. For example, the work by Maity *et al*. explored the complete process of gold nucleation and reduction on ferritin using crystallography[132,133], whereas Xu *et al.* investigated the role of different protein profiles in the nanocluster formation[134]. These works show that the positive and amine-rich residues (e.g., lysine and arginine) are responsible for the coordination of the $AuCl_4$ ions, whereas other residues (for instance tyrosine, tryptophan and specially cysteine) reduce and strongly bind the metal. Moreover, our group has directed its efforts towards the green synthesis of AuNCs, focusing on the rational design of the protein coordination environment, first aiming at a NCs synthesis with mild-reductants[92] and afterwards clustering the coordinating residues on the protein surface area,[87] and including tryptophan in the protein sequence to

enhance the PL properties of the NC by energy transfer from the protein to the cluster [137].

Protein templates tune the NCs properties through coordination. Among the NCs qualities, the optical photoluminescence is particularly fascinating and has been extensively studied since it is applicable in many different scenarios, such as sensing and imaging. The interest in tuning the photoluminescence of protein-coordinated metal NCs has yielded several works assessing different amino acid compositions and commonly used natural proteins as coordinating agents[137]. However, these works focus on comparing various protein features among natural proteins without a systematic work on engineering proteins to understand the underlying relationship between NCs photoluminescence and their protein ligands. Up to date, there is no deep understanding of the role played by the coordinating protein on the features of NCs and the coupling between the capping residues and PL properties of the cluster. Considering the role of the stabilizing agents on the NCs properties, an extra level of tailoring can be achieved by exploiting protein engineering.

2.1.4.X-ray absorption spectroscopy

The structure of nanoclusters is a crucial aspect to study. There are several spectroscopic tools, such as UV-Vis spectroscopy or photoluminescence spectroscopy, that can be used to probe the physico-chemical properties of a NC by probing their molecular orbitals and extracting information on their energy states. These techniques are based in the interaction of photons with the studied molecules, mainly through absorption of light, and the phenomena used for the molecules to dissipate the excess of energy (e.g., fluorescence). However, those approaches cannot evaluate the physico-chemical properties of the individual atomic components of those NCs,

because the generated photons do not possess enough energy to excite electrons from inner shells in atoms. Synchrotron facilities are designed to produce extremely energetic X-ray radiation with a high flux (number of photons per second), as well as being equipped with optical setups that allow manipulating the X-ray beam to control different parameters such as their energy or size. Those high energy X-rays can excite the electrons located in the inner shells of heavy metals, which is suitable for studying, among others, metallic structures such as metal nanoclusters or metal centers in proteins. In particular, synchrotron-based X-ray Absorption spectroscopy (XAS) can shed light on the chemical environment and the oxidation states of the metal atoms excited. XAS techniques have been vital for determining the structure-function correlation in metalloproteins[138], as well as subtle changes in their electronic or chemical state.

X-ray absorption occurs when an incoming photon collides with a core electron at its binding energy, ejecting such electron from the atom. (Figure 2.1). Each element has its characteristic electronic binding energy in each core energy level (K-edge, L-edge, M-edge). Typically, XAS experiments allow to tune the X-ray beam energy in order to excite a particular edge of an element. Then, detectors are set up to measure the X-ray beam intensity before and after interacting with the sample to obtain the X-Ray absorption coefficient as a function of the beam energy.

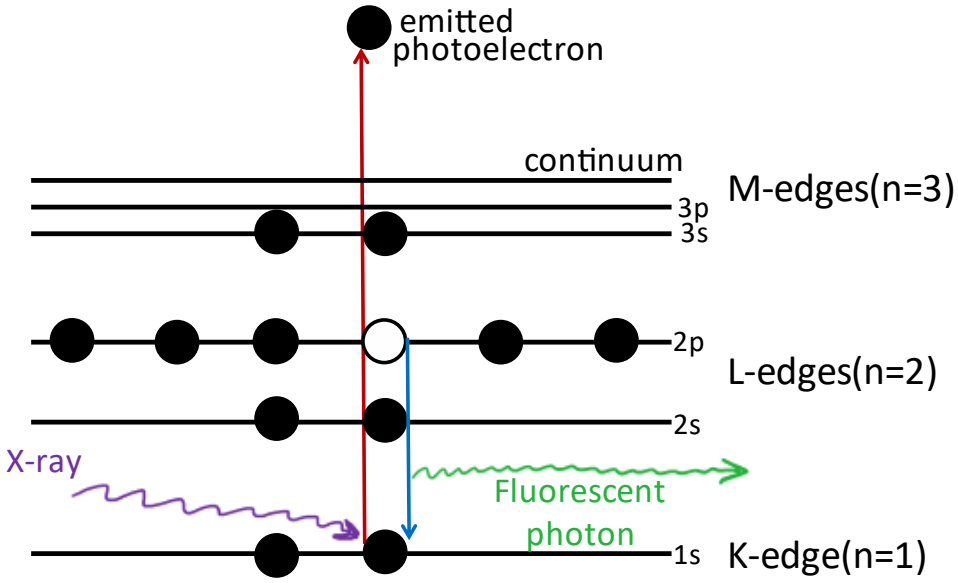

Figure 2.1. Schematic model of an X-ray absorption event. When the X-ray beam has the same energy as the core shell atom's binding energy, the latter is ejected from the atom in the form of a photoelectron. The core hole is then filled with an electron from higher electronic orbitals, which can dissipate the excess of energy, for example, in the form of fluorescence.

XAS spectrum is divided into the X-ray absorption near-edge structure (XANES) and the extended X-ray absorption fine structure (EXAFS) regions (Figure 2.2). The XANES region corresponds to the X-ray energies close to the binding energy of the electrons (the edge). The features before the edge correspond to the electronic configuration of the element. In contrast, the features right above the edge represent effects such as multi-scattering or the many bodies effect, which contains essential information about the oxidation state of the sample and the coordination chemistry. On the other hand, the EXAFS region goes for tens to a thousand of eV above the edge

and represents the interference between the outgoing wave of the emitted photoelectron and its elastic backscattering when it encounters a neighboring atom (Figure 2.2). The interference wave depends on the number, distances, and type of scattering atoms, so the data inferred can define the z-number, bond distances, and the number of ligands.

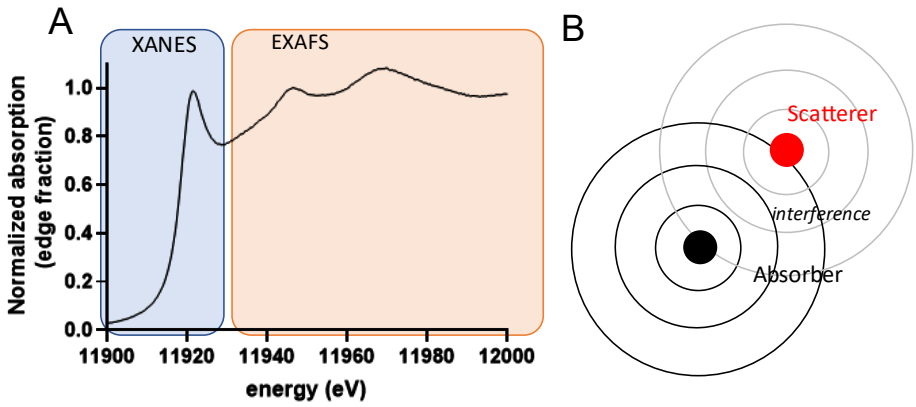

Figure 2.2. X-ray Absorption (XAS). A) The XAS spectrum can be divided into two areas. The XANES area corresponds to the energies close to the binding energy of the core electron (also called edge or whiteline), while the EXAFS region corresponds to energy levels above the edge. B) The information extracted from the EXAFS region corresponds to the interference pattern generated by the interaction of the emitted photoelectron from the absorber atom and the neighboring scattering atoms.

The information extracted from the EXAFS region, has a significant limitation in determining the atomic scatters beyond the first or second neighboring atoms, given that the number of events is much smaller, and other edges could be excited if the energy derives too much from the originally targeted edge. However, in very crystalline samples, such as big

metallic nanoparticles, other coordination spheres beyond the second one could be evaluated, although this is not the case for metalloproteins in solution. The typical distance range in which the accuracy is good for non-crystalline samples is 3-4 angstrom. This limits the EXAFS information that can be extracted in metalloproteins with very complex coordination spheres.

2.2. Approach

The main aim of this project is to perform an exhaustive characterization of the behavior of metallic NCs scaffolded by engineered proteins. The approach selected to shed light on how the protein coordination affects the photoluminescence properties of NCs consist of using non-emissive self-standing AuNCs and their coordination into a collection of proteins that share the same structure but encode different metal-coordinating residues, at the same positions, to coordinate the AuNCs.

Up to date, such a systematic approach to address this relevant aspect using engineered protein templates has not been reported. Towards this aim, a series of CTPR proteins were designed in which the metal-binding site is composed of different coordinating amino acids: either cysteines or histidines. Screening diverse amino acids coordinated to NCs synthesized *ex situ* will explore the role of the capping ligands while avoiding any effect on the PL caused by the metal coordinating residues on the structure of NC grown *in situ*. For the AuNCs synthesis, Prof. Prieto and co-workers[133] described a method for the robust synthesis of water-dispersible gold nanoclusters without organic ligands, so-called naked gold nanoclusters (AuNKNCs). These non-passivated gold nanoclusters are non-emissive and require subsequent coating with different molecules such as adenosine monophosphate (AMP) or cysteines to achieve efficient PL in various spectral regions[139]. Therefore, those naked NCs are ideal to conjugate to

the two different metal-coordinating proteins designed for the proposed study, which resulted in strikingly distinct emission properties.

For a systematic and deep exploration of the role of the coordinating residues over the NCs optical properties, time-resolved PL and X-ray absorbance spectroscopies were employed to study the photophysics and structure of protein-AuNKNCs conjugates. Time-resolved PL is an optical spectroscopy technique that can determine the emission decay, a valuable parameter in resolving the possible photophysical mechanism for its PL. X-ray absorbance spectroscopy is a compendium of synchrotron radiation-based techniques used to obtain information on the electronical configuration of the different chemical species present in a sample, in addition to information about their chemical environment (Nature of species coordinated, bond-length, coordination number, geometry). Both approaches are highly valuable to unknot the role that chosen residues in engineered proteins have in the PL changes of AuNKNCs.

The results of this work provide the first reported example of the simple generation of protein-NC systems with photophysical features tuned only by the protein template, starting from a unique non-emissive nanomaterial. Most importantly, they contribute to deepen our understanding of the mechanisms behind the optical properties of metal nanomaterials when biomolecules, particularly proteins, coordinate them.

2.3. Results and discussion

2.3.1. Protein Design

CTPR proteins with different metal-coordination sites were designed based on the PDB crystal structure 2HYZ[138]. Metal coordination sites consisting of a tetra-histidine (his) or a tetra-cysteine (cys) were engineered on a CTPR

motif and repeated four times in a tandem protein. These residues were chosen based on their ability to coordinate noble metals. As previously described, the coordinating residues were introduced in positions 2, 6, 9, and 13 of the CTPR motif[137]. Combining these mutated CTPR motifs (C4cys or C4his depending on the residue used for metal coordination), and the wild-type CTPR motif (WT) as flanking blocks, two proteins with six CTPR modules were constructed with the following structure: WT(C4his)$_4$WT and WT(C4cys)$_4$WT, which for the sake of clarity will be called C6-16his and C6-16cys respectively; each of these designed proteins includes 16 coordinating residues (Figure 2.3**).** In addition, all the designed proteins contain a C-terminal solvating helix intended to improve the solubility in aqueous media with the inclusion of polar residues[140].

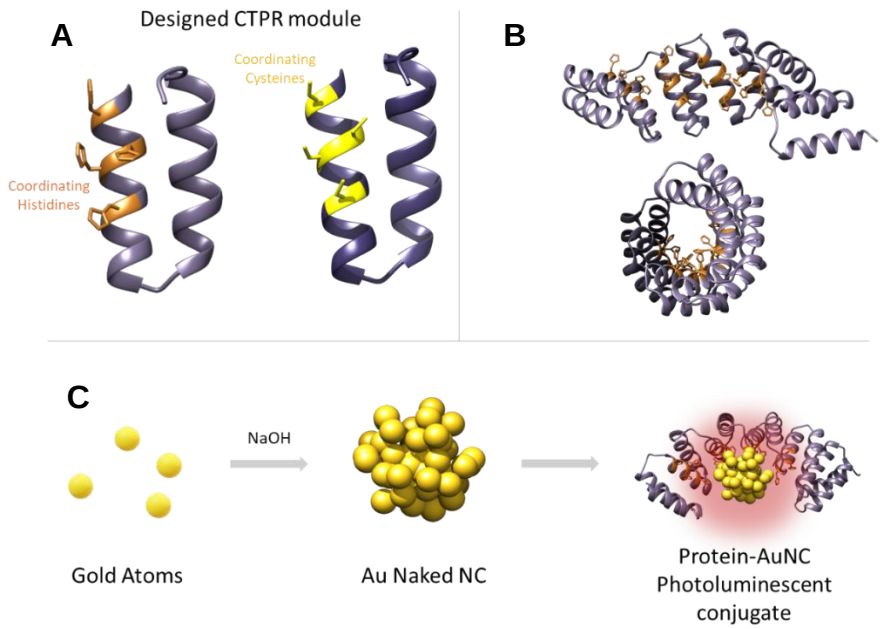

Figure 2.3. Designed consensus tetratricopeptide repeats (CTPRs) to coordinate naked metal nanoclusters. A) Mutated CTPR motif in which

4 metal-coordinating histidines (orange) are introduced at positions 2, 6, 9, and 13 within the 34 amino acid CTPR sequence. The exact positions were mutated to 4 cysteines (yellow) to construct a coordinating protein module based on cysteines. B) 4 CTPR motifs with the metal-coordinating amino acids are combined and flanked with 2 wild-type CTPR modules to construct CTPR proteins with 6 repeats (C6-16cys and C6-16his). Front-view and side-view of C6-16his protein structural model based on the crystal structure of CTPR8 (PDB ID: 2HYZ)[141]. When the mutated CTPR units are combined with two WT capping repeats, the coordinating residues are localized on the inner concave surface of the CTPR superhelix. C) Scheme of the formation of CTPR-templated AuNKNCs, pre-formed Au naked NCs are coordinated by the engineered CTPR repeat proteins.

2.3.2. AuNKNCs synthesis, conjugation, and characterization

The naked gold nanoclusters were synthesized following the protocol developed by Prof. Prieto and co-workers (see Experimental Section 2.5.2.)[141], resulting in a transparent solution of non-photoluminescent NCs of around 2 nm in size (Figure 2.4b and c). First, the AuNKNCs were washed to remove the excess reactants. The optical properties of AuNCs are one of their most valuable features. Different AuNCs can be synthesized to tune the emission properties and other spectroscopic features such as the PL lifetime. For example, the design of red-emitting clusters can be achieved with the capping of specific organic molecules (such as thiolates)[137] or increasing the size of the NCs[137].

The AuNKNCs-CTPR conjugates presented PL (Figure 2.4a), as expected considering the previous report in which capping AuNKNCs with organic molecules led to highly emissive systems. This result confirms the efficient coordination of AuNKNCs by the engineered proteins, whereas none of the controls, i.e., CTPR WT protein without coordinating residues and CTPR-

16glu protein with glutamic acids in the coordinating positions, lead to emissive composites (Figure 2.4c and 2.5). Furthermore, the chemical identity of the metal coordinating amino acids (cys or his) within the protein encoded different emission color of the coordinated AuNKNCs when irradiated with a UV lamp (Figure 2.4a), and their absorbance spectra showed a tail in the 300-350 nm region (Figure 2.4b). Both protein-AuNKNCs systems displayed PL upon photoexcitation at 390 nm. The PL spectra of C6-16his-AuNKNCs (Figure 2.4c) peaks at 515 nm and tails down to 750 nm. Strikingly, the PL spectrum of C6-16cys-AuNKNCs peaks at 675 nm (Figure 2.4c) and tails down to 900 nm.

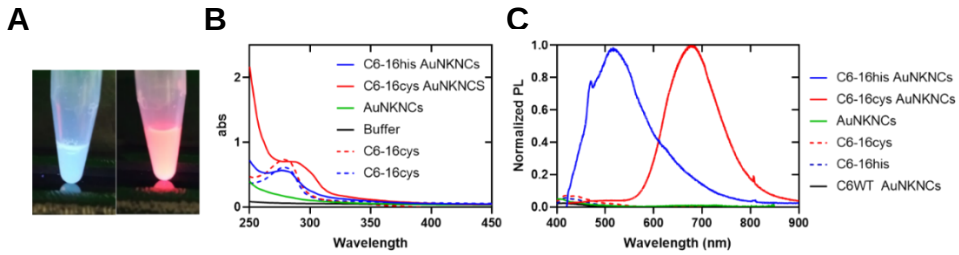

Figure 2.4. PL properties of AuNKNCs-CTPR protein conjugates carrying cysteines or histidines. A) Picture taken on C6-16his-AuNKNCs (left) and C6-16cys-AuNKNCs conjugates liquid dispersions under UV light. B) Absorption spectra of AuNKNCs and protein-AuNKNCs conjugates: C6-16his-AuNKNCs (solid blue), C6-16cys-AuNKNCs (solid red), C6-16his protein (dashed blue), C6-16cys protein (dashed red), AuNKNCs (green), and buffer (black). C) PL spectra of C6-16his-AuNKNCs (solid blue), C6-16cys-AuNKNCs (solid red), C6-16his protein (dashed blue), C6-16cys protein (dashed red), C6WT-AuNKNCs (solid black) and AuNKNCs (green) upon photoexcitation at 390 nm. The spikes at 470 nm and 808 nm are ascribed to buffer contribution and scattering from the pump, respectively.

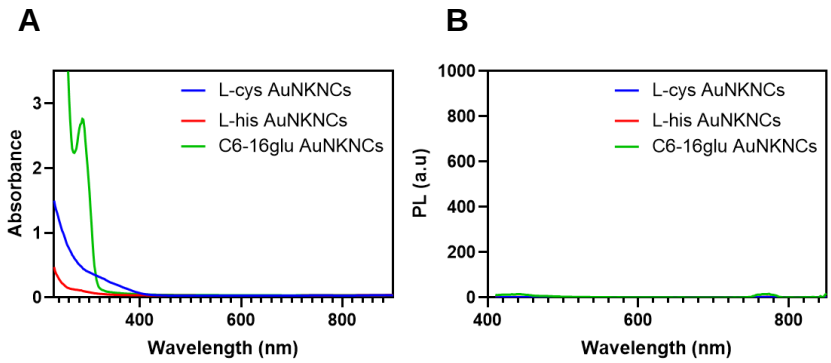

Figure 2.5. **PL properties of AuNKNCs-CTPR protein conjugates carrying glutamic acids or capped with L-amino acids.** UV-vis absorbance spectra (a) and PL spectra (b) at λ_{ex} = 390 nm of the L-amino acids and the C6-16glu controls.

One of the parameters worth exploring is coordination stoichiometry, since the quantity of gold reactant in comparison with the number of available coordination residues in the proteins could change the coordination dynamics, optical properties and structure of the resulting AuNCs. Thus, the number of AuNKNCs per protein in the conjugation reaction was varied from 3 to 100 molar excess of gold salts. Since the increase in AuNCs size impacts the luminescent properties shifting the emission towards the red region[142], we hypothesize that similarly, incrementing the number of effective coordinating residues bound to gold may also yield a PL change. Therefore, the Au stoichiometry was changed to explore a concomitant effect on red and blue emission bands. The screening tests indicated that increasing the amount of gold per protein promoted the red emission band at the expense of the blue emission in C6-16cys-AuNKNCs, (Figure 2.6). However, for the C6-16his-AuNKNCs, only changes in PL intensity were observed, without significant spectral variations. Hereafter, an Au-to-protein molar ratio of 30 equivalents will be used, unless otherwise stated, since this ratio gives rise to the maximum PL intensity of C6-16his-AuNKNCs,

whereas C6-16cys-AuNKNCs displays significant red emission at that gold ratio.

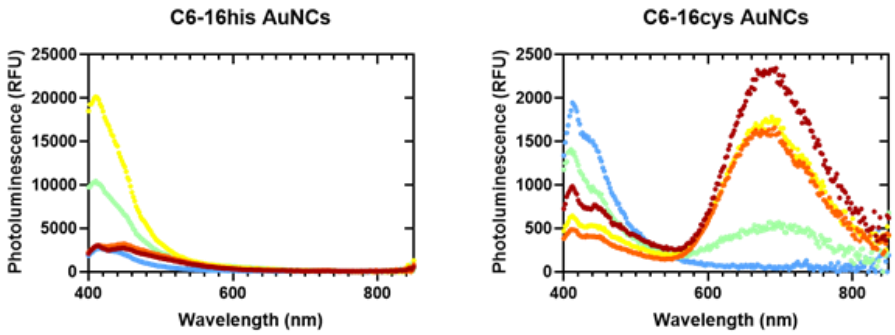

Figure 2.6. Gold:protein ratio affects the PL. Photoluminescence spectra of the Left) C6-16his and Right) C6-16cys designed protein scaffolds with different molar ratios of Au to protein: 100:1 (burgundy), 50:1 (red), 30:1 (yellow), 10:1 (green) and 1:1 (blue).

The protein-AuNKNCs conjugates were imaged using Transmission Electron Microscopy. The AuNKNCs grid presented particles with a mean diameter of 1.6 ±0.3 nm (Figure 2.7) and similar polydispersity to that previously reported by Prof. Prieto and co-workers[143].

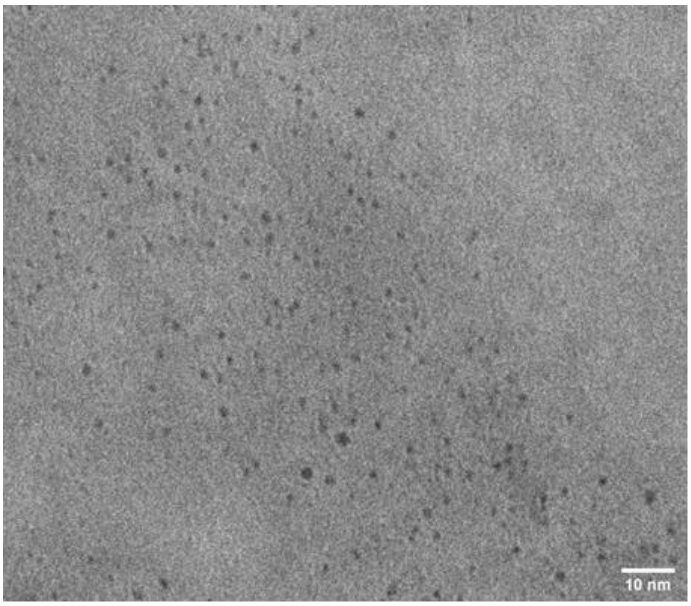

Figure 2.7. Non-capped AuNKNCs. TEM micrograph (120 kV) of AuNKNCs freshly synthesized.

After the conjugation, the purified protein-AuNKNCS conjugates showed a homogeneous dispersity consisting of a mean diameter of 1.7 ± 0.3 nm for C6-16cys-AuNKNCs and 1.7 ± 0.5 nm for C6-16his-AuNKNCs (Figure 2.8a), which is in agreement with the size obtained for the AuNKNCs and the previously reported molecule-capped AuNKNCs[144]. The conjugates were further characterized using MALDI-TOF mass spectroscopy to confirm the coordination of AuNKNCs by the protein. The MALDI results showed that the mean size of metal nanoclusters was 14 ± 7 gold atoms per cluster for the C6-16cys-AuNKNCs conjugates and 18 ± 4 gold atoms per cluster for the C6-16his-AuNKNCs (Figure 2.8b). Given the standard deviation of MALDI measurements, the sample may present 18-gold atom clusters (among other populations). 18 is one of the so-called ‘magic numbers’ for

AuNCs and positively affects the robustness of the clusters since the 18-gold atom clusters have the exact number of electrons to fill the s, p, and d atomic orbitals[145]. The conjugates were further characterized by X-ray Photoelectron Spectroscopy (XPS) to determine the oxidation state of gold within the coordinated AuNKNCs. The deconvolution of the signal of Au $4f_{7/2}$ showed a mixture of Au(0), Au(I), and Au(III) with binding energies at 84, 85, and 87.5 eV, respectively in both protein conjugates (Figure 2.8c). However, significant differences were observed in the relative ratios of the different oxidation states. For C6-16his-AuNKNCs, the relative amount of gold species was 27% Au(0), 63% Au(I), and 10% Au(III), while for C6-16cys-AuNKNCs, the relative amount of gold states was 72% Au(0), 22% Au(I), and 6% Au(III). This elemental analysis supports the fact that cysteine-rich coordinating protein acts as a more potent reductant for gold than the histidine-rich protein. Moreover, the different ratios of gold species can be correlated with the optical properties of the coordinated clusters. In this respect, the Au(I) percentage of 22% on C6-16cys-AuNKNCs agrees with the data reported in literature for red-emitting thiolated-AuNCs, which usually ranges from 10% to 25%[137]. Meanwhile, the higher binding energy observed on the Au 4f7/2 shell in C6-16his-AuNKNCs is commonly described for blue-emitting gold nanoclusters[146], related to the smaller size of the cluster as the binding energies increase[141,147]. In the case of the standalone AuNKNCs, the XPS analysis fitting revealed a composition of 80.5% Au(0) and 19.5% Au(III); which does not agree with the XPS data previously reported[131,148], consisting of a mixture of Au(0) and Au(I); probably due to the remaining Au(III) salts present in our AuNKNCs sample.

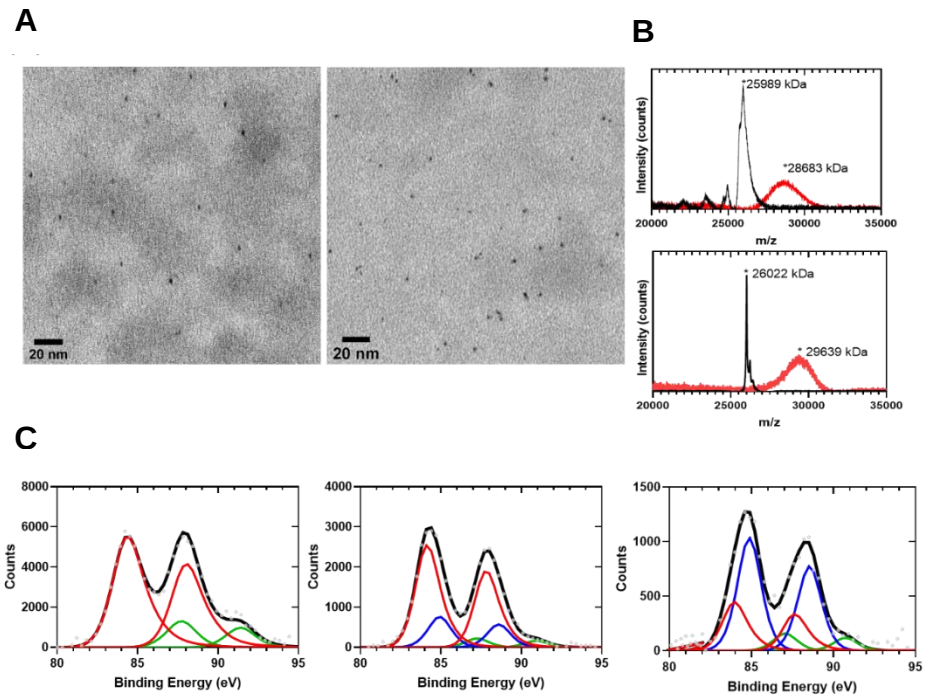

Figure 2.8. **AuNKNCs-CTPR protein conjugates characterization.** (a) TEM micrographs at 120kV of the C6-16cys (left) and C6-16his (right) templated AuNKNCs. The scale bar corresponds to 20 nm. (b) MALDI-TOF mass spectra of the design proteins (black) and the protein-AuNKNCs conjugates (red) for C6-16cys (top) and C6-16his (bottom). (c) XPS spectra of AuNKNCs (left), AuNKNCs templated by C6-16cys (middle) and by C6-16his (right). The black lines correspond to the XPS spectra, and the colored lines correspond to the spectra deconvolution for the species Au(0) in red, Au(I) in blue, and Au(III) in green.

In addition to steady-state PL, time-resolved PL measurements were carried out in the protein-AuNKNCs to shed light on their light-emitting properties. The PL dynamics of C6-16his-AuNKNCs at 515 nm (Figure 2.9a, b) follow a three-exponential law with an amplitude-weighted average of 1.7 ns. For C6-16cys-AuNKNCs, the PL at 700 nm decays slowly following a three-exponential law with an average lifetime of 1.6 µs (Figure

2.9c, d). In the case of protein conjugates produced with 100 equivalents of gold, the results depend on the type of protein functionalization. C6-16his-AuNKNCs possess two PL contributions at 515 and 700 nm, although its light emission is less intense than its 30 gold equivalents counterpart and C6-16cys conjugates. The PL at 515 nm decays with an amplitude average of 2.0 ns, whereas the PL band at 700 nm decays with an average lifetime of 0.9 µs, all of them following a three-exponential law. Contrarily, the PL spectrum of C6-16cys-AuNKNCs displays a maximum at 700 nm, and PL decay follows a three-exponential model with an average lifetime of 1.2 µs (Figure 2.10). As reported elsewhere, the blue PL bands with nanosecond decay components are ascribed to AuNC inner transitions across the discrete levels within the Au d- and sp- bands [114,149]. The red PL band is assigned to phosphorescence based on the associated microsecond PL decay and its strong intensity-dependence with oxygen (Figure 2.11).

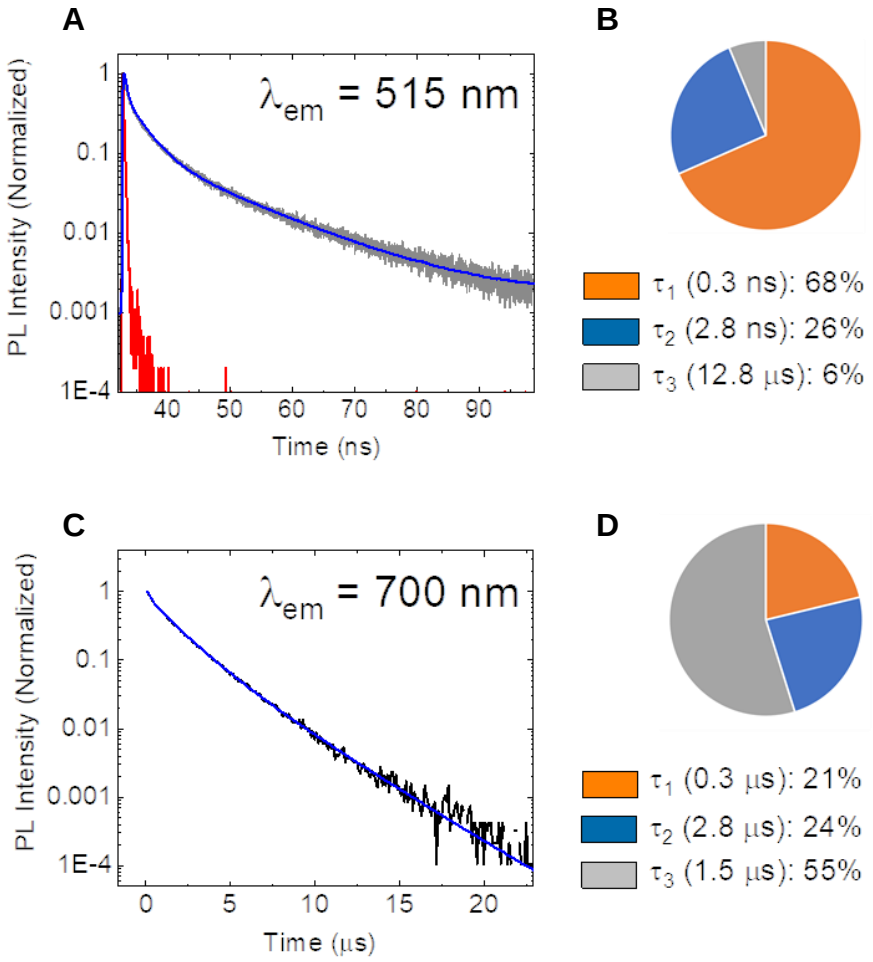

Figure 2.9. The PL decay curves of the protein-AuNKNCs conjugates obtain from 30 equivalents of chloroauric salts. PL spectrum photoexcited at 405 nm, PL dynamics detected at the PL peak and PL lifetime components obtained from a three-exponential fit of C6-16his-AuNKNCs (A, B) and of C6-16cys-AuNKNCs (C, D). Blue lines in (A, C) stand for three-exponential fits to the PL decay curves. The red line in (A) represents the instrumental response function of the setup.

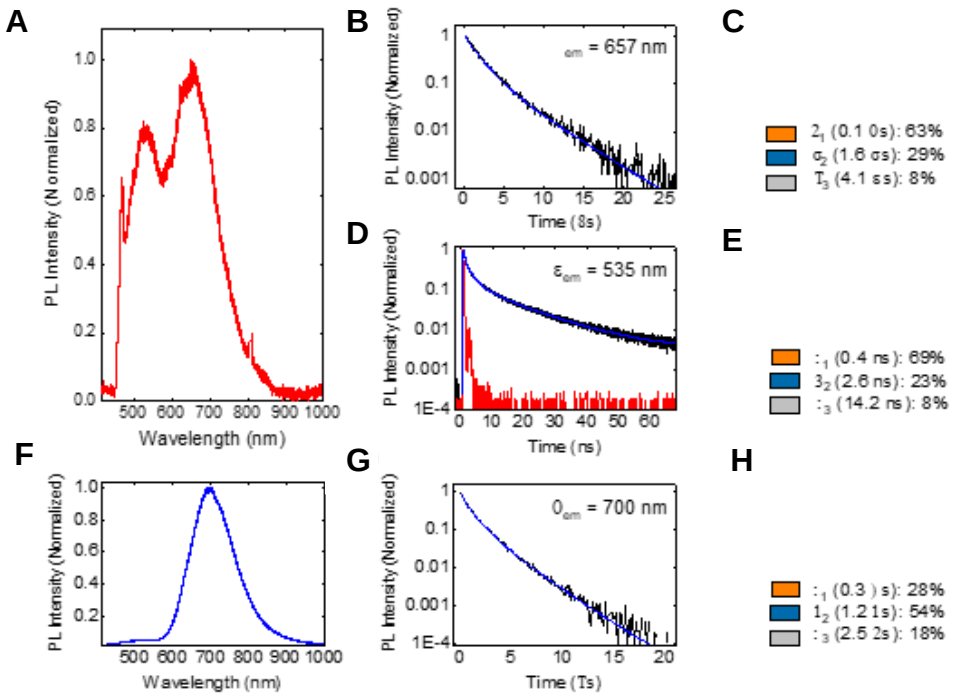

Figure 2.10. The PL spectra and PL decay curves of Protein-AuNCs obtained from 100 equivalents of chloroauric salts. A) PL spectrum of C6-16his AuNC photoexcited at 405 nm. The spikes at 475 nm and 808 nm are ascribed respectively to buffer contribution and scattering from the pump. B, C) PL decay detected at 657 nm and PL decay components. D, E) PL decay detected at 535 nm and PL decay components. (f) PL spectrum photoexcited at 405 nm of C6-16cys AuNCs, G, H) PL decay detected at 700 nm and PL decay components. Blue lines in (B, D, G) stand for three-exponential fits of the PL decay curves. Red line in (D) stands for the instrumental response function of the set-up.

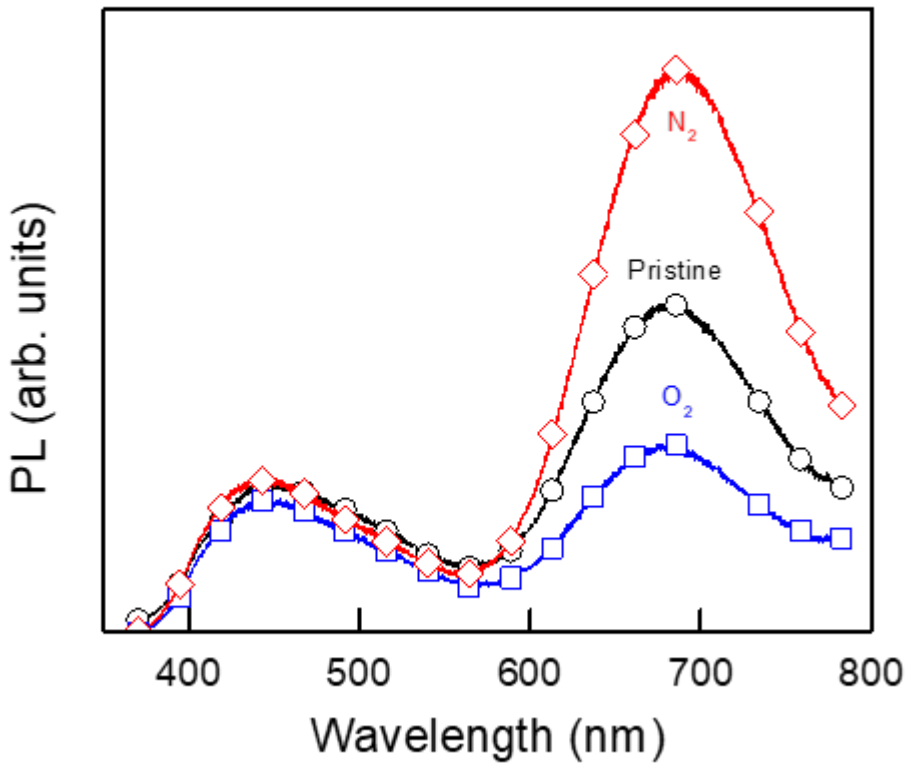

Figure 2.11. Phosphorescence emission from C6-16cys-AuNKNCs. PL spectra of C6-16cys-AuNKNCs: pristine (black open circles), bubbled with O_2 (blue open squares) and bubbled with N_2 (red open diamonds). Solutions were purged for 3 minutes.

Considering that the protein conjugates were synthesized from a single batch of AuNKNCs, and thus their size should be the same, this difference in PL may not be a consequence of the NC size, as usually reported[131,148]. Besides, the size inferred from the mass spectrometry results indicated that the blue-emissive histidine-coordinated AuNCs are only slightly larger than the red-emissive cysteine-coordinated AuNCs. Consequently, the change in the PL properties must instead be related to an interplay of the capping

ligands on the AuNC electronic properties. The formation of ligand-to-metal charge transfer (LMCT) or ligand-to-metal-metal charge transfer (LMMCT) states has been extensively described for ligand-capped AuNCs, especially those carrying thiol-Au coordination[150]. The observed PL spectrum in C6-16cys-AuNKNCs conjugates agrees with previous reports in protein-templated AuNCs in which the coordination is achieved using cysteines[151], and also in AuNCs capped with small molecules using thiols[152]. Furthermore, other bond-involved electron-rich heteroatoms and groups (O, N, -COOH, and NH_2) have also been related to these mechanisms and could play an essential role in activating the metal triplet state[150]. In addition, as reported before, histidine-capped AuNCs hold a bluish-green emission (490 nm) with short lifetimes[151].

2.3.3. AuNKNCs conjugates stability studies

To further understand the role of the protein scaffold in the PL spectrum of the AuNKNCs and how the luminescence changes with a compromised protein structure, thermal denaturation ramp and enzymatic digestion were performed. The experiments assess the protein secondary structure (thermal denaturation) and the primary integrity of the polypeptide chain (trypsin digestion). First, circular dichroism spectrometry (CD) was performed in order to check the protein integrity once the AuNKNCs were conjugated (Figure 2.12). The results showed no significant change in the CD spectra for C6-16cys-AuNKNC compared with the pristine protein. However, there was an evident change in the ratios between the minima at 220 nm and 205 nm in the histidine-rich protein, which points towards a partial loss of the alpha-helical content.

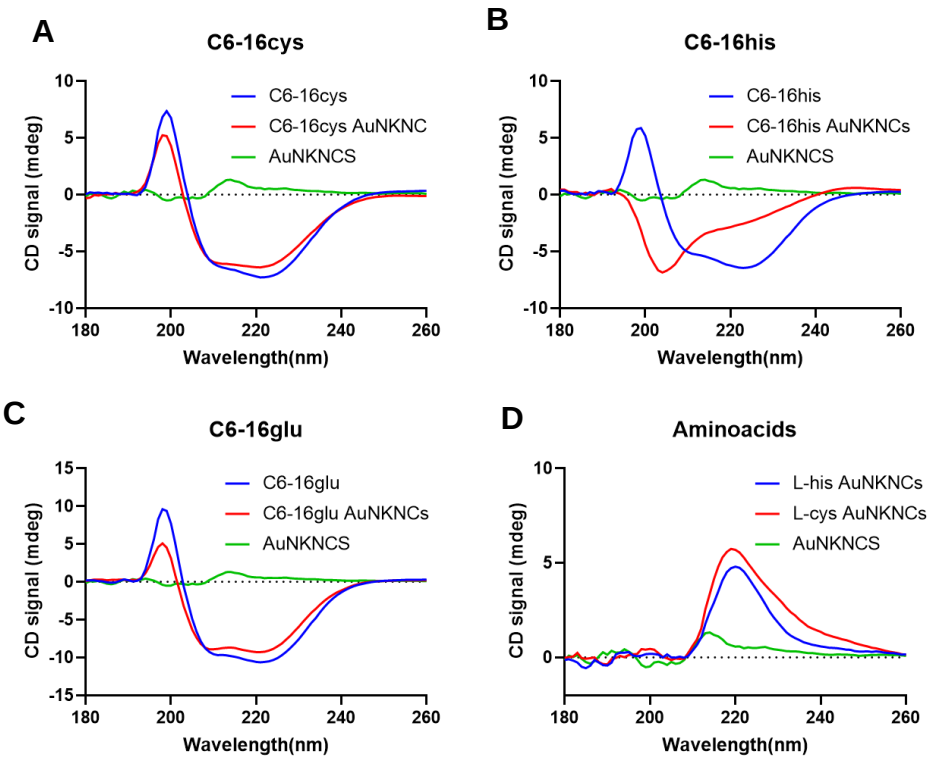

Figure 2.12. AuNKNCs-CTPR secondary structure stability. Far-UV circular dichroism spectra of the proteins (blue), the protein-AuNCs conjugates (red) and the non-capped AuNKNCs (green). A) C6-16cys B) C6-16his, C) C6-16glu and D) AuNKNCs capped with L-amino acids, L-his (blue) and L-cys (red).

When performing temperature ramps, the PL (λ_{ex} 390 nm) for C6-16cys protein conjugates did not change along with the increasing temperature, while for the histidine-rich protein, there was a significant increase in PL when the sample cooled down after the temperature ramp (Figure 2.13). The working hypothesis on this points towards a re-arrangement of the N-Au bond due to its less stiff nature when triggered by thermal movement[157].

If this were the case, energy optimization could be the leading cause of the emission increase observed. For C6-16cys-AuNKNCs conjugates, the rigidity of the S-Au bond could explain the absence of a significant change since the restriction for internal molecular movements of such bonds could lead to emissive relaxation pathways when the cluster is excited[156,158].

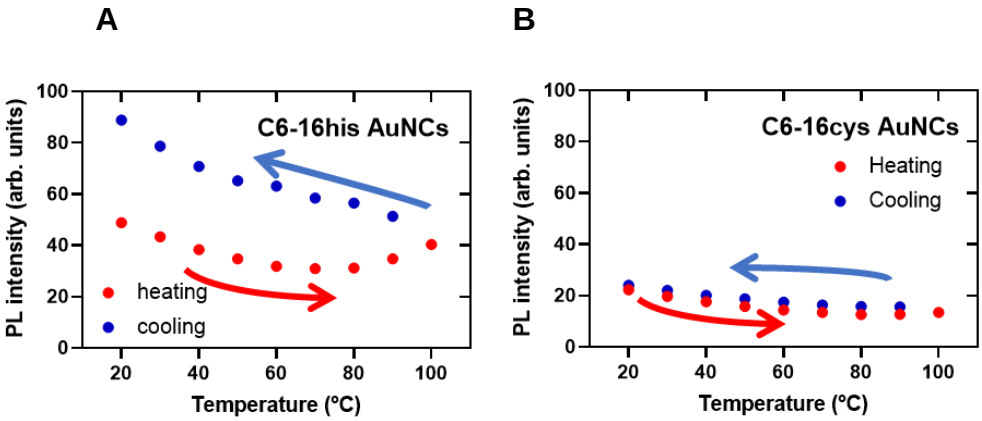

Figure 2.13. AuNKNCs-CTPR protein conjugates thermal stability. Photoluminescence of the protein-AuNCs conjugates with increasing (red circles) and decreasing (blue circles) thermal denaturation steps for C6-16his-AuNKNCs A) and C6-16cys-AuNKNCs B) for λ_{ex} at 390 nm.

After trypsin digestion, a decrease in the emission intensity was observed, but the remaining PL was maintained even at high concentrations of trypsin for both conjugates. However, the protein was utterly digested (Figure 2.14), reinforcing the importance of the surface ligand in PL rather than the structural integrity of the protein. To further understand the role of the coordinating amino acids and the protein scaffold, controls in which the AuNKNCs were conjugated to L-cysteine and L-histidine were assessed using the same protocol and stoichiometry as for the protein conjugates. The samples were spectroscopically characterized using PL, UV-Vis, and CD. They all lacked PL emission (Figures 2.5 and 2.12), which points to the

relevance of the protein metal-binding surface (i.e., the higher amount of available coordinating residues per surface unit in the protein in constrast with the free residues in solution) in the process of NC stabilization and tuning their optical properties.

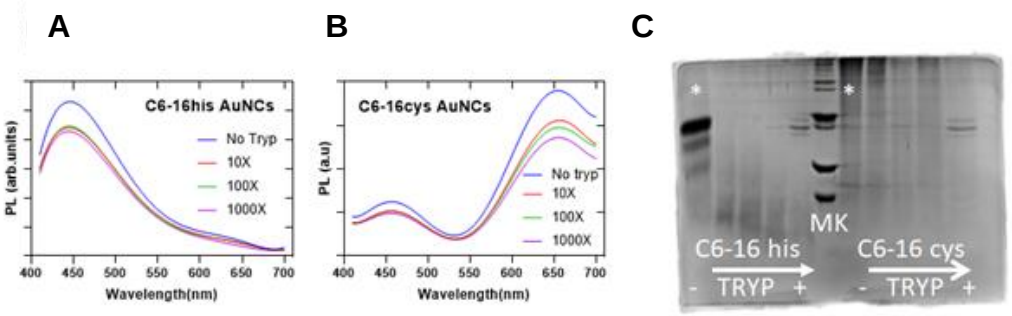

Figure 2.14. Trypsinization of AuNKNCs-CTPR conjugates. Photoluminescence of the AuNKNCs-C6-16his (A) and AuNKNCs-C6-16cys (B) conjugates with increasing amounts of trypsin for λ_{ex} at 390 nm. C) Picture of PAGE gel of the protein-AuNKNCs conjugates with increasing amounts of trypsin. MK= protein marker; asterisks (*) mark the control lanes with protein-AuNKNCs without trypsin. The direction of the arrows indicates increasing amounts of trypsin.

2.3.4. AuNKNCs conjugates X-Ray absorbance spectroscopy

The chemical and coordination properties of the NC in presence of the proteins were characterized using X-ray absorbance spectroscopy (XAS) to determine the relationship between the chemical composition and coordination of the Au within the protein and the optical properties of the AuNCs. This experiment helps to corroborate the information about oxidation states obtained from XPS and becomes a valuable tool to attain information about the state of the clusters and the protein coordination [156]. Protein-AuNKNCs conjugates were generated using both 30 and 100

equivalents of Au compared to the protein, concentrated to obtain solutions of at least 0.1 mg/mL of gold, and studied at B18 beamline (Diamond Light Source). In addition, several controls were also analyzed to determine possible changes in the AuNCs due to coordination to the proteins at residues different from the designed histidines or cysteines. These controls included non-passivated AuNKNCs but also protein conjugates with no specific gold coordinating residues: CTPR6 protein with 6 WT units (C6WT) and a CTPR with glutamic acids on the inner concave face (C6-16glu), which resulted in non-luminescent AuNKNCs, probably due to the interaction of the Au with other residues (i.e., lysines for C6-WT and glutamic acids for C6-16glu).

Principal Components Analysis (PCA) of the X-ray absorption near-edge structure (XANES) region of the spectra obtained (ranging from –20 to +80 eV around the edge) suggested the presence of 3 or 4 components on the set of samples measured. The standards used as components for the following Linear Combination Fitting (LCF) included: Au (0) foil; Au (III) hydroxide to mimic remaining Au salt; Au (I) Cl to emulate possible coordination of Cl to the NC during coordination to the proteins; Au (I) sulfide to reproduce coordination to cysteines; and Au (I) cyanide to model coordination to histidines, lysines, or glutamic acids (as N, O and C atoms are similar in size and better standards were not available).

Analysis of the individual samples using LCF (Figure 2.15, Table 2.1) showed that AuNKNCs are mostly a combination of Au(0) and Au(III)OH. This result is in agreement with XPS analysis showing similar Au(0) and Au(III) populations, although in general, XPS showed the presence of higher quantities of Au(0) in all of the samples measured. Nevertheless, for both protein-AuNKNCs conjugates, Au(0) seems to disappear, being in disagreement with the data extracted by XPS (Table 2.1). XANES analysis

of C6-16cys-AuNKNCs conjugates suggested strong Au(I)-S coordination, minor presence of other bonds (probably Au coordinated to nitrogen or oxygen), and a small percentage of Au(III)OH species. Equally, the binding of AuNKNCs to C6-16his seemed to be dominated by Au(I)-Cl or Au(I)-CN species, probably indicating the coordination to nitrogen from the histidines. However, the analysis of C6-16his conjugates was more problematic due to the lack of a standard fully mimicking the Au-imidazole bond. Remarkably, the coordination of C6-16cys proteins with increasing amounts of AuNKNCs did not change, but more significant amounts of Au(III) were observed when C6-16his was coordinated to 100 molar equivalents of gold. (Figure 2.16).

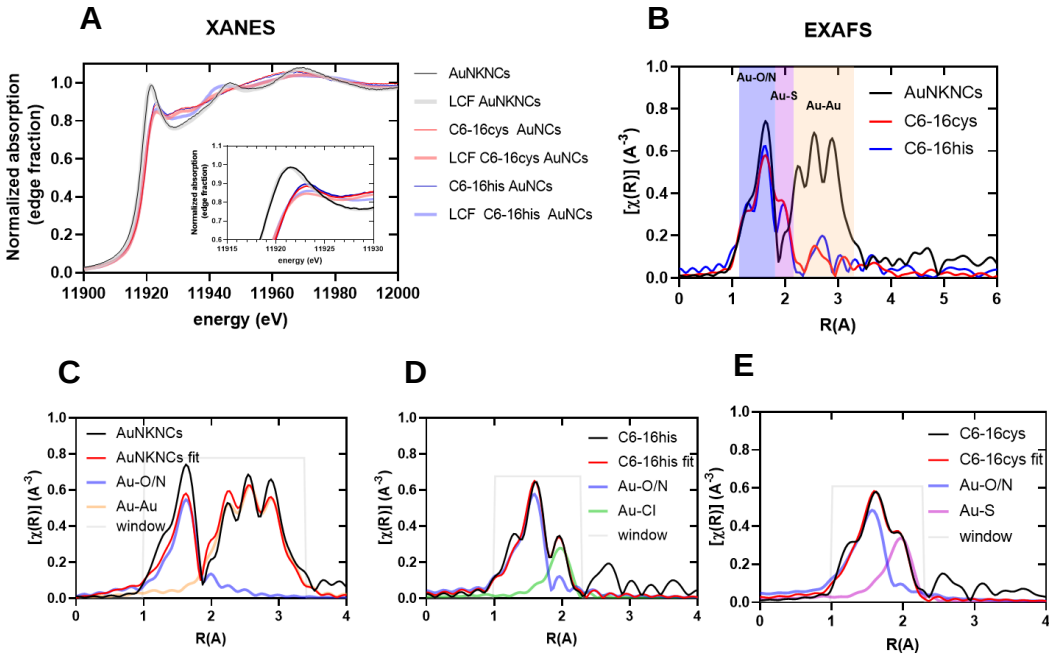

Figure 2.15. XAS spectra of AuNKNCs and AuNKNCs-CTPR protein conjugates. A) XANES spectra of the protein-AuNKNCs conjugates and their linear combination fitting (LCF): AuNKNCs (black, LCF in grey), C6-16cys-AuNKNCs (red, LCF in pale-red), and C6-16his-AuNKNCs (blue, LCF in pale-

blue). Detail of the whiteline in the inset. B) FT-EXAFS of the AuNKNCs (black), C6-16cys-AuNKNCs (red), and C6-16his-AuNKNCs (blue), with the colored areas that correspond to the Au-O/N (blue), Au-S(purple), and Au-Au(orange) bonds. C, D, E) Fitted FT-EXAFS with the single path scattering analysis for each component of AuNKNCs (C), C6-16his (D), and C6-16cys (E) conjugates. Measured EXAFS spectra (black), single path scattering fitting (red), Au-O/N component (blue), Au-Au component (yellow), Au-Cl component (green), Au-S component (purple), fitted window (grey).

Table 2.1: XANES data from AuNKNCs and AuNKNCs-CTPR protein conjugates. Data acquired with LCF analysis of Au L_3-edge XANES spectra fitting, in which each possible coordination is weighted using the standards described.

Sample	R-factor	X^2	Au(0)	Au(I) Cl	Au(III) OH	Au(I) S	Au(I) CN
AuNKNCs	0.0008930	0.0001050	61.8	---	38.2	---	---
C6-16cys-AuNKNCs 30 eq	0.0015115	0.0001849	---	---	5.9	80.5	13.6
C6-16cys-AuNKNCs 100 eq	0.0010692	0.0001293			4.8	85.2	10.0
C6-16his-AuNKNCs 30 eq	0.0033612	0.0004060	---	60.3	---	---	39.7
C6-16his-AuNKNCs 100 eq	0.0054142	0.0006469	---	49.4	6.9	---	43.6
C6-16glu-AuNKNCs 30 eq	0.0008712	0.0001025	14.3	48.2	11.0	---	26.5
C6-16glu-AuNKNCs 100 eq	0.0011418	0.0001381	36.4	42.2	---	---	21.4
C6-WT-AuNKNCs 30 eq	0.0020385	0.0002449	---	59.2	6.2	---	34.6
C6-WT-AuNKNCs 100 eq	0.0018819	0.0002272	---	65.1	2.5	---	32.4

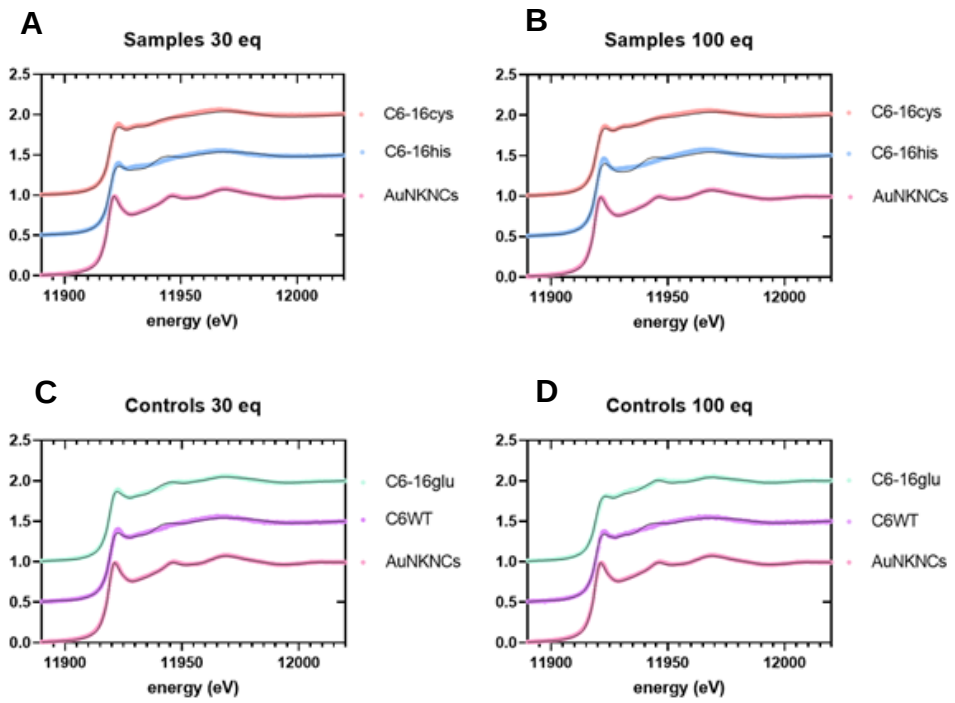

Figure 2.16. XANES spectra of AuNKNCs and AuNKNCs-CTPR protein conjugates. Au L_3-edge XANES spectra (black lines) and LCF (colored lines) of AuNKNCs and protein-AuNKNCs with including protein controls, for 30 and 100 gold equivalents.

Further analysis of the samples using extended X-ray absorption fine structure (EXAFS) allows obtaining information on the coordination sphere around the Au within the AuNCs, including the bond length and coordination numbers of the different bonds involved. LCF using the abovementioned standards was initially attempted to analyze the different samples (Figure 2.17). However, the lack of standards fully mimicking the Au-imidazole (or other Au(I)-N/O bonds) made it difficult to obtain suitable fittings under these circumstances. Accordingly, analysis of the different samples was performed using only single scattering paths of the different types of Au bond expected (O, S, Cl, Au; where O includes both Au-O and Au-N

contributions) for the fit (Figure 2.16, Table 2.2). This analysis confirmed the main Au (0) character of AuNKNCs that was observed on XPS and XANES measurements. FT-EXAFS fitting in agreement with XANES suggested Au-Au coordination (bond length of 2.86 Å, which fits the canonical Au-Au bond length extracted in Au crystals by EXAFS [140,158]) for two-thirds of the Au in the NCs, while the other third of the gold was present in Au-O/N bonds (bond length of 1.99 Å).

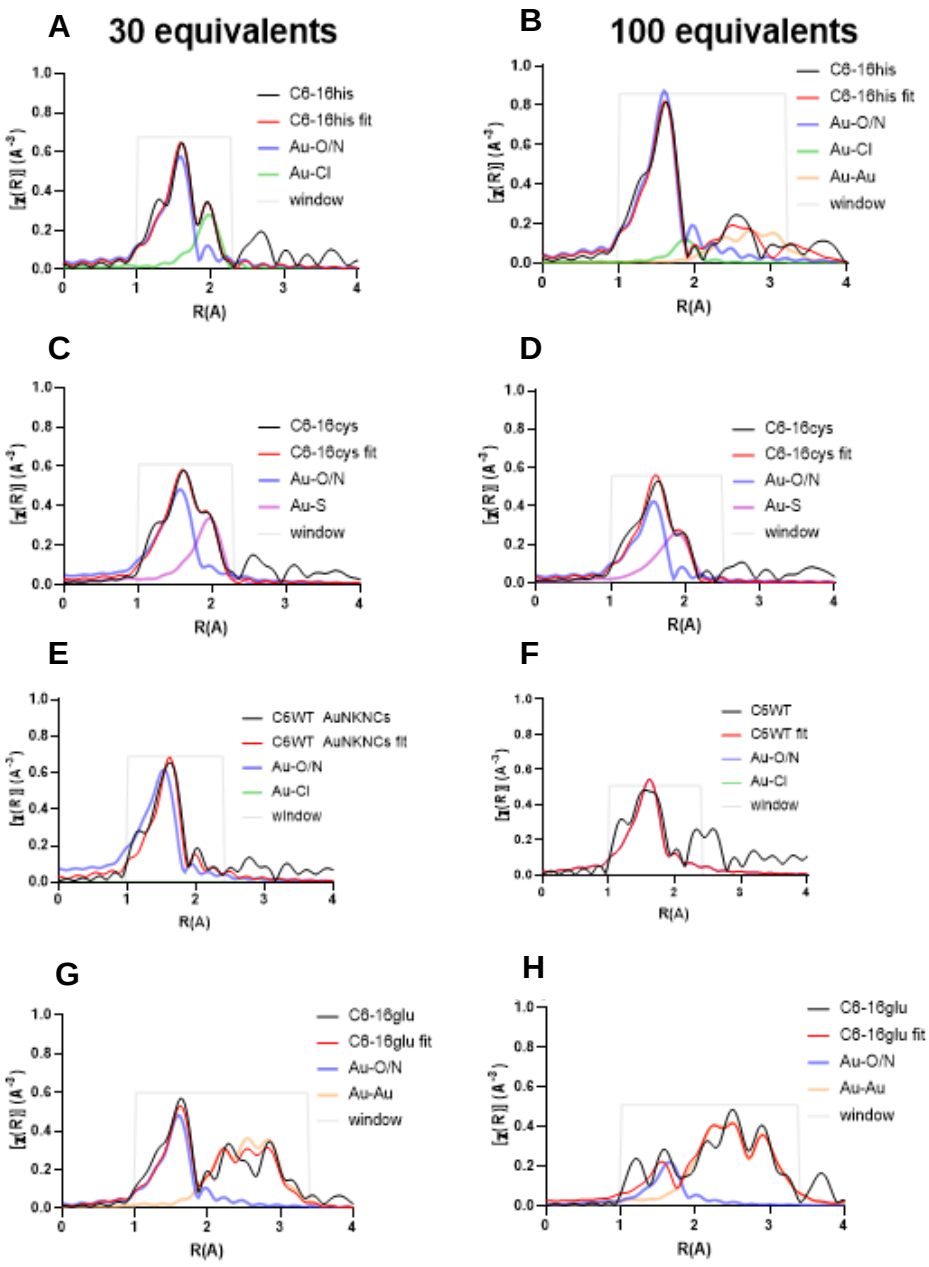

Figure 2.17. EXAFS spectra of AuNKNCs and AuNKNCs-CTPR protein conjugates. Au L_3-edge FT-EXAFS fittings of the C6-16his-AuNKNCs (A, B), C6-16cys-AuNKNCs (C, D), C6-WT-AuNKNCs (E, F), C6-16glu-

AuKNCs (G, H). Measured spectra (black), fitted spectrum (red) and single scattering paths for each component: blue for O/N, orange for Au-Au, green for Cl and purple for S-Au.

Table 2.2. Data acquired from Au L_3-edge FT-EXAFS analysis. On each component, the Amplitude (S_0^2*CN) and bond length is described for each sample. Standard deviation in brackets; when no brackets appear, the parameter was fixed during the fitting.

			Au-O/N		Au-S		Au-Cl		Au-Au	
Sample	**R-factor**	**X_2**	**Amplitude (S_0^2*CN)**	**Bond length (Å)**	**Amplitude (S_0^2*CN)**	**Bond length (Å)**	**Amplitude (S_0^2*CN)**	**Bond length (Å)**	**Amplitude (S_0^2*CN)**	**Bond length (Å)**
AuNKNcs	0.094	264.9	0.88 (0.16)	1.99 (0.02)	-	-	-	-	7.08 (1.56)	2.86 (0.01)
C6-16cys-AuNKNCs 30 eq	0.0278	105.2	1.24 (0.24)	1.98 (0.02)	0.55 (0.23)	2.33 (0.02)	-	-	-	-
C6-16cys-AuNKNCs 100 eq	0.0354	42.03	0.92 (0.12)	1.982 (0.009)	0.46 (0.15)	2.32 (0.02)	-	-	-	-
C6-16his-AuNKNCs 30 eq	0.0257	34.00	1.03 (0.23)	1.97 (0.02)	-	-	0.32 (0.17)	2.32 (0.03)	-	-
C6-16his-AuNKNCs 100 eq	0.0409	0.04	1.40 (0.09)	1.97 (0.01)	-	-	0.12 (0.05)*	2.19*	5.27 (2)*	3.13 (0.04)*
C6-16glu-AuNKNCs 30 eq	0.0938	39.23	0.85 (0.11)	1.98 (0.02)	-	-	-	-	3.16 (0.52)	2.83 (0.02)
C6-16glu-AuNKNCs 100 eq	0.1219	17.70	0.36 (0.11)	1.94 (0.04)	-	-	-	-	6.37	2.84 (0.01)
C6-WT-AuNKNCs 30 eq	0.0625	25.04	1.21 (0.14)	1.99 (0.01)	-	-	-	-	-	-
C6-WT-AuNKNCs 100 eq	0.1385	12.24	1.19 (0.22)	1.99 (0.02)	-	-	-	-	-	-

** Most likely due to secondary scattering events.*

FT-EXAFS also revealed exciting changes in the structure of AuNKNCs upon interaction with CTPR proteins. For example, spectral analysis from C6-16cys-AuNKNCs suggested both significant Au-O/N and Au-S contributions in the assembly of the clusters. Bond lengths for Au-O/N and Au-S were 1.98 Å and 2.32 Å, respectively. However, while the importance of Au-O/N in C6-16cys-AuNKNCs conjugates decreased with increasing amounts of AuNKNCs, Au-S contribution to the structure of the AuNCs was not altered. Furthermore, the spectra of C6-16cys-AuNKNCs protein conjugates did not contain metallic contributions from Au-Au bonds commonly present in NPs and NCs with well-formed metallic cores. Equally, the FT-EXAFS spectra of C6-16his-AuNKNCs were dominated mainly by Au-O/N contributions (bond length 1.97 Å) and small amounts of Au(I)-Cl (bond length 2.32 Å; Table S2 in Annex 1), with no or little importance of Au-Au bonds (only a small contribution when the protein reacted with increasing amounts of AuNKNCs). Au-O/N contributions (bond length 1.99 Å) also dominated the FT-EXAFS of control system C6WT-AuNKNCs, independently of the quantities of AuNKNCs used to coordinate onto the protein. Still, a small peak between R 2.3-2.7 Å was observed for samples containing both AuNKNCs and the WT protein, which is most likely a multiple scatterings event, although it could also indicate possible Au···Au aurophilic interactions [148,150,159]. Instead, C6-16glu-AuNKNCs showed a combination of Au-O/N (bond length 1.94-1.98 Å) and significant Au-Au single scattering contributions (bond length 2.83-2.84 Å), suggesting a strong Au(0) character for the NCs bound to those proteins. However, the size of the NCs when C6-16glu reacted with 30 or 100 equivalents of AuNKNCs are smaller than the unreacted ones, as estimated from the Amplitudes (S_0^2*CN) obtained from the FT-EXAFS fitting (Figure 2.17 and Table 2.2).

The evidence extracted from the EXAFS and XANES analysis points towards a change in the metallic character of the AuNKNCs, which is lost upon protein coordination with both types of his-based and cys-based CTPR protein scaffolds designed to bind to the NCs. The main component in AuNKNCs is the Au-Au bond, with an amplitude (S_0^2*CN) of 7.1 (Table 2.2), in agreement with a cluster core of metallic nature. In the case of the C6-16cys protein, the coordination is, as expected, predominantly directed by the sulfur present in the cysteines, although some Au-O/N coordination is also contributing, probably from few lysines and glutamic acids present in CTPR scaffolds. The lack of Au(0) signals could relate to a coreless AuNC structure, such as Au-SR stapled catenanes, as reported previously on FT-EXAFS analysis of BSA-templated AuNCs[132]. The interesting photoemission properties of Au(I) – thiolate structures have been extensively studied[131,140] and rise as a good candidate for the type of cluster observed in C6-16cys-AuNKNCs.

On the other hand, the coordination between C6-16his and AuNKNCs shows the main contribution from Au-O/N bonds. This contribution is expected from the high amount of active nitrogen atoms in the protein, and together with a lack of realistic signals from Au-Au interactions, should indicate the presence of Au-N stapled clusters. Besides, evidence points to the stability and PL enhancement effect N/O-containing groups such as amines or carboxylic acids have in photoluminescent protein-templated AuNCs [148,150,159] and, more importantly, the impact that amine-rich proteins have in shifting AuNCs PL towards blue [137]. The glutamic acids present in the C6-16glu protein also seem to direct the binding of AuNKNCs. However, they do it without altering their metallic nature significantly (Table 2.2), as observed by the presence of Au-Au interactions in C6-16glu samples and the coordination numbers particle diameters estimated from the EXAFS spectra. Instead, the original CTPR scaffold (C6-WT) without any

differential designed coordination residue displayed the expected general Au-O/N coordination, representing non-directed coordination, in opposition with the data extracted for the designed protein scaffold holding specific coordination residues geometrically tinkered alongside one verge of the protein.

XANES and EXAFS results combined with the PL studies suggest that the sole coordination by primary amine-containing or carboxylic groups on the WT and C6-16glu proteins is insufficient for an effective PL. In opposition, the PL observed in C6-16cys-AuNKNCs could rise from the interaction between the metal and thiols: LMCT and LMMCT transitions possibly due to the presence of new Au(I)-S bonds. Charge transfer from the sulfur to the Au(I) atom, most likely via a metal-centered triplet state, could explain the appearance of phosphorescence, manifested by a red emission shift and long µs lifetimes [161]. On the other hand, the high concentration in a reduced space of active imidazole groups in C6-16his-AuNKNCs could compensate for the lack of a strong Au(I)-SR interaction since imidazole can act as a coordinating group as well as a reductant. Moreover, the synthesized C6-16his-AuNKNCs resemble histidine-capped AuNCs holding intense blue PL with lifetimes at the nanosecond regime [151,160]. The Au(I)-N bond directed by the imidazole seems key to explaining the fluorescent properties of C6-16his-AuNKNCs, arising from optical transitions across the discrete molecular-like AuNC levels.

2.4. Conclusions

Protein-based AuNCs have risen as excellent biocompatible nanomaterials with valuable properties given by their PL and the molecular recognition capacities derived from proteins. Recently, the efforts to comprehend the nature of the PL from such hybrids have shed light on the importance of

ligands and synthesis conditions. These investigations, which represented the initial steps to study these relevant effects, were developed using natural and widely used proteins and peptides such as BSA, OVA, or GSH and *in situ* methodologies for the NC synthesis.

Herein, rational design has been used on simple scaffolding proteins, CTPRs, to explore the effect of the coordinating protein on the PL properties of originally non-emissive AuNKNCs through engineering specific coordination residues on the same protein scaffold. Additionally, the selection of previously described water-dispersible non-emissive AuNKNCs allowed us to use the same nanomaterial to solely study the effect of the protein capping, without additional coordination/ reduction effects from the protein environment on the *in situ* synthesis methods of metal nanoclusters.

Besides, an extensive optical and X-ray spectroscopical characterization of the designed protein-AuNKNCs composites sheds light on the mechanisms underlying the relationships between the NC composition and the metal coordination by biomolecules and optical properties of metal NCs. Interaction of unstabilized nanoclusters with proteins carrying engineered metal coordination sites showed dramatic differences depending on the chemical nature of those amino acids. Proteins based on glutamic acid maintained the metallic nature of the AuNKNCs bond. However, those carrying lysine, histidine, or cysteine transformed the structure of the clusters radically, losing their Au-Au metallic core and maybe being transformed into Au-N/S stapled type structures. These Au-amino acid interactions also seem to control the resulting photophysical properties of the clusters, allowing to switch and tune the PL of nanoclusters effectively.

Finally, the reported synthesis method that combines engineered coordinating modules and naked nanoclusters offers a quick, green, and

easy way of developing emissive systems with tunable PL emission wavelengths and lifetimes.

Engineered repeat proteins can be envisioned as tailored, modular protein-based systems for the control interfacing of biomolecules with nanomaterials towards 1) the fundamental physicochemical studies on the properties of emerging the bio-nano hybrid materials with advanced properties, and 2) the design of future multifunctional protein-hybrids with customized PL properties for a broad range of applications.

2.5. Experimental section

2.5.1. Protein expression and purification

Proteins were over-expressed using *Escherichia coli* C41 cells. Overnight saturated cell culture was diluted and grown until the optical density reached 0.6 at 37°C. At this point, the protein expression was induced using 0.6 mM of Isopropyl β-d-1-thiogalactopyranoside (IPTG), and the cells were grown at 30°C for 5 hours. Overexpressed proteins were purified using the His-tagged fusion method in a nickel nitriloacetic acid (Ni-NTA) affinity chromatography column, and His tag removed using tobacco etch virus (TEV) protease. Then, electrophoresis gels were used to confirm the molecular weight and the purity of the purified proteins. The protein concentration was estimated using the molar extinction coefficient calculated from their amino acid composition. Purified proteins were stored at -80°C.

2.5.2. AuNKNCs synthesis

The synthesis of the naked AuNKNCs was developed by Prof. Prieto's laboratory (Instituto de Ciencia Molecular (ICmol) at Universitat de València)[163]. Briefly, AuNKNCs were synthesized by mixing a NaOH

solution (440 µL, 2M) with water (860 µL) and then adding an aqueous solution of HAuCl4 (25 µL at 50 mM HAuCl4; at a NaOH/Au molar ratio of 704/1). The mixture became colorless immediately and was kept without stirring for one hour.

2.5.3. AuNKNCs conjugation to proteins

After the synthesis of AuNKNCs, the pH is adjusted using HCl, and the protein is added in a molar ratio of 30/1 HAuCl4/protein. The mixture is left overnight under stirring and covered from light. Then, the sample is washed and concentrated using an Amicon 3 kDa ultrafiltration device. For the screening of conditions, the reagents and proteins were mixed in a microplate: AuNKNCs were synthesized as mentioned before *in situ* in each well, keeping the same molar ratios of gold and NaOH as exposed in the AuNKNCs synthesis. After one hour, the protein was added to a final fixed concentration of 20 µM and left overnight. The photoluminescence was registered using a Biotek Synergy H1 plate reader, with a λ_{ex} of 370 nm under aerobic conditions (Figure 2.6).

2.5.4. TEM imaging

TEM measurements were conducted on a JEOL JEM 1400 Plus microscope (120 kV). The samples for TEM were prepared by drop-casting of the protein solution at 100 nM concentration over a TEM grid and blotted to dry. The analysis of the images was performed using ImageJ software.

2.5.5. MALDI-TOF MS analysis

Mass spectra were acquired on an UltrafleXtreme III MALDI-ToF mass spectrometer with delayed extraction (Bruker) accoutered with a pulsed N2 laser (λ= 337 nm). MALDI-TOF sample preparation included 2 µL of the sample mixed with 2 µL of sinapic acid (matrix) in 50:50 water/acetonitrile

with 0.01% trifluoroacetic acid (TFA). Thus, 1 μL of the mixture was deposited onto the MALDI plate and air dried. All mass spectra were acquired in positive reflection mode using delayed extraction with a range of 50−100 laser shots and an excitation voltage of 20 kV.

2.5.6. X-Ray Photoelectron spectroscopy

X-ray photoelectron spectroscopy measurements were executed with a SPECS SAGE HR 100 spectrometer accoutered with a 100 mm mean radius PHOIBOS analyzer and a nonmonochromatic X-ray source. An Mg Kα line of 1253.6 eV energy and 250 W was placed perpendicular to the analyzer axis and calibrated using the 3d5/2 line of Ag, with a full width at half maximum of 1.1 eV. An electron flood gun was used to neutralize the charge. Measurements were conducted directly on dry deposited films in an ultrahigh vacuum chamber at a pressure of 8 × 10–8 mbar. The analysis of spectra was done with CasaXPS 2.3.15dev87 software. Spectra were charge-corrected by fixing the adventitious carbon C sp3 at 284.8eV.

2.5.7. Optical and Photophysical Spectroscopy

Absorbance spectra of protein-AuNKNCs conjugates were acquired on a 96-well microplate using a Biotek Synergy H1 plate reader. For time-resolved PL measurements, a 405 nm PDL 828 Picoquant Sepia laser with a 50 ps pulse duration was employed as a photoexcitation source. The repetition rate was set at 10 MHz, and the beam was mildly focused on the sample. Photoluminescence measurements were carried out in solution in 2 mm optical path quartz cuvettes. Samples were purged with N_2 prior and stirred while measuring. A 420 nm long-pass filter was used to remove scattering from pump pulses. Photoluminescence was collected with a pair of achromatic, convergent lenses (2” diameter and a focal of 7.5 cm) and sent to an SP2500 Acton Research spectrometer to select the desired spectral window in an N_2-cooled CCD (Princeton Instruments). Two

different excitation/detection configurations were employed to monitor the nanosecond and microsecond time domains. PL decay measurements in the ns-time region involved excitation with the 405 nm picosecond diode laser described above with a repetition rate of 10 MHz and acquisition with a PicoQuant HydraHarp-400 time-correlated single-photon counting (TCSPC) system. Analogous measurements in the µs time-domain involved excitation with a 355 nm passively Q-switched Nd:YAG laser (TEEM Photonics; 0.3 ns pulse duration, at 269 Hz repetition rate) and acquisition with a TimeHarp 260 TCSPC board. PL spectra were acquired by filtering the desired wavelength with a spectrometer (SP2500, Acton Research) and detected with a Picoquant PMA Hybrid-Photomultiplier Assembly with a transit time spread of less than 50 ps. PL decay analysis was carried out with Fluofit software (Picoquant). The phosphorescence origin of C6-16cys-AuNKNCs emission was assessed bubbling the sample with O_2 and afterward bubbling with N_2. Solutions were purged for 3 minutes (Figure 2.11).

2.5.8. Thermal stability vs. photoluminescence measurements

Photoluminescence was measured in a Biotek Synergy H1 plate reader conducting thermal denaturation ramp from 20°C to 100°C and from 100°C to 20°C every 10°C, using a λ_{ex} at 390 nm. The secondary structure of the protein-AuNKNCs conjugates was checked using circular dichroism (CD) on a spectropolarimeter Jasco J-1500, with a PM-539 detector and a 150W Xe arc excitation lamp. CD spectra from 260 nm to 180 nm were measured at 20ºC and 100ºC using a scanning speed of 200 nm/min and 5 accumulations, a bandwidth of 5 nm, a data pitch of 0.2 nm, and a DIT of 0.5 s. The CD signal was recorded at 220 nm for the thermal denaturation ramps using a JP Selecta Tectron Bio thermostat controller.

2.5.9. Trypsin digestion

Protein-AuNKNCs samples were incubated with increasing molar equivalents of trypsin from porcine pancreas (Sigma Aldrich, CAS 9002-07-7), from 10:1 (trypsin:CTPR conjugates) to 1000:1 in 10X increments, and were incubated for 1 h. Photoluminescence of the protein-AuNKNCs conjugates was measured on a Biotek Synergy H1 plate reader at λ_{ex}=390 nm. In addition, polyacrylamide gel electrophoresis was performed to check the protein integrity after trypsin digestion, running the digested samples with incremental amounts of trypsin at 200 V.

2.5.10. X-Ray Absorbance Fine Structure (XAFS)

X-ray Absorption Spectroscopy data were collected at B18 beamline at Diamond Light Source at the Au L3-edge (11919eV) using Cr-coated mirrors and a Si111 monochromator. Samples were measured in liquid form inside plastic Eppendorf tubes at concentrations over 0.1 mg/ml of Au. Data collection was performed in fluorescence mode employing a 36-element solid-state Ge detector positioned at 90 degrees from the incoming beam. Energy scans were performed from 11719 to 12919 eV (k-range up to 16 $Å^{-1}$) with a constant energy step of 0.3 eV and a total acquisition time of ca. 3 minutes per scan. Scans were repeated from 50 to 100 times per sample and then averaged (where the number of repetitions was selected depending on Au concentration and XAS signal). The resulting spectra were from the I_F/I_0 signal, measured by an ion chamber placed before the sample and filled with ca. 70 mbar of Argon and up to 1 atm He (resulting in absorption of ca. 10% of the incoming beam).

The standards used contained a mixture of the expected oxidation states present in the AuNKNCs and protein samples and some of the possible ligands bound to the Au once coordinated to the inner interface of the proteins studied. In particular, those standards included: Au(0) foil; Au(III)

hydroxide; Au(I) Cl; Au(I) sulfide; and Au(I) cyanide. Those standards were obtained from the XAS standard database provided by Hephaestus software, while Au(I) Cl was measured experimentally at the I14 beamline (Diamond). The measurements and standards were calibrated using corresponding Au foil scans to align the edge to 11919 eV.

Data processing and analysis were then performed with Athena and Artemis software from the Demeter package using the IFEFFIT code[164]. Initially, Principal Components Analysis was run on the series of Au samples in the XANES region (-20 to +80 eV around the edge), and target transform was applied on a series of Au standards (including Au(0) foil, Au(III) hydroxide, Au(I) chloride, Au(I) sulfide, and Au(I) cyanide) to confirm their presence as components in the samples measured. XANES linear combination fits (LCF) were then performed in the range -20 to +80 eV around the edge using the standards mentioned above.

EXAFS fits were performed in the k-range (from 2.5 to 15.5 $Å^{-1}$). R-range varied from 1 to 2.4 Å (when only fitting the first shell) or from 1 to 3.4 Å (when also Au-Au signal was included in case of a significant fraction of metallic gold). In the absence of a 3d structure, only single scattering paths were used for the fit, including Au-O/N, Au-Cl, Au-S, Au-Au. Most of the parameters were left free to be optimized by the fits, but values obtained by the fit of Au standards were used as starting guesses when possible. However, Debye-Waller for Au-O/N was fixed to 0.002 $Å^{-2}$ as found from the fit of the Au(III) hydroxide standard, the decision to fix it was due to its strong correlation to the amplitude parameter. E_0 was optimized to different values for different paths because they are representative of fractions of the sample where Au atoms are in various oxidation states. Coordination Numbers (CN) were left free to be optimized by the fit and were obtained using a single parameter for amplitude representing the product of S_0^2* CN.

3.SENSING APPLICATIONS OF METAL NANOCLUSTERS TEMPLATED BY ENGINEERED PROTEINS

3.1. State of the art

The IUPAC defines a chemical sensor as 'a device that transforms chemical information, ranging from the concentration of a specific sample component to total composition analysis, into an analytically useful signal'. Equally, it also defines a physical sensor as 'a device that provides information about a physical property of the system'[165]. Both type of sensors are extremely useful for extracting information from their environment and have been used and perfected since ancient times[166,167]. Nonetheless, ordinary methods to measure physical variables such as temperature, pressure, humidity and mass change, or chemical parameters like acidity, presence of molecular species and electric conductivity are constructed for giving responses in meso- and macro- scales, so these spatial resolutions are not sufficient to probe micro- and nano-scale environments. New tools for measuring physical and chemical parameters are needed in a world in which we require better sensitivity and reliability at those smaller scales, given the importance of the phenomena that occurs at the nano and micro settings, for example, the significance of tumor microenvironment (enhanced temperature, inflammation) in tumor cell growth[168,169].

Photoluminescent metal NCs have been widely used as sensors because luminescence emission can be encoded to change in response to specific modifications in their environment, including fluctuations in temperature, oxidative stress imbalances derived from cellular metabolism, acidity, or the presence of different substances like metal ions, or biomarkers. In this way, the precise information about the physicochemical status extracted from the microenvironment could be used to evaluate the best actions to be taken, e.g., therapeutic treatments for a patient or ecological interventions in a polluted location.

3.1.1. Temperature sensing and nanothermometry

Temperature is a fundamental thermodynamic variable and one of the environmental parameters with a critical influence on living organisms. In the case of environments at the micro and nanoscale in biological systems, temperature is a crucial trigger of chemical and physical dynamic processes, controls metabolism and thermodynamic mechanisms, but can also become an early sign of relevant phenomena such as inflammation[163]. However, traditional thermometers cannot measure on the sub-micrometer scale, especially in environments with fast thermodynamic changes, such as the intracellular environment. Thermoresponsive nanomaterials are one way to measure temperature at the nanoscale, as well as suitable actuators that respond to thermal stimuli. The importance of accurately measuring temperature at micro and nano scales emerges from the role that heat variations, called hyperthermia or hypothermia, have in living organisms across several pathologies (e.g., tumor growth, inflammation, or stroke[164]). Besides, heat can be used for treatments, but it must be precisely controlled for safety issues. For example, hyperthermia therapy is a commonly used anticancer treatment in which the temperature of the malignant cells is raised above physiological levels (around 42º C) using irrigations with solutions at the required temperature[170]. However, the treatment can be more focused and less harmful for healthy tissues using tumor-targeted metallic nanoparticles that can produce heat when externally activated using light (photothermal therapy or PTT)[40] or magnetic stimulation (magnetic hyperthermia therapy or MHT)[172]. In this sense, the accurate temperature measurement at the nanoscale becomes a grounding step for any thermal-related therapy or studied phenomena.

Several approaches have already been taken for sensing temperature at the nanoscale, such as the use of organic dyes[170], carbon dots[177], quantum dots, fluorescent proteins[175,176], or photoluminescent metallic clusters[178], in

which emission intensity varies along with temperature ranges. Even more complex techniques like XAS[179] have been used for such endeavors. However, nanothermometry has different limitations that have to be accounted for. Notably, for many thermoresponsive nanomaterials, their toxicity (for example, in quantum dots due to their heavy metal composition), low biocompatibility, stability in biological media, and minor sensitivity are substantial burdens for their use in cellular organisms. However, thermal responsiveness endowed with biomolecular recognition is an interesting feature since the nanothermometer can be targeted to specific tissues expressing a biomarker or to distinct intracellular compartments when using proteins as templates of the thermoresponsive nanomaterial. Equally, this approach could help to enhance the biocompatibility of such nanomaterials, by using non-toxic biomolecules. Some efforts have previously been made in this direction using protein-passivated metal nanoclusters[180–182]. Nevertheless, they have limitations such as hysteresis, *i.e.*, the differential response the thermometer has at a given temperature when performing temperature heating or cooling ramps, common in temperature sensors and which makes measurements unreliable, and a low range of temperature sensitivity (typically from 4ºC to the temperature at which the protein is still stable and folded, usually below 60ºC). The low range of temperature sensitivity is not a handicap when measuring ordinary biological samples, because they usually lie in within the operation range, but can be problematic in the case of extreme environments and extremophile organisms (for example, bacteria living in submarine fumaroles).

3.1.2. Chemical sensing

Sensors can be designed not only to measure physical variables but also to identify the presence of specific molecules and assess the chemical

environment, for instance, pH levels. The pursuit of a device for chemical and molecular sensing has driven the efforts in the field towards innovative proposals, such as electronic noses and chemical tongues[183–186]. The complexity of these devices relies on a sensor array that can deal with a heterogenous input of molecules for complex detections. However, much simpler chemical detectors can be designed, especially using nanoparticle-based devices sensitive to metal species or redox processes[187], such as the formation of reactive oxygen species (ROS)[188]. In particular, the detection of heavy metals[183–186] or rare-earth elements[190] could be relevant for determining contaminants in food and the environment, or assessing the availability of chemical resources for mining.

Detection of molecules has remarkable relevance in health monitoring. In this field, the relevant molecule to be detected becomes a biomarker. The National Institute of Health (NIH, USA) defines a biomarker as a characteristic of an organism that is objectively measured and evaluated as an indicator of normal biological processes, pathogenic processes, or pharmacological responses to a therapeutic intervention[180,191,192]. Biomarkers used in diagnostics must be detectable in samples easy to obtain from the patient (*i.e.*, in bodily fluids like blood, urine, saliva), and provide information to allow early diagnosis and treatment[143,193]. Biomarkers are typically used to diagnose a disease, assess its prognosis, and predict the efficacy and safety of a drug. Therefore, it is necessary to differentiate between disease-related or drug-related biomarkers. The first one informs about the effect of a treatment or the progression of the disease[184,194–196]; the second one predicts drug efficacy and response in patients.

DNA[197] and protein[198,199] have been used for templating nanomaterials for sensing purposes, and design can further increase complexity by adding logic gates[184,194–196] or chemoresistors[22,144,179,191]. Those elements might include logical operators, switchers and simple computation to the sensing

device, and increase the reliability of the detection. Apart from other photoluminescent nanostructures, for instance carbon dots and quantum dots, NCs have been widely used for chemical sensing and detection of ions, such as Cu^{2+} [198,199], or toxic metals like Hg^{2+} [202]. Particularly, AuNCs are a popular sensor option given their chemical stability and low reactivity with other components of the cellular medium. Furthermore, the importance of biological and cellular processes has fueled the recognition of biomolecular sensing as an important section of chemical sensing, in which the development of photoluminescent nanoprobes, including metallic NCs, is bursting.

The use of nanoclusters as fluorescent reporters to detect chemical species and biomarkers is increasing due to their stability, tunable optical properties, and the wide variety of biomolecules with recognition capabilities used for their conjugation[203,204]. For this purpose, NCs are commonly synthesized using a templating strategy that avoids NCs aggregation, leading to stable nanomaterials of a specific size. Since NCs radius (i.e., the number of atoms comprising the clusters) and ligands define their fluorescence properties, using templating agents is translated into a defined size and optical properties. In addition, the templating molecule can also provide recognition capability for molecular targets. Therefore, nanoclusters synthesized following this strategy might have selectivity for the analyte and tunable fluorescence properties that allow the target molecule's specific recognition, detection, and quantification.

Many research lines focused on sensing develop nanoparticles, quantum dots, and nanodots. In particular, the number of publications related to NCs is increasing since they have a great potential for chemical detection due to their tunable properties. In particular, their photoluminescence (PL) is an interesting property that can be used both in PL spectroscopy and

fluorescence imaging, although PL spectroscopy is the appropriate technique if more accurate quantitative results are required. The key to using NCs as fluorescent reporters in biosensing strategies is to tune their optical properties, leading to their specific detection and quantification. Designed proteins for the precise synthesis of metal nanoclusters and tailored specificity is, in this sense, an intelligent approach to cover different biosensing needs (Figure3.1).

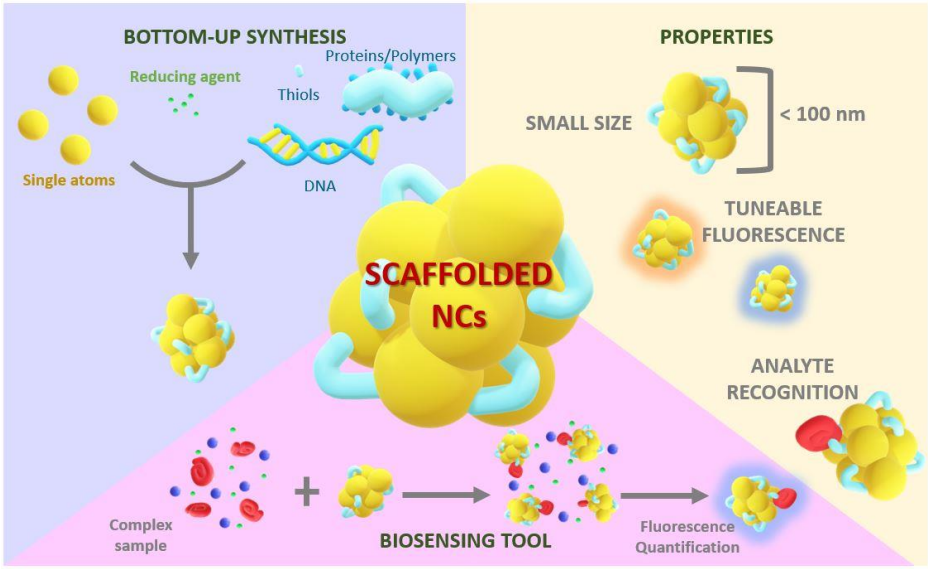

Figure 3.1. Overview of bottom-up synthesis of bio-templated metal NCs, their properties and their use as biosensing tools.

3.2.Approach

Protein engineering can be used for designing functionalized tools that can fulfill a set of desired requirements or perform a specific action. Simple modular proteins are excellent to use as templates for creating functional nanostructures because of their stability properties, modularity, and structure. For example, in a consensus tetratricopeptide repeat (CTPR),

only 8 residues of the 34 within each CTPR repeat are conserved and have structural significance, leaving plenty of space for mutations and changes alongside the protein. In the past, an easy way to template metal nanoclusters on a CTPR protein with specific binding capability (Hsp90) was showed, and the use of this system to build a fluorescent probe that recognizes the CTPR target molecule and reports the binding through a change in the PL[92]. In the present work CTPR templated metal nanoclusters for sensing different stimuli, such as temperature, ions, and reactive oxygen species (ROS) is explored, with the primary objective of developing an array of modular sensing tools that could be combined in the same protein scaffold.

3.3. Results and discussion

3.3.1. Protein design and NCs synthesis

Blue fluorescent protein stabilized metal NCs were synthesized in one step by reducing the metal salt ($HAuCl_4$, $AgNO_3$, or $CuSO_4$) with sodium ascorbate in the presence of a CTPR protein with 3 modules, in which the last one bears a C-terminal cysteine (C3_cys), at 37°C for 72 h. The as-obtained protein stabilized metal NCs suspension are light brown under visible light (Figure 3.1A) and emit strong blue fluorescence under 365 nm irradiation (Figure 3.1B). The UV-visible spectra (Figure 3.1C) of the protein-stabilized metal compared with the spectrum of the protein at the same concentration showed, in addition to the characteristic protein absorption at 280 nm, the presence of small and broad peaks around 350-370 nm, and in the case of AuNCs a slight rise around 560 nm due to the presence of a small fraction of gold nanoparticles. The fluorescent protein-stabilized metal NCs showed maximum excitation and emission peaks at

375 and 453 nm (CuNCs), 371 and 445 nm (AgNCs) and, 365 and 438 nm (AuNCs), respectively (Figure 3.1D).

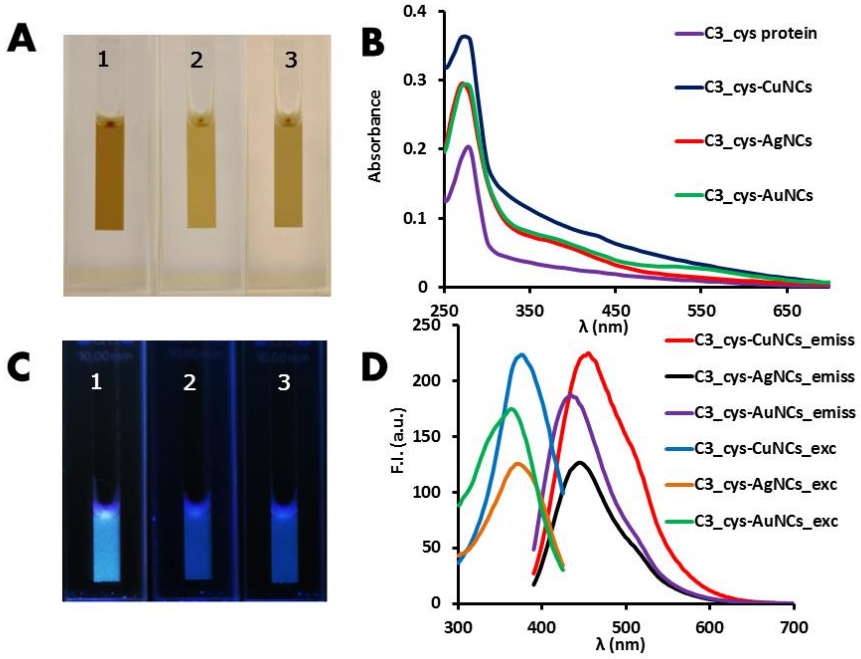

Figure 3.1. PL characterization of metal NC-CTPR protein conjugates. A and C) images of CTPR-metal NCs solution under visible light and UV light: C3_cys-CuNCs (1), C3_cys-AgNCs (2), and C3_cys-AuNCs (3). B) UV-Vis absorption spectra of the non-conjugated CTPR protein and the synthesized protein-NCs conjugates. D) Excitation and emission spectra of CTPR templated NCs.

The fluorescence quantum yield (Φx) of C3_cys-CuNCs, C3_cys-AgNCs, and C3_cys-AuNCs were 4.1, 2.6, and 3.5%, respectively, when anthracene was used as a reference. These values are in the same range as those reported for other protein-stabilized fluorescent metal NCs in the literature [183,200,201].

MALDI-TOF mass spectrometry was used to determine the size of the NCs. The spectra of the protein-NCs complexes showed clear shifts compared to the spectrum of the protein. However, the peaks in the mass spectra that correspond to the protein-NCs conjugates were broader than the pure protein peak, indicating the presence of protein populations with different numbers of metal atoms. Thus, it is possible that the laser irradiation during the MALDI-TOF acquisition was etching the NCs bound to the proteins. For example, the mass spectrum of C3_cys-CuNCs (Figure 3.2) showed a prominent peak at m/z= 14,693.34 Da, corresponding to C3_cys-CuNCs with six copper atoms per protein (compared to an m/z= 14,321.65 Da for the free protein). Similarly, the mass spectrum of C3_cys-AuNCs showed a peak at m/z= 14,869.47 Da, indicating three gold atoms per protein, and the mass spectrum of C3_cys-AgNCs showed a peak at m/z= 14,789.94 Da that corresponds to five silver atoms per protein. It is plausible that other NCs species were also formed; however, they were not clearly detected by MALDI-TOF mass spectrometry.

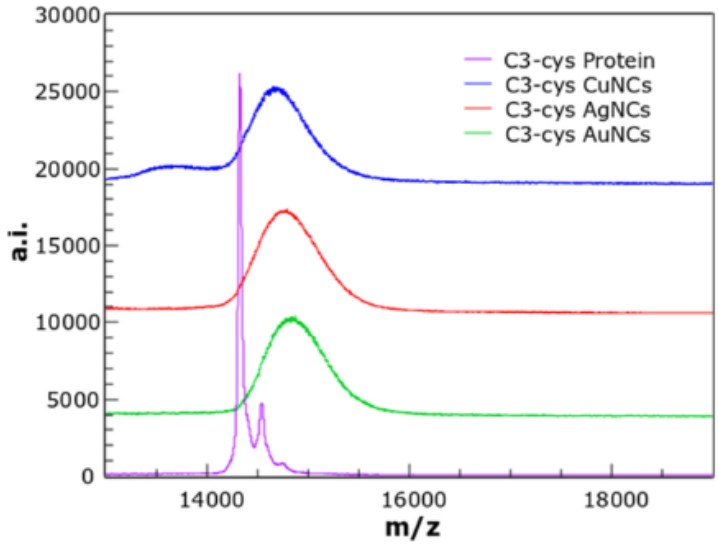

Figure 3.2. MALDI-ToF analysis of metal NC-CTPR conjugates. Mass spectra of non-conjugated C3_cys protein (magenta trace) and the protein-NCs conjugates: C3_cys-CuNCs (blue trace), C3_cys-AgNCs (red trace), and C3_cys-AuNCs (green trace). The shifts in the peaks relative to the protein spectrum correspond with the absorption of six Cu atoms, five Ag atoms, and three Au atoms.

3.3.2. Temperature sensing

The photoluminescence (PL) of protein stabilized metal NCs was tested under a temperature range from 25°C to 60°C (Figure 3.3). The fluorescence decays up to 40% in all the NCs evaluated, no matter the metal of choice (Figure 3.3D, 3.3E, and 3.3F). Potential hysteresis effects may hamper the use of a sensor as a reliable nanothermometer. Thus, it is important to evaluate that the fluorescence intensity at a specific temperature is not dependent on the heating or cooling cycles and remains the same when the system is being heated up or is cooling down. Hysteresis effects may emerge from local conformational changes of the protein in the surroundings of the metal NC [207,208]. However, CTPR proteins

present good thermodynamic stability under the temperature range in which the sensor was evaluated and a fully reversible thermal denaturation [209]; therefore, these scaffolds guarantee a system without hysteresis.

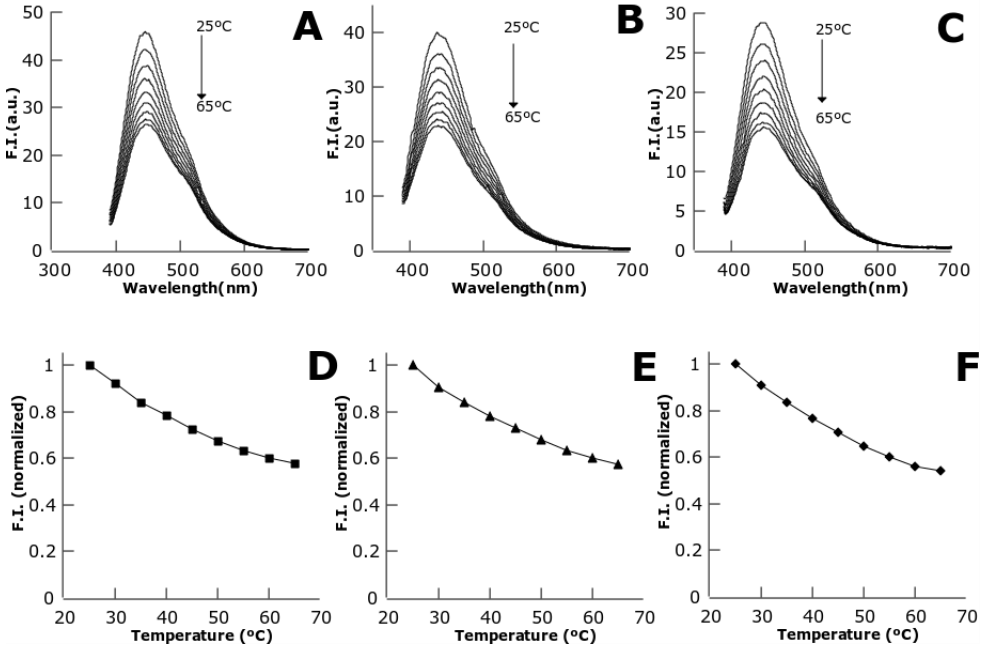

Figure 3.3. Metal NC-CTPR conjugates as temperature sensors. CTPR-templated NCs emission spectra under a temperature gradient from 25°C to 65°C (upper row) for C3_cys-CuNCs (A); C3_cys-AgNCs (B) and C3_cys-AuNCs (C). Normalized fluorescence intensity vs. temperature (lower row) for C3_cys-CuNCs (D); C3_cys-AgNCs (E) and C3_cys-AuNCs (F).

The stability of the fluorescent signal from the metal NCs through different cycles of temperature was also tested. It is observed that the metal NCs can undergo heating and cooling cycles from 25°C to 60°C without losing the temperature response and the resolution of the detection (Figure 3.4). CTPR-templated metal NCs can perform several cycles without losing

fluorescence or temperature sensitivity, making them robust temperature sensors.

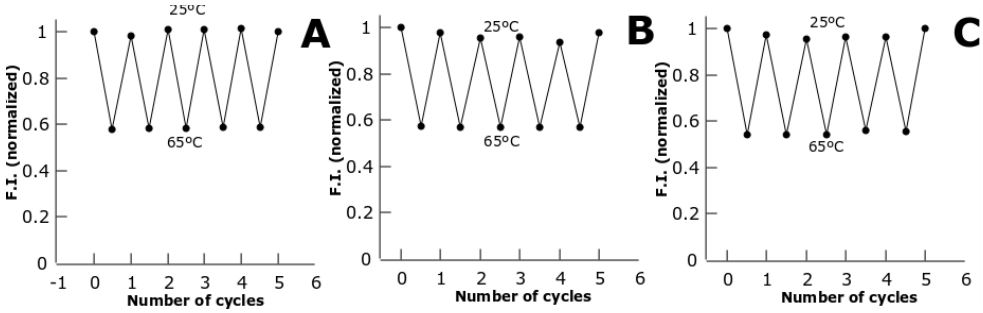

Figure 3.4. Cycles of temperature sensing. Normalized fluorescence intensity vs. the number of temperature cycles between 25°C and 65°C for C3_cys-CuNCs (A), C3_cys-AgNCs (B), and C3_cys-AuNCs (C).

3.3.3. Ion detection

Several ions were tested as targets for the sensing properties of the protein-stabilized metal nanoclusters. Among these ions, only copper showed a significant quenching of the fluorescence emission of the metal nanoclusters for each of the nanocluster compositions (Figure 3.5).

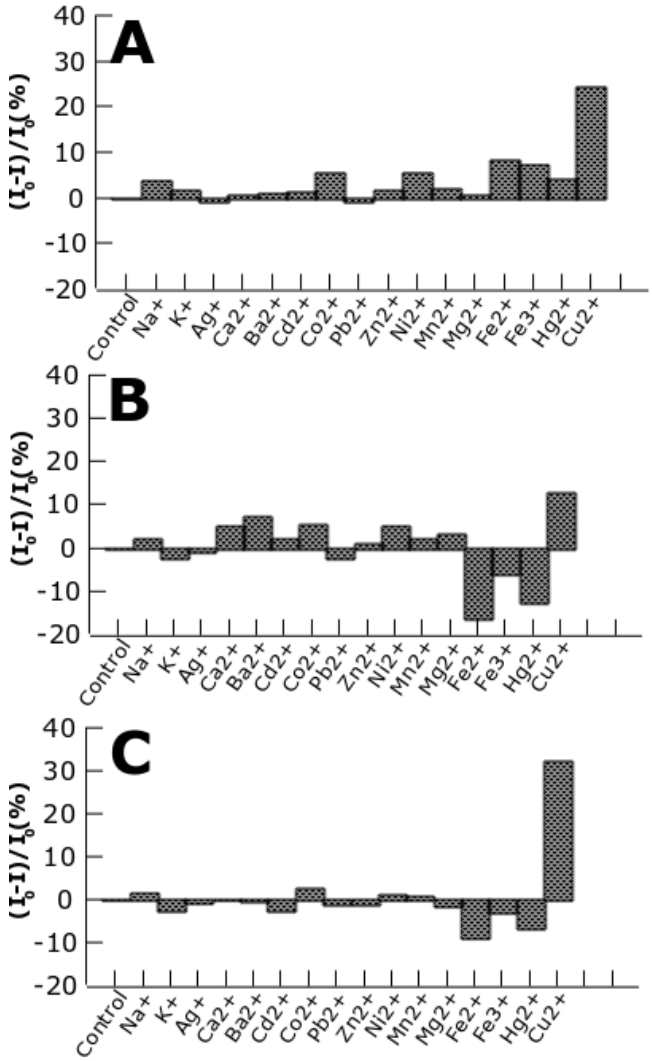

Figure 3.5. Ion detection by protein-stabilized nanoclusters. The change in the fluorescence emission intensity of the protein-stabilized nanoclusters upon the addition of different ions at the same concentration (10 μM). C3_cys-CuNCs (A); C3_cys-AgNCs (B) and C3_cys-AuNCs (C).

Moreover, gold protein-stabilized nanoclusters were the most responsive to Cu^{2+}, quenching up to 40% of the PL at 10 μM of Cu^{2+} (Figure 3.6). This

phenomenon has already been reported in other works based on BSA-AuNCs[210].

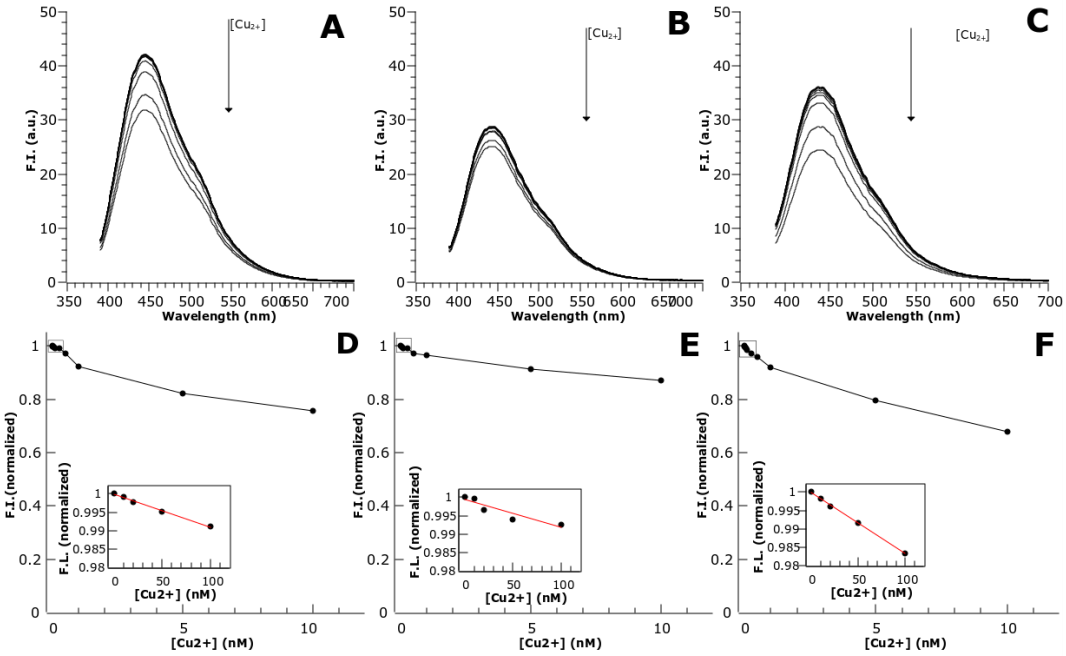

Figure 3.6. Cu detection by protein-stabilized nanoclusters. Fluorescence emission spectra of CTPR templated metal NCs in the presence of different Cu^{2+} concentrations (upper panels) C3_cys-CuNCs (A); C3_cys-AgNCs (B) and C3_cys-AuNCs (C). Normalized fluorescence vs. Cu^{2+} concentration plots (lower panels). C3_cys-CuNCs (D); C3_cys-AgNCs (E) and C3_cys-AuNCs (F).

No studies have been performed to explore the mechanism of fluorescence quenching by copper, but there are some possible explanations for this effect. One possibility is that Cu^{2+}, as a paramagnetic species, can enhance intersystem crossing (ISC) as a mechanism of non-radiative dissipation of the energy absorbed, competing with fluorescence emission and thus quenching the PL of the metal NCs[211]. Another possible explanation is a reaction with Cu^{2+} causing de-attachment of Au NCs from the coordination

residues, thus leading to a loss of PL. However, further characterization would be necessary to detangle copper's molecular mechanism underlying fluorescence quenching.

3.3.4. Reactive Oxygen Species (ROS) detection

The different nanoclusters samples were evaluated as sensors for detecting oxidative stress through reactive oxygen species in the environment. The Ag-based nanoclusters were the only protein-templated nanocluster that showed a reliable response to ROS (Figure 3.7). PL of the Ag-NCs was quenched in response to the amount of ROS produced by Rose Bengal (RB) in time. The quenching occurred slowly in time, with a 10% fluorescence loss in an hour. It is important to note that the positive control used to detect ROS formation, 2,2'-azino-bis(3-ethylbenzothiazoline-6-sulphonic acid (ABTS), showed a more significant response to ROS than the AgNCs.

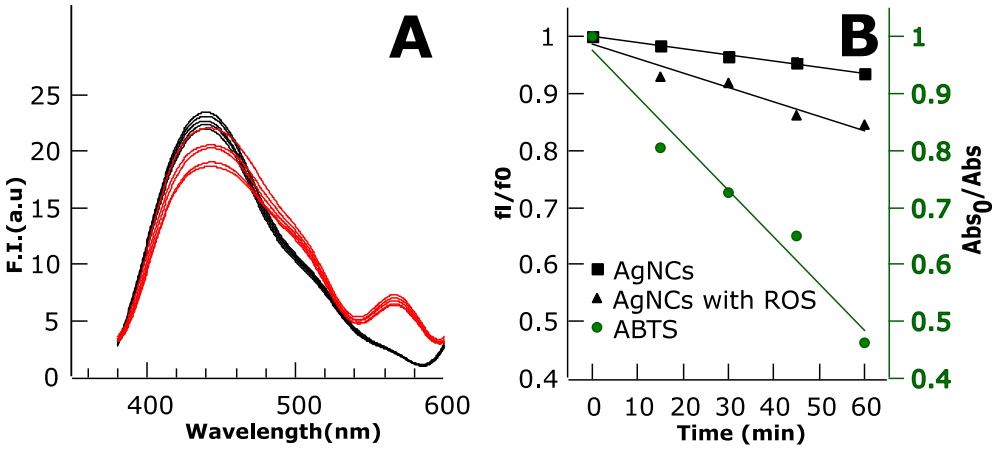

Figure 3.7. ROS detection by CTPR-AgNCs. A) Fluorescence emission spectra of the C3_cys Ag nanoclusters with no ROS control (black lines) and RB NCs, *i.e.*, oxidative environment from ROS production (red lines). B) Stern-Volmer plot showing the quenching of the Ag-NCs fluorescence

with time upon irradiation of RB, related to increased amounts of ROS. ABTS was used as a probe for ROS production; its absorbance was measured to check ROS formation (green spheres, absorbance on green axis).

In the case of the copper nanocluster, an initial quenching of the system before sample irradiation was observed. However, there was no further quenching upon irradiation when ROS were synthesized (data not shown). Thus, RB may be quenching the nanocluster fluorescence due to an interaction between the molecule and the Cu atoms. The mechanism of how ROS quenches the fluorescence in AgNCs is not yet solved in our system. However, considering the low stability to oxidation of the Ag-NCs, oxido-reduction changes on the Ag-NCs directed by ROS activity may induce a quenching in the fluorescence.

3.4. Conclusions

In previous work, we developed new technologies to use designed CTPR proteins for the controlled growth of AuNCs. The main objectives of the current work were: 1) evaluate the potential of repeat protein scaffolds as versatile templates for the synthesis and stabilization of NCs with different metal compositions (Au, Ag, and CuNCs); and 2) explore the use of CTPR stabilized metal NCs as sensors for different conditions, such as temperature, ions, or ROS. The sensitivity of these NCs for temperature sensing and the ability to undergo several temperature cycles without losing sensing efficiency are remarkable. Moreover, AuNCs can detect small concentrations of copper ions in solution, and AgNCs showed sensitivity to ROS species. Although previously reported systems showed similar detection capabilities, and in some cases, with better specificity and detection limits, the primary advantage in CTPR templated metal NCs is

that the same system can encode different sensing capabilities and functionalities by changing the metal attached. Therefore, this work demonstrates the versatility of the repeat protein scaffolds to obtain protein-stabilized nanoclusters with different metal compositions, which increases their potential use in the field of biosensing. Furthermore, due to the modular nature of these proteins, CTPR protein templated metal NCs have a great potential as integrated modules in larger assemblies of CTPR proteins. In this way, multi-component sensing tools using their modularity and different functional elements alongside the protein array could be built.

3.5. Experimental section

3.5.1. Chemicals

All chemicals were purchased from Sigma-Aldrich and used without further purification. Ultrapure reagent grade water (18.2 MΩ, Wasserlab) was used in all experiments.

3.5.2. CTPR protein design and purification

CTPR protein was produced following standard molecular biology protocols for recombinant protein expression. First, the CTPR3_cys protein cloned into a pPro-EX-HTb vector was transformed in *Escherichia coli* C41 (DE3) cells. Next, the cells were grown with ampicillin in Luria−Bertani media (LB). IPTG induced the protein expression at OD = 0.6-0.8. After 16 h expression at 20°C, cells were harvested, and the his-tagged proteins were purified via affinity chromatography using Ni-NTA resin. Next, the his-tag was cleaved using TEV protease, and a second Ni-NTA affinity column purification was performed to remove the his-tag and the TEV protease from the protein sample. Finally, the protein concentration was determined by absorbance at 280 nm using the extinction coefficient calculated from the amino acid

composition. The CTPR3 with an additional cysteine residue at the C-terminal (C3_cys) has the following amino acid sequence:

GAMDPGNSAEAWYNLGNAYYKQGDYDEAIEYYQKALELDPNNAEAWY NLGNAYYKQGDYDEAIEYYQKALELDPNNAEAWYNLGNAYYKQGDYDE AIEYYQKALELDPNNAEAKQNLGNAKQKQGC *(Molecular weight: 14463.4 daltons)*.

3.5.3. Synthesis and characterization of protein stabilized metal Nanoclusters

The protein-stabilized metal NCs were synthesized following a previously reported procedure using sodium ascorbate instead of ascorbic acid to provide a reducing environment[92]. Briefly, 1000 µL of protein at 10 µM were mixed with $HAuCl_4$, $AgNO_3$, or $CuSO_4$ (5 µL 10 mM, 5 eq. related to protein) for at least 30 minutes to allow the adsorption of metal ions to the protein's stabilizing sites. Then, the reduction of the metal ions to metal NCs was achieved by adding 5 µL of sodium ascorbate at 100 mM (10 eq. related to metal ions). The reaction was incubated at 37°C for 72 h. Next, the samples were concentrated to 500µL using Amicon ultrafiltration tubes with a 10-kDa membrane. Finally, the unreacted salts were removed by gel filtration chromatography using an Illustra NAP-25 column. The purified samples were kept at 4°C for further experiments. The absorption and fluorescence spectra of protein stabilized metal NCs were recorded using a spectrophotometer UV-Vis (Jasco V630-Bio) and a fluorometer (Perkin Elmer LS55).

3.5.4. Fluorescence quantum yield

The fluorescence quantum yield (Φx) was calculated using anthracene in ethanol as a reference (Φ_{ref} = 0.27, λexc = 370 nm, and λem = 423 nm) and the following formula:

$$(1)\ \phi_x = \phi_{ref} \frac{Grad_x}{Grad_{ref}} \left(\frac{{\eta_x}^2}{{\eta_{ref}}^2} \right)$$

Where $Grad_x$ and $Grad_{ref}$ are the gradients from the plot of integrated fluorescence intensity versus absorbance at the excitation wavelength for the sample and the reference, respectively, and η_x and η_{ref} are the refractive indexes of the solvents, water, and ethanol, respectively. Fluorescence measurements were performed using a fluorometer (Perkin Elmer LS55), and absorbance was recorded with a spectrophotometer UV-Vis (Jasco V630-Bio) in quartz cuvettes (5 mm pathlength).

3.5.5. Temperature sensing

The fluorescence spectra of a C3_cys-metal NCs suspension at 10 μM protein concentration were measured at different temperatures ranging from 25°C to 65°C. In addition, the reversibility and the cycle stability of the metal NCs as temperature sensors were tested, repeating the process for 5 cycles in the same sample.

3.5.6. Ion detection

Different ions at 10 μM including Na^+, K^+, Ag^+, Ca^{2+}, Ba^{2+}, Cd^{2+}, Co^{2+}, Pb^{2+}, Zn^{2+}, Ni^{2+}, Mn^{2+}, Mg^{2+}, Fe^{2+}, Fe^{3+}, and Hg^{2+} were incubated with the metal NCs to evaluate the selectivity of the protein-stabilized metal NCs towards them. After 30 min of reaction, 200 μL of the reactant solution was transferred into a quartz cuvette (5 mm pathlength) for fluorescence spectra recording at room temperature.

Copper detection was evaluated by the incubation of protein-stabilized metal NCs in phosphate-buffered solution (10 mM phosphate pH 7.4) with ion solutions at different concentrations (0–10 μM) at 1:1 (v/v). The

fluorescence spectra were recorded under the same experimental conditions.

3.5.7.ROS detection

To detect reactive oxygen species (ROS), the assays were performed using Rose Bengal as the synthesizer for ROS. When irradiated with green light, this dye can produce singlet oxygen molecules. As a control for the presence of ROS 2,2'-azino-bis(3-ethylbenzothiazoline-6-sulphonic acid) (ABTS) was used. ABTS is widely used in antioxidants studies as the reporter for oxidative stress environments [207,208]. In a typical experiment, 90 µl of 10 µM protein stabilized metal NCs in phosphate-buffered solution were mixed with 10 µl of RB at 100 mM. The PL was measured in a quartz cuvette (5 mm pathlength) upon irradiation with a green LED lamp during 15-minute steps for a total time of 60 minutes. In parallel, 25 µl of ABTS were mixed with 10 µl of RB (100 mM) and 65 µl of phosphate-buffered solution as a positive control of ROS detection. Absorbance was measured using a Jasco spectrophotometer (model V630BIO UV-Vis) before and after irradiation with a green LED lamp during 15 min steps for a total time of 60 minutes.

4.ENGINEERED PROTEIN-NANOCLUSTER FOR BIOLOGICAL APPLICATIONS

4.1. State of the art

4.1.1. Fluorescence microscopy for cellular imaging

Fluorescence microscopy is a robust methodology used to reveal the internal structure of cells and the distribution of their components. Among the fluorescence microscopy techniques, confocal laser scanning microscopy (CLSM) allows data reconstruction in 3D using optical sectioning. Moreover, it can be used as a qualitative and quantitative technique[217]. However, a classical burden of conventional fluorescence microscopy is the resolution limit due to light diffraction, defined by Ernst Abbe in the equation[218]:

$$d = \frac{\lambda}{2NA}$$

In which λ is the wavelength of the fluorescence emission of the probe and NA is the numeral aperture of the objective employed. Still, recent advances in super-resolution fluorescence microscopy[219] (with approaches such as STED[220], PALM[221,222], STORM[223], or MINFLUX[224,225]) have been vital to tackling this problem. As such, the application of super-resolution microscopy methods sheds light on a large number of cellular processes. Examples include the distribution, dynamics, and organization of subcellular structures and mechanisms such as membranes and lipid rafts[226], chromosomal DNA in nuclei[227,228], human immunodeficiency virus (HIV) viral infection[229], or molecular traffic within the endoplasmic reticulum (ER)[230,231], microtubules and mitochodria[232,233]. In addition, those techniques have also been used to study the cellular uptake, distribution, and behavior of a number of molecules or nanomaterials (*i.e.,* metal nanoparticles) designed as therapeutic or biotechnological agents.

Spatial analysis of metals in biological samples is important to understand different biological processes (*i.e.*, cellular homeostasis, cellular metabolism, diseases)[213,234], but it is challenging to study bio-metals thoroughly using fluorescence microscopy[235]. The localization and distribution of bio-metals can be partially followed using emissive chelating molecules, which alter their PL emission upon binding to free metal ions[234,236–238]. However, most cellular metals are found bound to biomolecules or stored in safe compartments rather than as free ions[230,234,239]. Equally, it is also vital to study the behavior and fate of nanomaterials used in commercially available products and therapeutic or biotechnological agents once they are internalized by organisms[240,241]. Following the fate and degradation processes of metal-based nanomaterials is complicated using optical methods. Fluorescence can be lost upon release of linked fluorophores or degradation of fluorescent materials, since the endosomal/lysosomal pathway is the uptake pathway followed in most instances[242], meaning that the fate of the non-fluorescent material or free ions generated cannot be followed anymore with fluorescent microscopy.

4.1.2. X-ray fluorescence

Among the different techniques that allow direct detection of metals to track their localization inside tissues and organs (PET, MRI, or LA-ICP-MS), X-ray fluorescence (XRF) is an ideal technique for defining the distribution of biological metals and nanomaterials alike.

XRF is based on the interaction of X-rays with the electrons at the inner shell orbitals of atoms. Each element has its characteristic electronic binding energy in each core energy level (K-edge, L-edge, M-edge). X-rays are sufficiently energetic to excite the internal atomic orbitals of atoms from heavy elements (including most metals), while visible light in fluorescence

microscopy triggers transitions in the molecular orbitals. When one electron is excited and ejected out of an internal orbital, another electron located in an orbital at a higher shell fills the new electronic hole, and the energy excess is released in the form of fluorescence emission, which is unique for each element (Figure 4.1). This unequivocal emission makes XRF a perfect technique to directly detect the elemental components of nanomaterials. Also, as the XRF emission is element-specific, multiplex identification of different elements (*i.e.*, the combined use of probes in the same sample) is feasible. This is interesting for biological contexts, particularly if the elemental probes used are not naturally present in the sample.

Synchrotron-based X-ray fluorescence (SXRF) takes advantage of high brilliance synchrotron radiation produced in dedicated facilities. Current synchrotron facilities provide X-ray beams with high flux (number of photons per second), allowing good sensitivity and detection limits of metals, and possess advanced optical setups that allow beam manipulation to control parameters such as beam size.

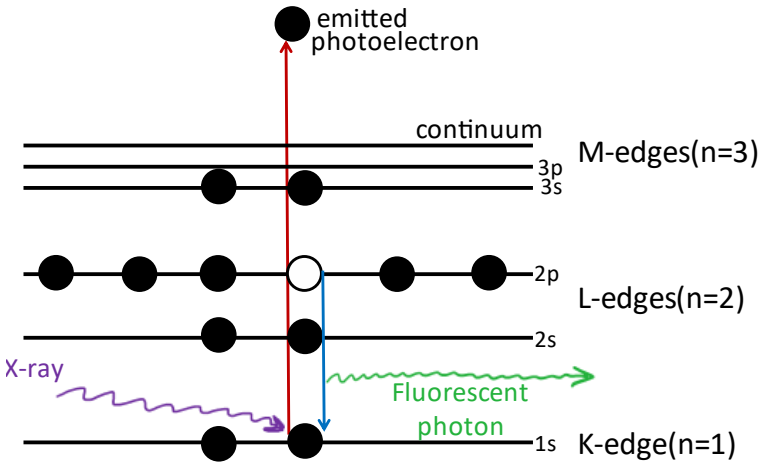

Figure 4.1. X-ray fluorescence mechanism. When an X-ray interacts with an electron from the inner orbitals of the atom, the electron is ejected and

another one fills the electronic hole, emitting fluorescence as an energetic release. The fluorescence emission is characteristic of each element.

4.1.3. X-ray fluorescence microscopy for metal identification in cells.

Synchrotron X-ray fluorescence mapping (SXRF)[243] is ideal for tracking bio-metals and metal-based nanomaterial inside biological samples such as tissues or cells at the micro- (μ-SXRF)[232,233] and nano- (SXRFN)[243] scales. Since the λ of X-rays is much shorter than visible light used in fluorescence microscopy, the resolution limit is mostly imposed by the optics setup available in the beamline used to focus the X-rays[244]. With the proper mirrors, the beam can be focused below the 50x50 nm^2 range[242], which combined with good penetration of X-rays is ideal to assess metal distribution within cells[245]. Still, since the mapping is done by scanning the sample with the beam, the high-resolution *vs.* large field imaging trade-off must be considered, because map scanning at high resolution is slow and time-consuming.

Besides, XRF mapping can be combined with other optical or X-ray based imaging, spectroscopic, or scattering techniques, such as fluorescence microscopy[246], Soft X-ray transmission microscopy[241], ptycography[247], or XAS spectroscopy[234]. The combination of such techniques for imaging offers a valuable multi-approach for in-depth studying of cells, their components, and the bio- or exogenous metals present in them. For instance, correlative SXRF and different X-ray tomographic techniques have produced high-quality 3D elemental maps of algae[235], *Caenorhabditis elegans* nematodes treated with cobalt nanoparticles[248], the precise fate of an anti-cancer metallocomplex in cancer cells[249], and iron functionalized nanoparticles in cervical cancer immortalized cells (HeLa)[250]. In addition, correlative SXRF and fluorescence microscopy have been used to elucidate manganese toxicity in HeLa cells[251], the effects of metals in the

cytoskeleton of dendrites[252], tracking the nuclear delivery of iron oxide-titanium nanoparticles[253], and for organelle identification using dual-labeled antibodies (carrying both gold nanoparticles and commercial dyes)[26].

Still, there is a lack of commercially available, cheap, and robust organelle-specific tags for sub-cellular recognition in SXRF imaging. Therefore, tracking the different organelle structures with precision in SXRFN is challenging, making it difficult to determine the exact subcellular localization of any metal studied. Certain cellular compartments can accumulate specific metals of biological origin in a preferential way, for example, Zn in the nucleus, which can serve for organelle recognition by SXRFN[256]. However, this is not possible for most organelles. Alternatively, antibodies[257,258], DNA[259,260], carbon nanotubes (CNTs)[261], or organometallic complexes[262] have been tested as organelle-specific metal-containing probes. Some of these strategies achieved a good level of success in labeling cellular organelles and proteins. Nevertheless, they also faced several drawbacks. Although antibodies are an excellent option to label sub-cellular targets due to their molecular specificity and variety of options available, they have significant flaws as well, such as the high cost of these reagents and the need for permeabilization and fixation of cells (which can alter the internal content of cells)[263]. CNTs and organometallic complexes face other limitations, including low or non-cell permeability and labeling efficiency, and the need for complicated synthesis to produce them. Other approaches, including protein-encoded lanthanide-binding tags[263] and quantum dots[264], rely on rare elements, which increases their cost. Furthermore, most of these approaches do not allow multiplexing. Therefore, there is a need for new cellular probes capable of labeling efficiently and detecting simultaneously different organelles by SXRFN (or similar techniques). The value of these cellular probes can be increased if they can serve for correlative fluorescence imaging as well.

4.2.Approach

4.2.1.Organelle tags for correlative fluorescence microscopy and SXRFN imaging

Repeat proteins are a versatile engineering platform for multi-purpose nanotechnological tools. CTPR proteins, in particular, can be easily modified to include protein binding domains, peptides, or click chemistry reactive sites, among other functionalities[265], and their modular nature makes them an ideal scaffold for producing different modules with distinctive functionalities. They can also be designed to contain metal binding domains[254,255] and used to synthesize and stabilize small luminescent nanoclusters of different metals, including non-biological (Au, Ag) or trace bio-metals (Ni, Co). These NCs show excellent stability and biocompatibility, and have been used before as imaging probes in fluorescence microscopy[87]. Moreover, engineered NC-CTPRs are promising probe candidates for SXRF, as they can combine specific targeting domains with metal-binding domains within the same molecule (Figure 4.2). We recently demonstrated the potential of those hybrid systems as protein-specific probes for μ-SXRF in tissue samples by targeting successfully Hsp90 proteins in the hearts of fibrotic mice.

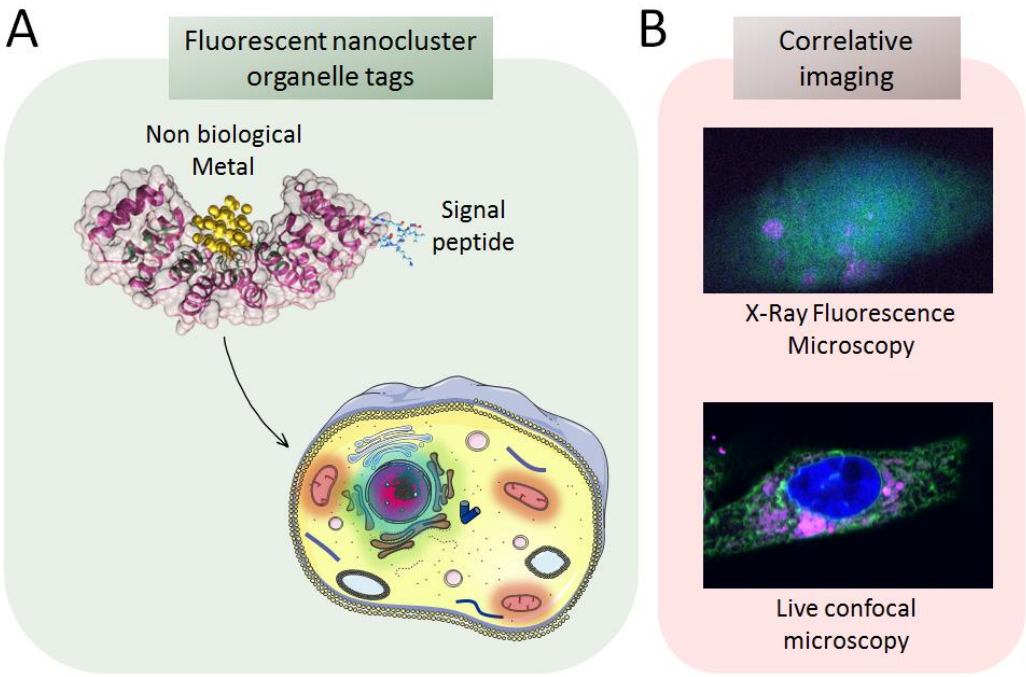

Figure 4.2. CTPR proteins can be engineered as correlative imaging labels. A) A CTPR protein with a fused signal peptide and a fluorescent metal nanocluster can be used as a label for different cellular organelles. B) X-Ray Fluorescence image of an MDA-MB-231 cell treated with AuNCs in which the Au channel is shown in magenta, the K in green (cytoplasm marker), and the Zn in blue (nuclear marker). A live confocal image of another MDA-MB-231 cell treated with AuNCs labeled with RITC (magenta), DAPI (blue), and ER-tracker (green).

This chapter describes a versatile strategy to design modular protein systems that combine organelle-targeting capabilities with distinct optical and X-ray fluorescence emissions (Figure 4.2). Organelle-specific SXRF nanoprobes are produced by introducing naturally occurring signal peptides (*i.e.*, short polypeptide sequences that cells use for protein sorting into the correct organelles) at the terminal sites of CTPR proteins carrying metal-binding modules for the templating of photoluminescent metal NC. Peptides

are chosen over other alternatives (small molecules or DNA aptamers) because they are highly organelle-specific and can be easily encoded in the genetic sequence of CTPR using molecular biology techniques. In addition, this approach allows easily changing the organelle targeted and the elemental composition of the metallic nanoprobe by interchanging the designed organelle tags and the metal salts used to generate the photoluminescent NC. Therefore, changing the NC composition of various NC-CTPRs carrying different signal peptides should be feasible to simultaneously recognize multiple organelle targets, which is not currently possible.

4.3. Results and discussion

4.3.1. Protein design for organelle tags

Signal peptides specific for individual organelles were genetically encoded at the C-terminal of CTPRs with 6 modules (C6). The protein variants and the peptides chosen were:

- NUCLtag: for *nuclear labeling*, the nuclear localization signal (NLS) sequence from SV40[267] was chosen, as it is commonly used for delivering DNA and proteins to cell nuclei[268]. Its amino acid sequence is PKKKRKV. Although Zn is usually used in SXRF cellular maps to identify nuclei, an unequivocal non-biological metal probe for the nucleus is valuable for better identification.
- MITOtag: for *mitochondrial labeling*, the peptide chosen was MLSARSAIKRPIVRGLATV. This peptide is a mitochondrial targeting sequence (MTS) used to translocate proteins into the mitochondrial matrix[259,260]. Mitochondria are interesting organelles to identify due to their role in many metabolic and energy-related physiology. This peptide

was encoded at the N-terminal of the protein, which is the common location of MTS within natural proteins that carry it.

- ERtag: for *endoplasmic reticulum* (ER) *labeling*, which was chosen given its essential role in protein synthesis, modification, and transport. For this purpose, the peptide sequence encoded was KDEL, a signal peptide present in intern proteins of the ER and recognized by a transmembrane protein, the KDEL receptor, for the retrotransport of proteins back to the ER[271,272].

Those proteins also carried 16 cysteines (C6-16cys) as metal coordination residues, forming a metal-binding domain that has already proven efficient in templating NC for *in situ* synthesis[87] and conjugating to naked NC [275–279].

4.3.2. Metal NC synthesis and characterization

Au, Ni, and Co NCs were synthesized *in situ* using an excess of 2 equivalents of metal salt per coordination residue followed by an ascorbate reduction. The NC-protein hybrids were characterized using mass spectroscopy and PL spectroscopy. The MALDI-TOF analysis (Figure 4.3) of the organelle-tag CTPR variants confirms the agreement between experimental and theoretical masses (theoretical masses: C6-16cys 26,025 Da, C6-16cys$_{\text{-NUCLtag}}$ 26,890 Da, C6-16cys$_{\text{-MITOtag}}$ 28,047 Da, C6-16cys$_{\text{-ERtag}}$ 26,510 Da). However, CTPR carrying NCs (NC-CTPR) do not fly as effectively as the protein-only samples, and thus they were difficult to identify by MALDI-TOF mass spectroscopy (Figure 4.3 right).

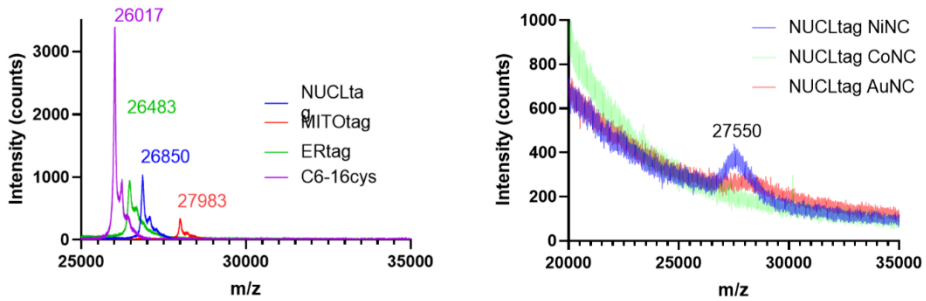

Figure 4.3. MALDI-ToF analysis of CTPR tag variants. Mass spectra of the NC-CTPRs variants (left) and the NC-C6-16cys$_{\text{-NUCLtag}}$ samples bearing NiNCs, CoNCs, and AuNCs (right).

C6-16cys$_{\text{-NUCLtag}}$ was used to grow *in situ* metallic Ni, Co, or Au NCs, and the Protein-NC systems subjected to further PL spectroscopic characterization. All three NC-C6-16cys$_{\text{-NUCLtag}}$ protein hybrids showed similar PL properties, with maximums of excitation at λ_{ex}= 390 nm, and emissions peaking at λ_{ex}= 450 nm and with long tails until 650 nm (Figure 4.4A). The PL emission of all systems was tested under different pH conditions, as it is known that pH can affect the PL properties of NCs. The internalization of our NC protein hybrids by cells occurs through mechanisms that lead them to endosomal compartments,[87] which can eventually evolve into acidic lysosomes. Therefore, understanding the pH-dependence of the PL properties of our NC-protein hybrids could help us to a better interpretation of *in vivo* fluorescence images. As expected, the emission from all NC-CTPRs was pH-dependent. Between pH 7.6 and pH 5, the fluorescent emission of all systems was successfully maintained, but this was significantly decreased at pH 4.4 (Figure 4.4B). Indeed, a precipitated solution was recovered from pH 4.4 samples, which was further

cleaned and stabilized in a pH 7.6 buffer solution, recovering the lost emission (Figure 4.4C).

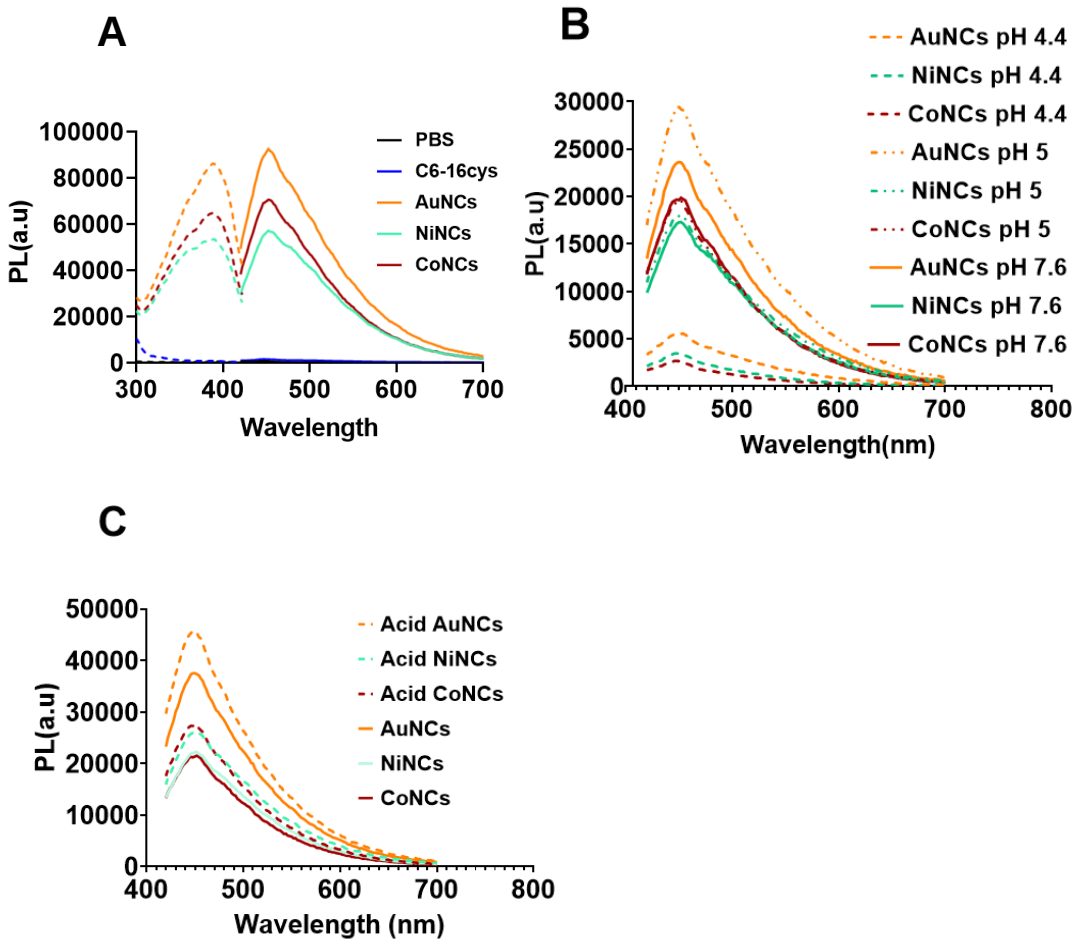

Figure 4.4. Photoluminescent spectra of C6-16cys with different metallic NC grown *in situ*. A) Excitation (λ_{em} 450 nm) and emission (λ_{ex} 390 nm) spectra measured in PBS at pH 8 of C6-16cys (blue), AuNCs-C6-16cys (orange), NiNCs-C6-16cys (cyan) and CoNCs-C6-16cys (red). B) PL emission spectra (λ_{ex} 390 nm) of AuNC-C6-16cys (orange), NiNCs-C6-16cys (cyan) and CoNCs-C6-16cys (red) at pH 7.6 (solid line), pH 5

(dotdashed line), and pH 4.4 (dashed line). C) PL emission spectra of AuNCs-C6-16cys (orange), NiNCs-C6-16cys (cyan) and CoNCs-C6-16cys (red) before acid treatment (solid line) and after the recovery from pH 4.4 to pH 7.6 (dashed line).

4.3.3. Cellular distribution and stability of NC-CTPR by SXRFN and Fluorescence microscopy

The distribution of NC-protein hybrids inside cells was first assessed using SXRFN. MDA-MB-231 cells were seeded onto silicon nitride windows, treated with 40 µM of Au, Ni, or Co untargeted-NC-C6-16cys for 24 hours, mildly fixed with 1% PFA, and air-dried in a desiccator. Samples were then imaged using nano-focused synchrotron radiation at beamline I14 (Diamond light source, UK). This allowed us to follow Au-L-edge, Co-K-edge, and Ni-K-edge fluorescence emissions and obtain elemental maps to visualize the internal distribution and quantify the amount of metal NCs-C6-16cys on fixed MDA-MB-231 breast cancer cells. The XRF maps obtained (Figure 4.5) show differences in the internalization of the three metal NCs. Au was distributed following a vesicular-like pattern in samples treated with AuNCs-C6-16cys. However, when CoNCs were used to treat MDA-MB-231 cells, Co showed a more homogeneous distribution alongside the cell, but some 'hotspots' colocalizing in areas with high concentrations of cellular Zn were also visible. The cellular distribution of Ni was more challenging to analyze due to background Ni emission from the experimental setting, probably from Ni traces in the optics setup. Nevertheless, the Ni signal was enhanced in cells treated with NiNCs, and image processing (energy calibration and fitting correction using the PyMca software[282,283]) allowed to see a homogeneous distribution similar to the one observed for CoNCs treated cells. Finally, samples treated simultaneously with the three types of NCs-C6-16cys showed an equal cellular distribution of Au, Ni, and Co to

those previously observed in cells treated with each of the individual NC-C6-16cys (Figure 4.5).

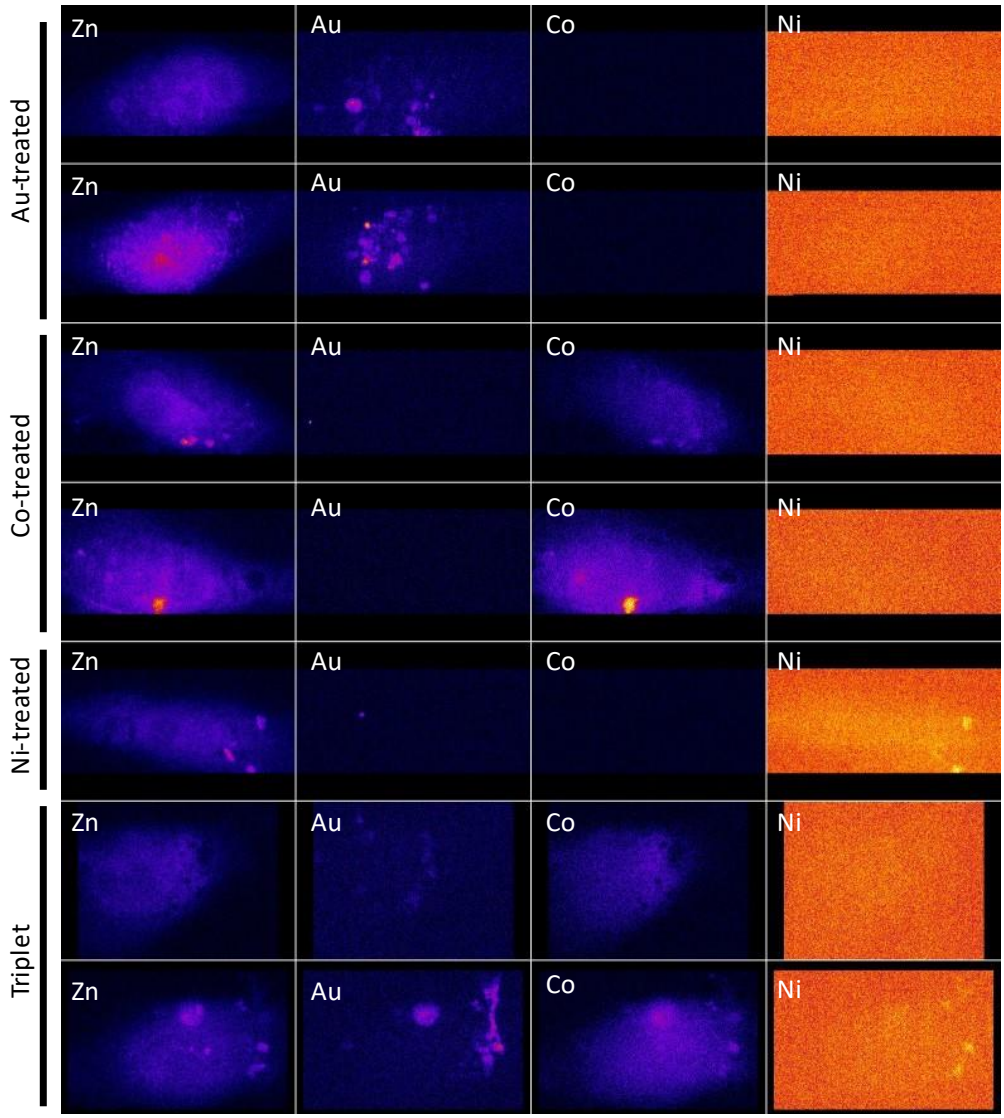

Figure 4.5. SXRFN elemental maps of NC-CTPR treated cells. Metal distribution (Zn, Au, Co, and Ni) of MDA-MB-231 cells treated with 40 μM of AuNC-C6-16cys (Au-treated), CoNC-C6-16cys (Co-treated), NiNCs-C6-16cys (Ni-treated) and 20 μM of each metal NC (triplet).

The XRF data was further analyzed to obtain the metal concentration in each cell area (Figure 4.6A). The XRF maps of K were used to define the cell areas. Quantification of metal amounts was not possible for samples treated with NiNC-C6-16cys (due to the strong nickel background). However, using the PyMca software[284], quantification of Au and Co was possible. Cells treated with AuNC-C6-16cys contained around 0.4±0.3 µM of the metal, while concentrations of Co were in the range of 0.6±0.4 µM in cells treated with CoNC-C6-16cys (Figure 4.6A). Moreover, the amounts of each of the metals inside the vesicular areas observed were found to be higher than in the rest of the cell, ranging from 1.3±0.5 µM in the case of Au to 1.6±0.8 µM in the case of Co (Figure 4.6A). Remarkably, Au and Co were found to colocalize in similar vesicles when cells were treated with all three (Au, Ni, and Co) of the NC-C6-16cys proteins (triplet cells). The concentrations of metals on those cellular structures (0.7±0.4 µM of Au and 0.9±0.5 µM of Co) where only half when compared with vesicles in cells treated independently with the individual NC-C6-16cys. This decrease in concentration was expected due to the lower dose at which those triplet cells were exposed (20 µM). Nevertheless, this data supports our previous observations using live confocal microscopy, in which AuNCs-CTPR are distributed in vesicles around the nucleus.

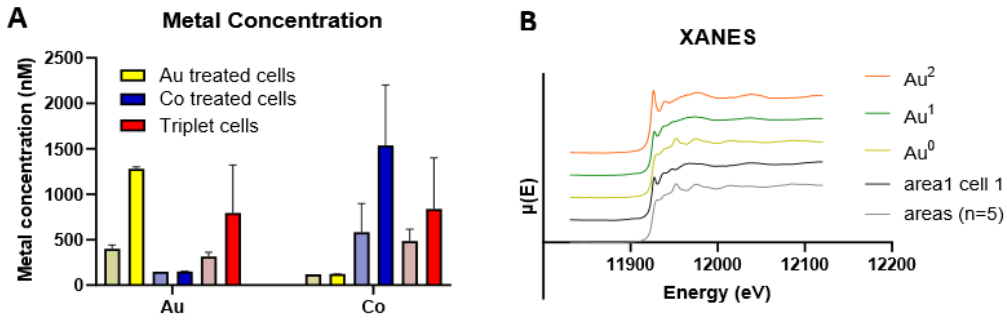

Figure 4.6. Metal concentration and AuNCs oxidation state in NC-CTPR treated cells. A) Average concentration after SD propagation analysis of Au and Co in MDA-MB-231 breast cancer cells treated with

individual doses of Au or CoNC-C6-16cys (40 µM) or a combination of Au, Ni, and CoNC-C6-16cys (20 µM of each). Bars with soft colors show the concentration of the metals found inside the whole cells, whereas bars with bright colors indicate the concentration of the metals found inside vesicles. B) XANES spectra of the three standards used (colored) and different vesicular areas of the Au-treated cells (grey). The total number of areas measured is 6.

Additionally, samples treated with AuNC-C6-16cys were further studied using XAS. XANES maps were collected from areas with high concentrations of Au (*i.e*., vesicular areas) to determine the average oxidation state of the Au and try to assess the stability of the NCs within cells. Previously, XANES spectra were acquired from a gold sheet, and solid samples of AuCl and $AuCl_3$ were used as standards. Remarkably, by comparing the spectra acquired from vesicular areas with the gold standards, it was shown that most Au found within cells was in the form of Au^0 species (except for one specific vesicular area, which contained more significant quantities of Au^I). This result agrees with previous *in vitro* analysis using XPS and suggests that Au NCs stabilized by our TPR proteins are stable inside cells after 24 h treatment (Figure 4.6).

A combination of the data obtained from our measurements demonstrates that Au and CoNC-C6-16cys are good options for further developing metal-labeling tools for cells in SXRF, since µM concentrations of non-biological metals templated by CTPR proteins can be detected inside cells. Still, changes observed in the cellular distribution of the different metals might be due to faster degradation of Ni or Co NCs once their NC-C6-16cys are inside the cells, compared with the more stable AuNC-C6-16cys protein-nanomaterial hybrid. This hypothesis would align with our previous observations showing that CoNC-C6-16cys and particularly NiNC-C6-

16cys seem to be less stable than AuNC-C6-16cys *in vitro*, as they tend to form aggregated nanoparticles that were visible hours after their synthesis. Such stability concerns hinder the use of Co and NiNC-C6-16cys as SXRF tags Therefore, more work is needed to improve the protein stabilization of CoNC and NiNC by NC-C6-16cys.

4.3.4. Fluorescence microscopy

AuNC-C6-16cys were further assessed as organelle probes using confocal laser scanning microscopy (CLSM). They were expected to be internalized in endosomes, since vesicle-like uptake was observed in SXRF and previous studies incubating cells with NC-CTPR hybrids[87]. However, the NC-CTPR hybrids need to be localized in the cytosol to be adequately sorted to each organelle. For these reasons, an endosomal escape agent was used to trigger the release of the different targeted AuNC-C6-16cys into the cytosol. L17E peptide was chosen for this purpose, since it was developed for endosomal escape and cytosolic delivery of proteins[288]. The L17E peptide is an amphiphilic derivative of a cationic membrane-lytic peptide, and its mechanism of action is pH-responsive. The peptide does not interact with the endosomal membranes at physiological pH conditions. However, in an acidic environment such as the interior of a lysosome or a mature endosome, the peptide becomes cationic, triggering the interaction with membrane lipids and inducing membrane lysis. The L17E peptide has been successfully used for the cytosolic delivery of big proteins such as immunoglobulins. In addition, AuNC-C6-16cys$_{\text{-NUCLtag}}$, AuNC-C6-16cys$_{\text{-MITOtag}}$, and AuNC-C6-16cys$_{\text{-ERtag}}$ were labeled with Alexa-fluor-647 for enhanced localization purposes.

Figure 4.7 shows the fluorescence images obtained from HeLa cells treated with 20 µM of AuNC-C6-16cys$_{\text{-NUCLtag}}$, AuNC-C6-16cys$_{\text{-MITOtag}}$, and AuNC-C6-16cys$_{\text{-ERtag}}$ labeled with Alexa Fluor 647 in the presence or absence of

L17E peptide. Confocal microscopy showed that all NC-protein hybrids were internalized into endosome-like vesicles, without identifying any contribution of the L17E peptide in the uptake mechanism. The only observable difference was the presence outside cells of red fluorescence attributed to Alexa-labelled NC-protein hybrids. This could indicate the presence of processes of cell death or aggregation of AuNC-C6-16cys-L17E to the surface of the well. The importance of L17E concentration for the internalization of the NCs-C6-16cys was further studied by incubating HeLa cells with 20 µM of AuNC-C6-16cys$_{\text{-NUCLtag}}$ mixed with increasing concentrations of the L17E peptide: from 20 µM (1x) to 160 µM (8x) (Figure 4.9). Images acquired using confocal microscopy showed differences in the size and morphology of the vesicles in which the AuNC-C6-16cys$_{\text{-NUCLtag}}$ proteins were internalized. There seemed to be a correlation between the decrease in cell integrity and the increase in the size of vesicles carrying the proteins with the increased concentration of L17E used to treat cells. This fact was particularly clear at the highest concentration of L17E used, as several dead cells could be observed.

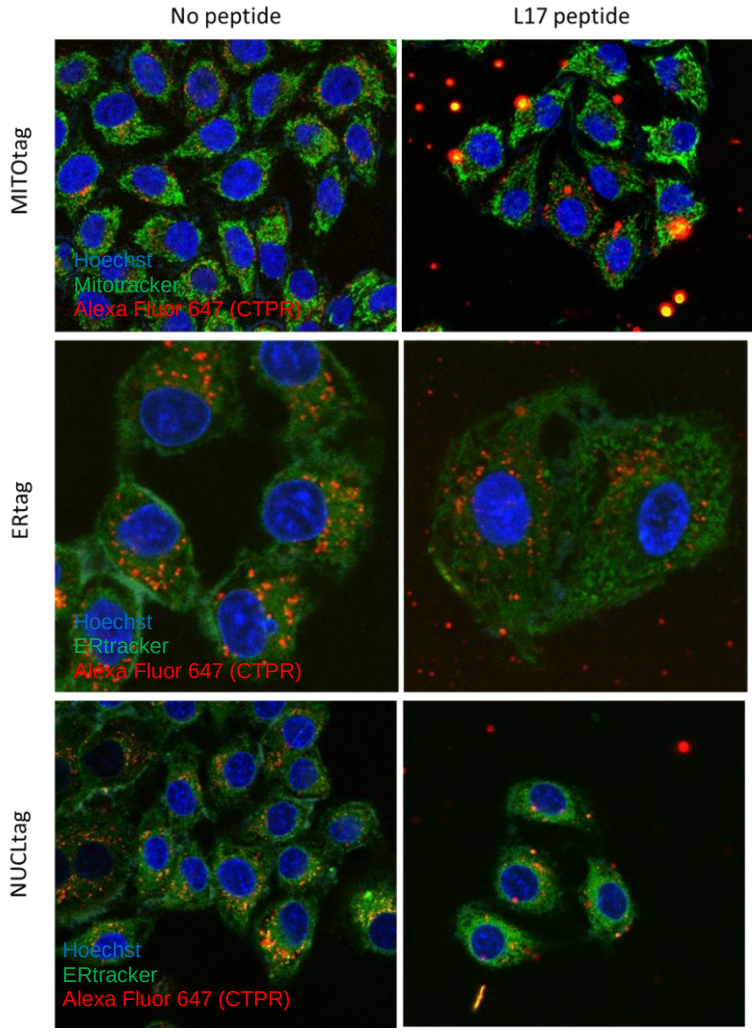

Figure 4.7. CLSM images of HeLa cells treated with AuNCs-CTPR tags. CLSM fluorescence images of HeLa cells incubated with 20 μM of L17E, AuNC-C6-16cys$_{\text{-NUCLtag}}$, AuNC-C6-16cys$_{\text{-MITOtag}}$, and AuNC-C6-16cys$_{\text{-ERtag}}$ labeled with Alexa Fluor 647 (red channel). Cells were stained with Hoechst 33342 for nuclei identification (blue channel), Mitotracker Green (upper panel) and ERtracker Green (middle and lower panels) for organelle identification (green channel).

Other transfection agents such as lipofectamine 2000 or ProteoJuice™ were also used in attempt to improve the efficiency of the lysosomal escape of the tagged proteins. Lipofectamine did not affect the internalization of the protein, as they were still found mostly in the same fluorescent vesicles. Only a limited number of death cells showed localization of the Alexa-labeled AuNC-C6-16cys$_{\text{-NUCLtag}}$, as shown by partial colocalization with the nuclear dye Hoechst 33342. ProteoJuice is a commercially available transfection agent commonly employed to internalize protein in cells. Some preliminary data on HeLa cells incubated with Alexa-labeled AuNC-C6-16cys$_{\text{-MITOtag}}$ showed the Alexa Fluor 647 signal from the protein in a distribution pattern very similar to the one of commercial Mitotracker (Figure 4.10). This suggested the presence of some endosomal escape and later efficient targeting of mitochondria by AuNC-C6-16cys$_{\text{-MITOtag}}$. These preliminary results point towards the importance of using the correct delivery agents for endosomal escape and the utility of organelle-tagged AuNC-C6-16cys proteins for bioimaging.

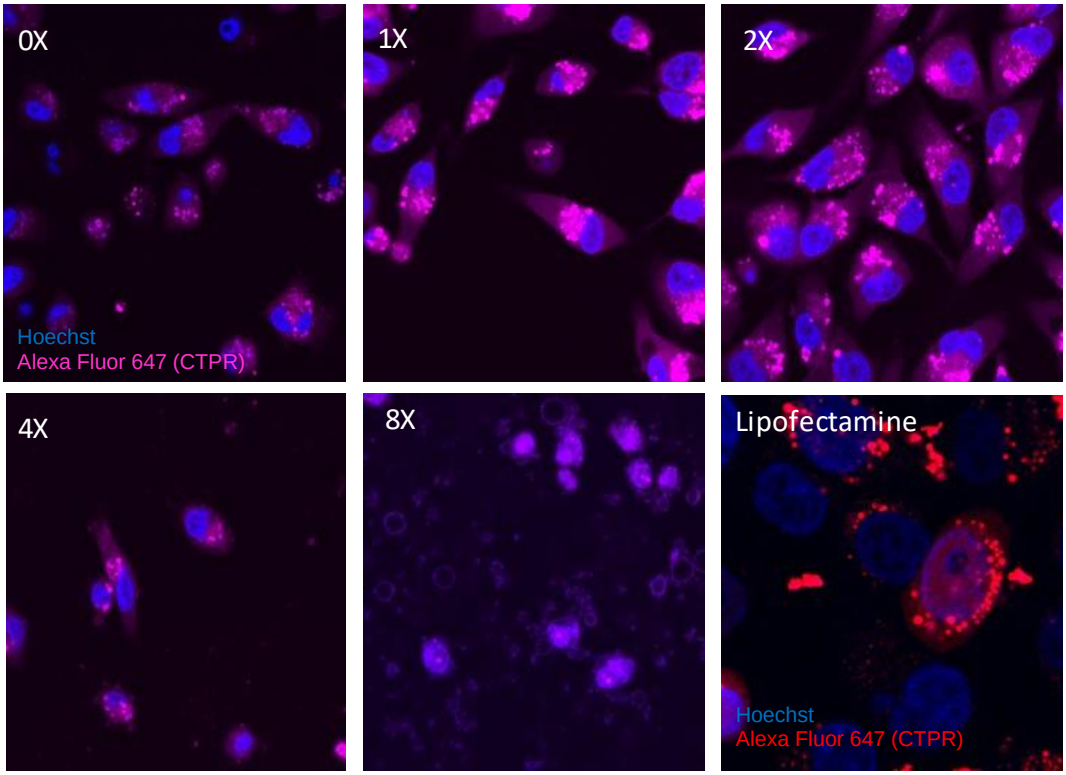

Figure 4.8. Effect of L17E in HeLa cells. CLSM fluorescence images of HeLa cells incubated with 20 μM of AuNC-C6-16cys$_{\text{-NUCLtag}}$ (magenta and red channels) and increasing concentrations of L17E peptide, from 20 μM (1X) to 160 μM (8X). Lipofectamine 2000 was also tested as a delivery agent. Hoechst 33342 dye was used for nuclei staining (blue channel).

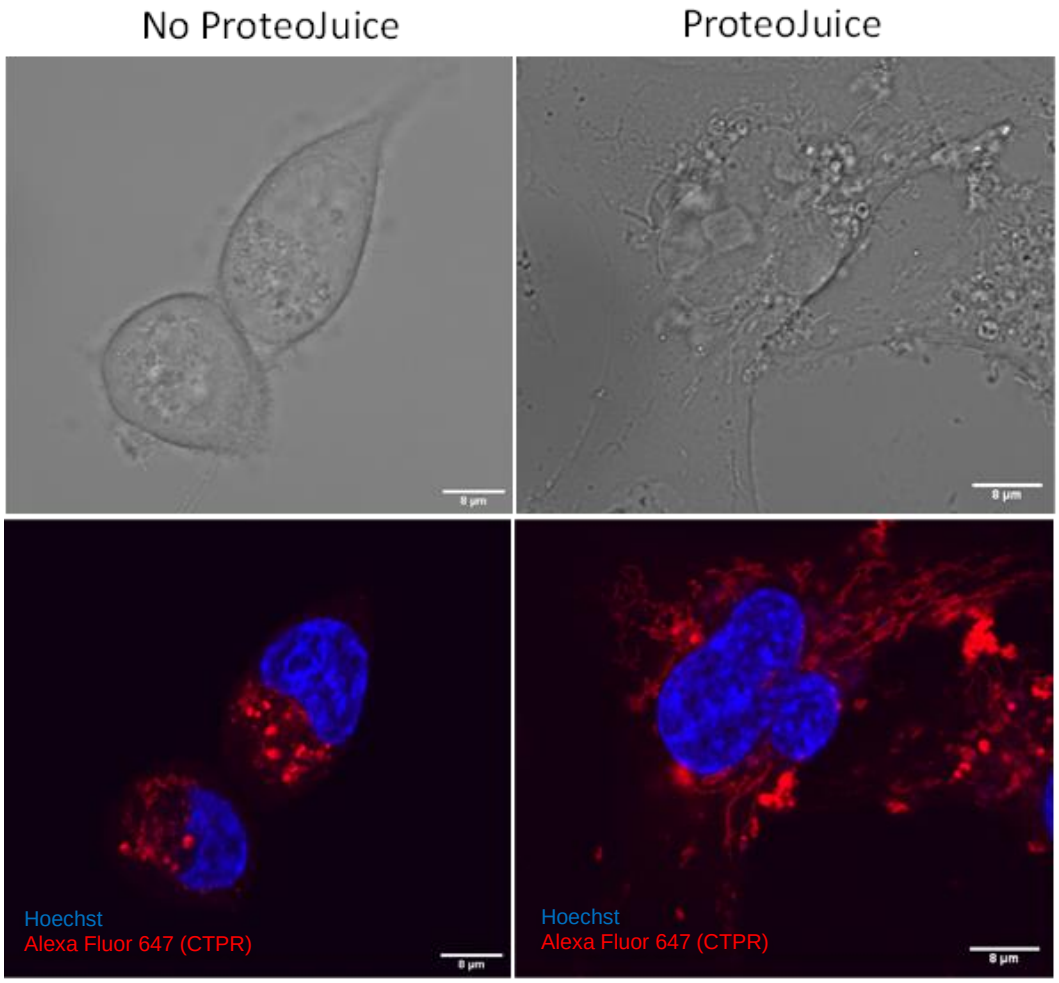

Figure 4.9. Effect of ProteoJuice™ transfection agent in AuNC-C6-16cys-$_{MITOtag}$ treated cells. CLSM brightfield (upper panel) and fluorescence (lower panel) images of Alexa-labelled AuNC-C6-16cys-$_{MITOtag}$ hybrids at 20 μM (red channel) in the absence or presence of ProteoJuice protein transfer agent. Nuclei dyed employing Hoechst 33342 (blue channel).

4.4. Conclusions

CTPR proteins have been proved to be versatile protein systems. Their designability and modularity are excellent features that allow to imagine and test different applications using CTPR as building blocks. CTPR proteins can be adapted to meet different needs for biomedical applications. Taking into account the CTPR scaffold role in nature, metallic nanoclusters can be templated within the protein structure using metal-binding modules. Protein-binding peptidic sequences can be added as well. This dual binding-emissive system can be used for several purposes, in particular for sensing and imaging. We designed CTPR-based systems as photoluminescent metal tags for organelle identification in correlative SXRFN and fluorescence microscopy. The SXRFN data shows that out of the three metallic hybrids tested, AuNC-C6-16cys are the most suitable to be used as nanoprobes due to their increased stability compared with Co and Ni analogs. Moreover, further optimization of the synthesis and cluster stabilization of NiNC-C6-16cys and CoNC-C6-16cys is needed to develop a set of multiplexing metal probes. Besides, AuNC-C6-16cys protein variants encoding different peptide organelle tags were assessed as labeling tools for the nucleus, the mitochondria, and the ER. The work carried out and detailed in this chapter is the first step to developing such labeling tools, although several limitations need to be accounted in the future, such as the need for external agents for cytosolic delivery, the enhancement of NC photoemission for cellular imaging or the need to find more suitable signal peptides.

4.5.Experimental section

4.5.1.CTPR protein design and purification

CTPR proteins were produced following standard molecular biology protocols for recombinant protein expression. First, CTPR variants encoded the signal peptides were constructed by PCR using the set of primers:

Table 4.1. **Primers used for organelle-tag CTPR variants construction.**

Variant name	*Forward primer*	*Reverse primer*
NUCLtag	M13/pUC	5’ TAA TAA AAG CTT TCA CAC TTT ACG TTT TTT TTT CGG ACC CTG TTT CTG TTT AGC 3’
MITOtag	5' GCC ATG GGA TCC ATG CTG TCT GCG CGT TCT GCG ATT AAA CGT CCG ATT GTG CGT GGC CTG GCG ACC GTG GCT GAG GCA TGG TAC AAC CTG 3'	M13/pUC
ERtag	M13/pUC	5’ TAA TAA AAG CTT TCA CAG TTC ATC TTT ACC CTG TTT CTG TTT AGC 3’

Then, the CTPR variants were cloned into a pPro-EX-HTb vector using the restriction enzymes BamHI and HindIII, and transformed in *Escherichia coli* C41 (DE3) cells. Then, the modified bacteria were grown with ampicillin in Luria−Bertani media (LB). IPTG induced the protein expression at OD = 0.6-0.8. After 16 h expression at 20°C, cells were harvested, and the his-tagged proteins were purified via affinity chromatography using Ni-NTA resin. Next, the his-tag was cleaved using TEV protease, and a second Ni-NTA affinity column purification was performed to remove the his-tag and

the TEV protease from the protein sample. Finally, the protein concentration was determined by absorbance at 280 nm using the extinction coefficient calculated from the amino acid composition.

4.5.2. Metal NC synthesis

The protein-stabilized metal NCs were synthesized following a previously reported procedure using sodium ascorbate instead of ascorbic acid to provide a reducing environment[92]. Briefly, 1000 µL of protein at 10 µM were mixed with $HAuCl_4$, $CoSO_4$, or $NiSO_4$ (2 µL 10 mM, 2 eq. related to protein) for at least 30 minutes to allow the adsorption of metal ions to the protein's stabilizing sites. Then, the reduction of the metal ions to metal NCs was achieved by adding 5 µL of sodium ascorbate at 100 mM (10 eq. related to metal ions). The reaction was incubated at 50°C for 24 h. Next, the samples were concentrated to 500µL using Amicon ultrafiltration tubes with a 10-kDa membrane. Finally, the unreacted salts were removed by gel filtration chromatography using an Illustra NAP-25 column. The purified samples were kept at 4°C for further experiments. The absorption and fluorescence spectra of protein stabilized metal NCs were recorded using a Biotek Synergy H1 plate reader.

4.5.3. MALDI-TOF mass spectra

Mass spectra were acquired on an UltrafleXtreme III MALDI ToF-ToF mass spectrometer with delayed extraction (Bruker) equipped with a pulsed N_2 laser (λ= 337 nm). MALDI-ToF sample preparation included 2 µL of the sample mixed with 2 µL of sinapic acid (matrix) in 50:50 water/acetonitrile with 0.01% trifluoroacetic acid (TFA). Then, 1 µL of the mixture was deposited onto the MALDI plate and air-dried.

4.5.4.CTPR Sample preparation for XRF imaging

Carbon framed (5x5 mm) silicon nitride membranes (500 nm thick) were deposited on 6 well plates, where they were washed with water, 70% and 100% ethanol, and let to dry in the air. Then, the membranes were irradiated with UV light for 20 min to sterilize them. A drop of 0.1 mg/ml of polyLys was added to each frame for 20 minutes, and then membranes were washed 3 times with PBS and dried in the air again. MDA-MB-231 breast cancer cell line was purchased from American Type Culture Collections (Manassas, VA, USA). This cell line was grown as a monolayer in Dulbecco's Modified Eagle's Medium (DMEM) supplemented with 10% fetal bovine serum (FBS), 2 mM L-glutamine, 0.25 µg mL^{-1} fungizone, and a mixture of 100 Units of penicillin and 100 µg mL^{-1} streptomycin. All the media, serum, L- glutamine, fungizone, and antibiotics were purchased from GIBCO. Cell lines were maintained at 37°C in an incubator with a humidified atmosphere consisting of 75% air and 5% CO2. A solution of $5x10^5$ cells/ml MDA-MB-231 cells was prepared, and 50 µl of those were placed on the frame and left to attach for 2 hours in DMEM medium. Excess cells were removed, and fresh DMEM medium was added to the well, and then let rest for 24 hours. 500 µL of Au, Co and/or NiNC-C6-16cys dispersed in PBS were diluted in medium containing 10% FBS at the desired concentration. The resulting sample was filtered through a 0.22 µm Millex-GP filter (Merck-Millipore Darmstadt, Germany). Cells were incubated with NC-C6-16cys (40 µM or 20 µM for the triplet cells) for 24h. Then, cell media with the proteins was removed, and cells were washed with phosphate buffered saline (PBS) for complete removal of NC-C6-16cys from cell medium. After the CTPR protein treatment, the cells were washed twice with Tris-glucose buffer and dipped for 2 s in sterile water. Then the cells were fixed using 1% paraformaldehyde (PFA) for 5 min at room

temperature, blotted using filter paper to remove any excess liquid, and dried in a desiccator.

4.5.5.XRF imaging

Silicon nitride membranes were visualized in both reflective and transmission mode using a Zeiss Axio Image M2m visible microscopy at the I14 beamline (Diamond Light Source UK) to select cells for XRF analysis. XRF maps and XANES spectra were acquired at room temperature using the four elements silicon drift diode detector available at I14. Beam energy was set at 12 keV and focused at 50 x 50 nm^2. First, coarse XRF scans were acquired to confirm the exact position of cells (300 nm step size, 200 ms dwell time). Then, fine cellular mapping was used to obtain the elemental composition of selected cells (100 nm step size, 200 ms dwell time). Moreover, we acquired XANES maps in regions of interest (between 1.5x1.5 μm^2 and 3x3 μm^2 in size) of cells treated with AuNC-C6-16cys. Solid Au sheet, AuCl, and $AuCl_3$ were measured as XANES standards. The maps were collected using a small number of key energies (*i.e.,* 11862.5, 11926.5, 11951.6, 11952.5, and 11975.6 eV; 100x100 nm^2 step size, 200 ms dwell time), which allowed to simulate the Au XANES spectra of each point analyzed, and assess the oxidation state of Au. The energies used for these maps were previously chosen by comparison of the standards acquired. This method has been recently developed by beamline scientists at I14 and allowed us to collect XANES maps in a short time, removing all traces of beam damage.

4.5.6.CLSM imaging

Tagged AuNC-C6-16cys were labeled using Alexa Fluor 647 protein label kit (ThermoFisher). HeLa cells were cultured on a µ-Slide 8-well plate at a density of $1x10^4$ cells per well in 250 µL of complete medium. After 24 h, the growth medium was removed, and cells were then incubated 16h at

37°C in the presence of the AuNC-C6-16cys (20 µM) and L17E peptide (20 µM). Then, the cells were incubated 5 min with PFA 1%, washed 3 times with PBS, incubated 20 min with Hoechst 33342 (ThermoFisher) for nuclear staining, Mitotracker Green™ and ERtracker Green™ (ThermoFisher) for organelle staining, washed three times with PBS to remove free unbound protein stabilized metal NCs and finally 250 µL of PBS was added to each well. Cellular uptake of the nanoclusters was detected using a Confocal Fluorescence Microscope (LSM 510 Meta, Zeiss). Excitation wavelengths of 405 nm to image the Hoechst dyed nuclei, 515 nm to image the Mitotracker Green™ and ERtracker Green™ and of 633 nm to image the Alexa dyed NC-protein hybrids were used for all the confocal fluorescent microscopy experiments.

5.CONDUCTIVE BIOMATERIALS: USING PROTEINS TO ORGANIZE METALLIC NANOPARTICLES

5.1. State of the art

5.1.1. Conductivity and charge transfer in living organisms

The discovery of the electric conductivity in animal tissues by Luigi Galvani in the 1770s powered the exploration of electrical phenomena within living beings, termed bioelectricity[290]. Tissue scale bioelectrical phenomena has been observed in excitable animal tissues such as the cardiac muscle tissue[291] or the nervous tissue[292]. In both systems, the electrical excitation is generated by a rapid and transient charge exchange across both sides of cellular membranes within the tissue, moving as a wave alongside the membrane (a mechanism termed action potential) and triggering action potentials in adjacent cells. This behavior translates in synchronized electrical excitation at tissue level. Nonetheless, bioelectricity also regulates and synchronizes cell behavior *in vivo*[293,294], especially in cell proliferation processes such as wound healing[295–298] embryogenesis (early development of organisms)[294,297] and cancer[299–301]. Moreover, bioelectricity on cell populations and tissues is not exclusive to animals since it has also been observed in physiologic processes of plants[289,299,302–304], bacteria[305–307], and archaea[282,283].

The basis of such electrical processes in living organisms relies on the movement of charged ions (such as H^+, Ca^{2+}, Na^+, K^+), which occur and are maintained by the formation of ionic gradients alongside different cellular or subcellular compartments. For example, the bioenergetic machinery of cells uses electrochemical gradients of H^+ in mitochondrial compartments as reservoirs for energy conversion, in which conductivity plays a significant role. Conductivity is a physical phenomenon consisting of the movement of charged particles, such as electrons (electroconductivity) and protons (protonic conductivity) throughout materials or molecules. In cellular

respiration and many other bioenergetic processes, protonic and electronic conductivity events can be commonly coupled. For instance, at the cellular level, protonic movement is a ubiquitous mechanism in energy-related processes, as transmembrane protein proton pumps generate electric fields across membranes (*i.e.*, membrane potentials). This occurs in mitochondrial cell respiration, where a proton gradient generated between the intermembrane space and the mitochondrial matrix is used for driving the phosphorylation of adenosine diphosphate (ADP) into adenosine triphosphate (ATP) by the protein ATP synthase[308]. Proton charge transfer (PT) and proton-coupled electron transfer (PCET) also have a meaningful role in living systems[305], for example, it occurs between enzymes and enzymatic cofactors (such as the coenzymes nicotinamide adenine dinucleotide, NAD, or flavin adenine dinucleotide, FAD) in which the coenzyme is reduced.

The underlying molecular process in electroconductivity of biological origin is electron transfer (ET), which occurs in the electron transport chain, among others. This is an array of bacterial, mitochondrial or chloroplast transmembrane protein complexes that transfer electrons from donors to acceptors *via* redox centers, and helps to maintain the proton gradient responsible for the cellular respiration. Two intermolecular and long distance ET mechanisms in molecules are commonly proposed: electron hopping[309–314] and quantum tunneling[299,308,315,316]. As a general approach, in electron hopping the electric current is produced by the movement of electrons from the excited states of atomic donors to electronic holes in atomic acceptors, following a path alongside a lattice — for example, an array of redox molecules. Instead, in quantum tunneling the ET occurs when the electron passes through an energetic barrier with a defined thickness, typically below 4 nm[315,316], *i.e.* a tunnel junction[317,318]. Such transfer is a forbidden phenomenon by classical mechanics, but the

probability of a tunneling event decrease exponentially with the thickness increase of the barrier. The distance range, the energetic barrier between the donor and the acceptor, the chemical environment and thermal fluctuations can affect which mechanism dominates the ET[319].

Nowadays, the molecular control of conductivity from biological origin takes importance as a possible solution for designing devices and materials for current problems, such as neurological regenerative medicine or sustainable energy harvesting. Remarkably, several types of biomolecules have been shown to participate in charge transport processes. Those include DNA[320] and proteins[321–323], which seem to be dominated by the hopping transport regime, at least at long-range distances and biological temperature ranges[324]. Thus, proteins can be envisioned as promising sources of conductive molecules for the design of bioelectronic tools.

5.1.2. Protein conductivity

Most proteins are usually considered insulators, although electronic and protonic conductivity has been recently shown in some types of proteins. Long-range electronic conductivity in protein-based materials arises from two mechanisms: redox-mediated via hopping electron transfer across redox centers, which are spaced closely enough for coherent overlap to occur[110], or non-redox-mediated conduction with a bandgap that depends, among other parameters, on the protein amino acid composition and the secondary structure of the protein scaffolds[113]. Protonic conductivity occurs when protons are transported along the protein scaffold using charged amino acids, such as aspartic and glutamic acids[112]. In addition, special charge transport occurs between redox-active amino acids, such as tyrosine or tryptophan, where the charge transport happens by proton-coupled electron transfer simultaneously showing electronic and protonic

transport (PCET) [325]. These different types of transport can interplay depending on the composition of the polypeptide chain[326].

Protein conductivity opens the door to develop new biocompatible conductive materials. Proteins are promising building blocks due to their versatility, designability and biocompatibility. Still, while there are emerging efforts in this area, there is an open challenge related to the limited conductivity of protein-based systems. The control of the charge transport mechanism in protein-based materials would allow tuning their conductive properties, necessary to generate bio-based conductive materials and devices. Several strategies have been reported to boost electronic or protonic charge transport in protein-based systems. For example, protonic charge transport in reflecting protein films has been tuned by varying the composition of the charged amino acids[327]. The electronic transport has been favored by introducing redox-active amino acids, such as tryptophan or tyrosine, or redox-active compounds, such as naphthalene diimide (NDI), alongside the protein scaffold[309–314]. However, despite the increasing knowledge on transport mechanisms, charge transport through long distances is difficult to control and tune as it depends on the structure of the protein-film and its chemical composition.[90,138]. The conjugation of conductive nanomaterials, such as metallic nanoparticles, with protein-based systems can be a useful choice for enhancing protein conductivity.

5.1.3. Nanomaterials for conductivity

Both charge transport mechanisms, ET and PT, can be used in synergistic devices using, on one hand, biomolecule scaffolds that already present some conductivity, and, on the other hand, different synthetic nanomaterials to enhance such conductivity. The miniaturization of electronics and their molecular coupling with biologic systems is a field in expansion[90,323]. In this sense, the use of synthetic molecules as dopants integrated in biomolecular

devices is being explored for developing new devices. For instance, graphene, a carbon allotrope with exceptional electroconductive properties, has been used for developing graphene-cellulose composites endowing conductive properties to cellulose-based supports and matrices[90,329], peptide-graphene nanowires[319] and graphene-protein thin supercapacitators[330,331] for miniaturized bioelectronics. Other common approach is the conjugation of conductive polymers[123,332,333], such as PEDOT, which has been used with polysaccharides and carbon nanotubes as a support matrix for neural cells[334]. These examples prove the potential that hybrid biomaterials have in electronics for applications in energy management, novel electronic devices and regenerative medicine.

Metallic nanomaterials deserve a special mention, since metals are the most used elements for crafting electroconductive devices due to their high conductivity. Several biological systems have been employed to template metallic nanomaterials for conductive purposes, such as nanowires based on Au and Ag salt deposition onto amyloid fibers[335], Pd and Pt salts deposited onto filamentous proteins from a hyperthermophile microorganism[139], or Ni and Co nanowires templated by the tobacco mosaic virus (TMV) capsid's central channel[203]. Apart from metal salts, metallic nanostructures such as gold nanoparticles have been used for the decoration of DNA[336], chitosan gels[329] and decellularized matrix[93] for cardiac tissue scaffolding, or conductive silk fibers[337]. Protein-based hybrid structures can also be generated with the specific arrangement of functionalized nanomaterials (gold nanoclusters, nanoparticles) along the protein backbone[92,93,309,329–331]. These approaches have resulted effective in enhancing conductivity to biomolecular-based materials.

5.2.Approach

The current chapter describes a novel approach that combines protein design, biomolecular templating of gold nanoparticles (AuNPs), and protein self-assembly to enhance the conductive properties of protein-based films (Figure 5.1). CTPR proteins are an ideal starting point scaffold for designing conductive biomaterials for the following reasons:

- The consensus tetratricopeptide repeat protein (CTPR) used as a protein scaffold comprises a 34 amino acid helix-turn-helix module[331]. The folding of CTPRs is defined by a few conserved residues; hence, there is much room for engineering new protein-based devices by introducing changes in non-conserved residue positions in the polypeptide sequence[338,339].
- CTPRs assemble, forming transparent ordered solid films through their intrinsic self-assembly properties of the structured units[90,332], by drop casting and drying a concentrated solution of protein. As previously demonstrated, these self-assembly capabilities enable photoconductive and electroactive functional assemblies based on CTPRs[341]. CTPR protein-based films have shown protonic transport due to their ionic nature and high content of charged amino acids, and as such, they have been proven to be attractive actuators that generate and discharge electric potential as a response to humidity in the environment[333,334]. The intermolecular order CTPRs adopt in films and the rigidity of the monomeric CTPR unit could be advantageous for charge transport alongside the protein film.
- In parallel works, the incorporation of AuNPs for electrical interfacing of redox enzymes or the AuNP-assisted assembly of a heme protein (cytochrome c, which contains an heme group that act as a redox center) resulted in effective improvement of the long-range charge

transfer efficiency[123,335,336] that naturally occurs between redox groups. AuNPs have also been used to generate AuNPs-peptide conductive nanocomposites[337]. The previous works showed the value of design strategies to improve conductivity in protein-based systems and inspired the use of AuNPs as electron conductive elements in a CTPR-based macroscopic hybrid films.

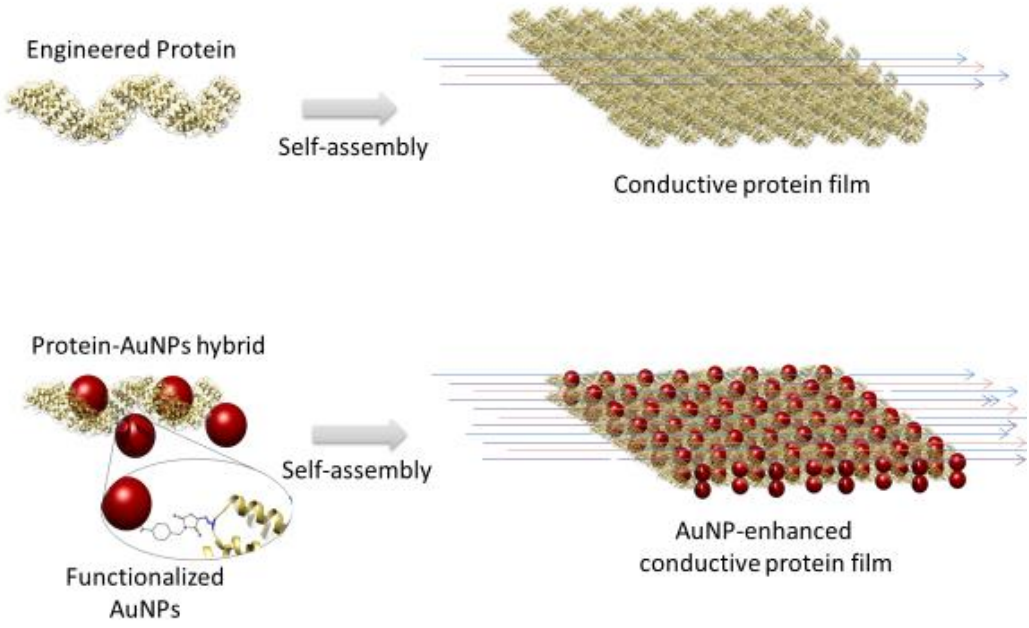

Figure 5.1. Conductive protein-based biomaterials. Top) Engineered repeat proteins as building blocks to fabricate self-assembled conductive films. Bottom) Protein-AuNPs hybrids as building blocks to fabricate AuNPs-doped self-assembled films with enhanced conductivity.

This constitutes a novel approach to tune the charge transport properties of protein-based materials by using electron-dense AuNPs. Two strategies are combined in a unique way to generate the conductive solid films: first, the controlled self-assembly of a protein building block, and second, the

templating of AuNPs by the engineered building block. This bottom-up approach allows controlling the structure of the films and the distribution of the AuNPs within, leading to enhanced conductivity.

Herein, a CTPR unit was first designed to template AuNPs in unique positions with nanometer precision through an orthogonal conjugation strategy. Then, protein self-assembly after solvent evaporation guided the formation of both solid films of CTPRs and CTPR-AuNPs. Remarkably, the CTPR films already displayed conductivity in the hundred nS/m range, recordable at micrometer length scales and mainly attributed to protonic charge transport. The CTPR-AuNPs hybrid films showed an enhancement of four orders of magnitude in conductivity compared to the CTPR-only films and, presumably, different charge transport properties. The current results demonstrate a strategy to fabricate protein-based conductive films with enhanced conductivity by using highly conductive nano-elements, which paves the way for the future application of hybrid protein-based systems in the field of bioelectronics.

5.3. Results and discussion

5.3.1. Protein design for nanoparticle templating

CTPR proteins were identified as good candidates to generate protein-based conductive films due to their ability to form ordered macroscopic materials through their self-assembly properties. CTPR16, a protein composed of sixteen CTPR repeats, was chosen as a scaffold considering its high stability and 16 nm length, making it suitable for templating several nanoparticles per protein. Moreover, as demonstrated for squid ring teeth proteins, the number of tandem repetitions significantly and systematically enhances bulk transport properties[338]. Therefore, sixteen CTPR repeats appeared as an appropriate protein size for promoting conductivity. To

ensure a homogeneous and controlled distribution of AuNPs over the CTPR film, AuNPs were introduced precisely on selected CTPR scaffold regions by covalent linkage. CTPR16 protein was engineered with 4 unique cysteine residues in the loop of the 2nd, 6th, 10th, and 14th repeats, by the mutation R33C. This position is integrated in the final loops of the repeats, and the repeats were chosen in order to have the AuNPs faced in opposite directions (Figure 5.2). This mutation allows the selective conjugation of the AuNPs, leading to CTPR16$_{4Cys}$ (Figure 5.2D). As there are no other cysteine residues in the protein, the AuNPs would be attached specifically on these positions. Position 33 within the CTPR sequence was selected since it is a non-conserved position[329] and, therefore, a non-structural position, besides being located in a solvent-exposed loop that will facilitate the conjugation. Repeats 2nd, 6th, 10th and 14th were selected to encode a CTPR-AuNP complex with optimal inter-particle distance with 2 nanoparticles per superhelical turn[203], and alternate particles facing opposite sides of the superhelix (Figures 5.2 and 5.3B). These mutations did not significantly affect the structure or scaffold stability, as confirmed by circular dichroism (CD) (Figure 5.3D).

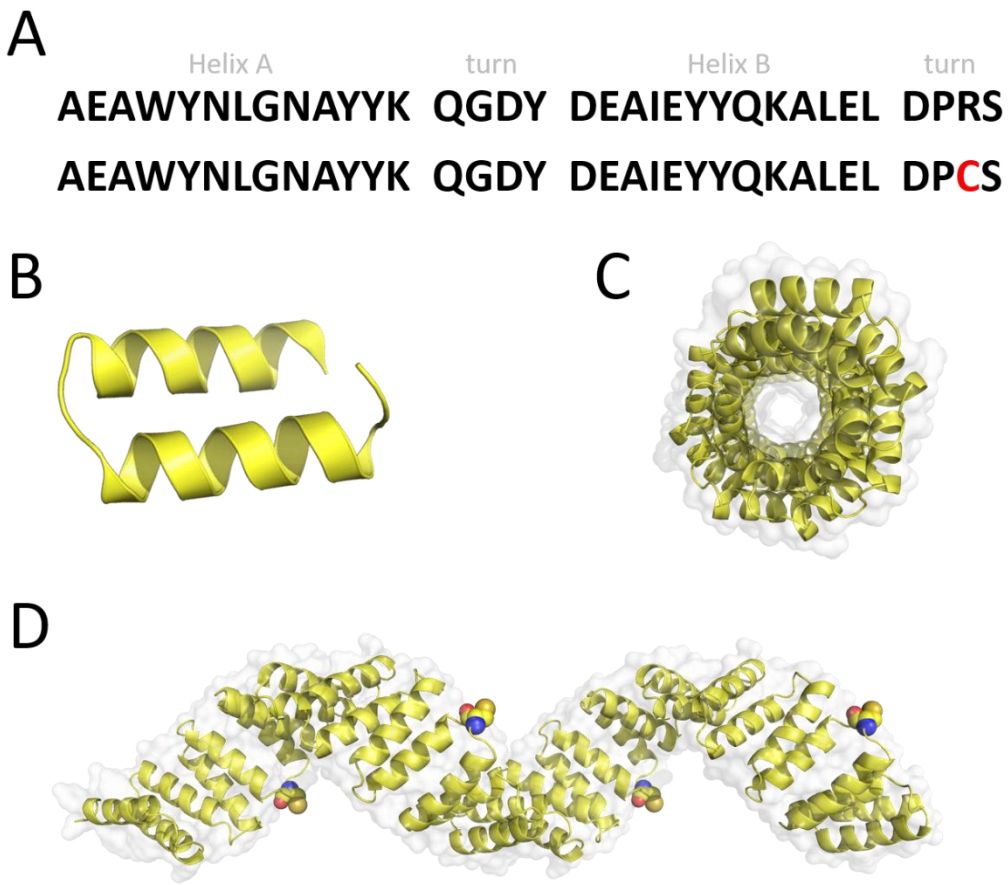

Figure 5.2. Sequence and structure of CTPR16$_{4cys}$. (A) Sequences of the wild type CTPR consensus (top) and of the mutated CTPR including the cysteine residue used for repeats number 2, 6, 10 and 14 (down). (B) Ribbon representation of one CTPR repeat. (C) and (D) Ribbon representation of CTPR16$_{4Cys}$ with its mutated cysteine residues highlighted as colored spheres.

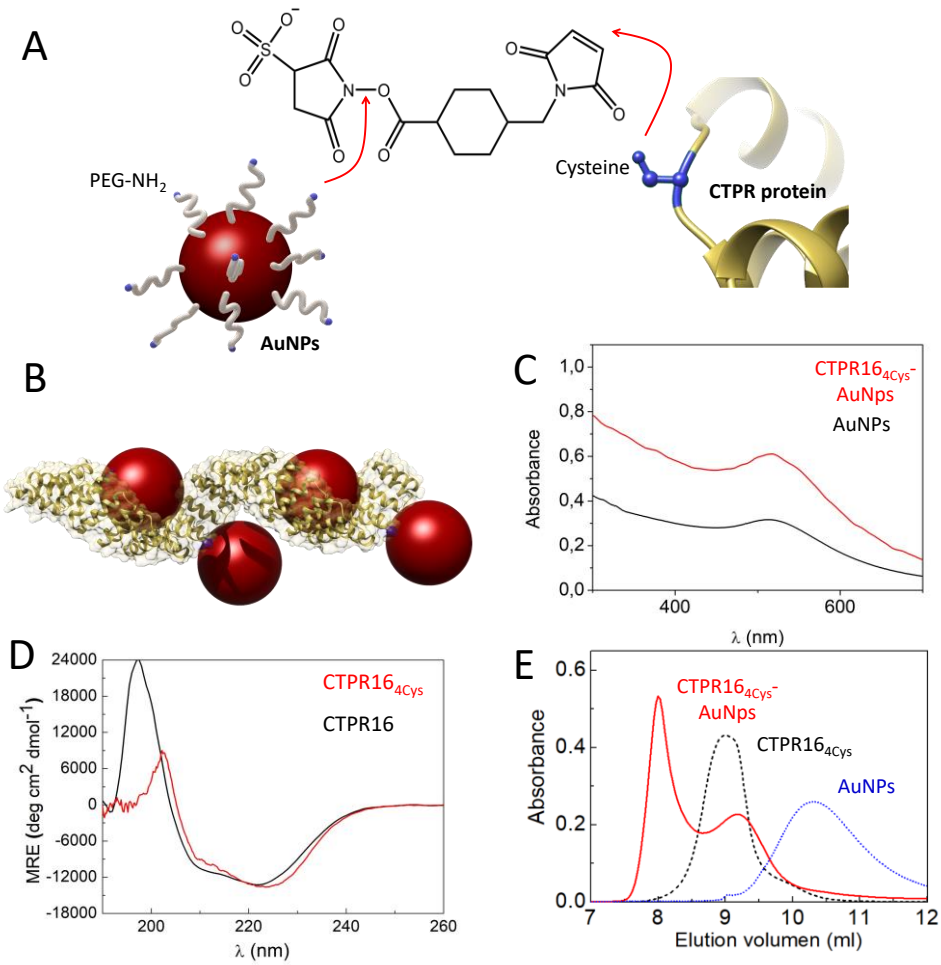

Figure 5.3. AuNPs conjugation to CTPR. A) Schematic representation of the conjugation strategy followed. The free amines from the PEGylated AuNPs and the thiol groups from the cysteines (shown in blue) of the CTPR16$_{4Cys}$ protein are linked using sulfo-SMCC molecules. B) Ribbon representation of the CTPR16$_{4Cys}$-AuNPs conjugated protein. Structural model is based on the structure of PDB ID: 2HYZ. The mutated cysteine residues are highlighted in blue. C) UV-Visible spectra of the AuNPs with their characteristic LSPR peak at 520 nm (black line) and the CTPR16$_{4cys}$-AuNPs conjugate (red line). D) CD spectra of CTPR16$_{4Cys}$ (red line) compared with the original CTPR16 (black line). E) Size exclusion

chromatograms of AuNPs (blue dotted line), the CTPR16$_{4cys}$ protein (black dotted line) and the CTPR16$_{4cys}$-AuNPs conjugates (red line).

5.3.2. Nanoparticle synthesis, conjugation and characterization

Newly synthesized AuNPs 3.1 ± 0.7 nm in diameter coated with amine-polyethylene glycol (Amine-PEG; to maintain their colloidal stability) showing a localized surface plasmon resonance (LSPR) around 510 nm were conjugated to CTPR16$_{4Cys}$ proteins using sulfo-SMCC conjugation chemistry. As shown in Figure 5.3A, the NHS ester group of the sulfo-SMCC linker reacts with amine groups of the amine-PEG AuNPs, while its maleimide group reacts orthogonally with cysteines in the protein scaffold. After conjugation, the CTPR16$_{4Cys}$-AuNPs complexes were purified from unbound AuNPs by affinity chromatography. The eluate that exhibited a pink/purple color, characteristic of the AuNPs, was analyzed by size exclusion chromatography (Figure 5.3E). The elution time of CTPR16$_{4Cys}$-AuNPs was the shortest compared to free CTPR16$_{4cys}$ and free AuNPs, due to their larger hydrodynamic radius. Moreover, the UV-visible absorption spectrum of the CTPR16$_{4Cys}$-AuNPs conjugates showed the AuNPs LSPR peak at 510 nm (Figure 5.3C), which confirmed AuNPs incorporation into the CTPR16$_{4Cys}$.

The conjugation efficiency was analyzed by transmission electron microscopy (TEM) (Figure 5.4A). TEM images acquired for determining the distribution of the AuNPs showed the presence of spatially limited assemblies made of 3 or 4 particles, with a disposition in agreement with the arrangement encoded by the engineered CTPR16$_{4Cys}$ scaffold (Figure 5,4A, left panel). Such assembled nanostructures were not observed in the original amine-PEG functionalized AuNPs, for which primarily large aggregates of particles are observed (Figure 5.4A, right panel). The CTPR16$_{4Cys}$-AuNPs conjugates also revealed some larger assemblies

composed of more than 4 AuNPs per group, which could be due to the linkage of two or more proteins through the AuNPs, as the activated AuNP-SMCC intermediates are not monovalent and could potentially be grafted by two or more proteins. However, the conjugates assemblies and the control particle before conjugation show a different behavior, with a predominance of 1–4 assemblies in the conjugates, whereas a predominance of large nonspecific aggregates was found in the control sample (Figure 5.5).

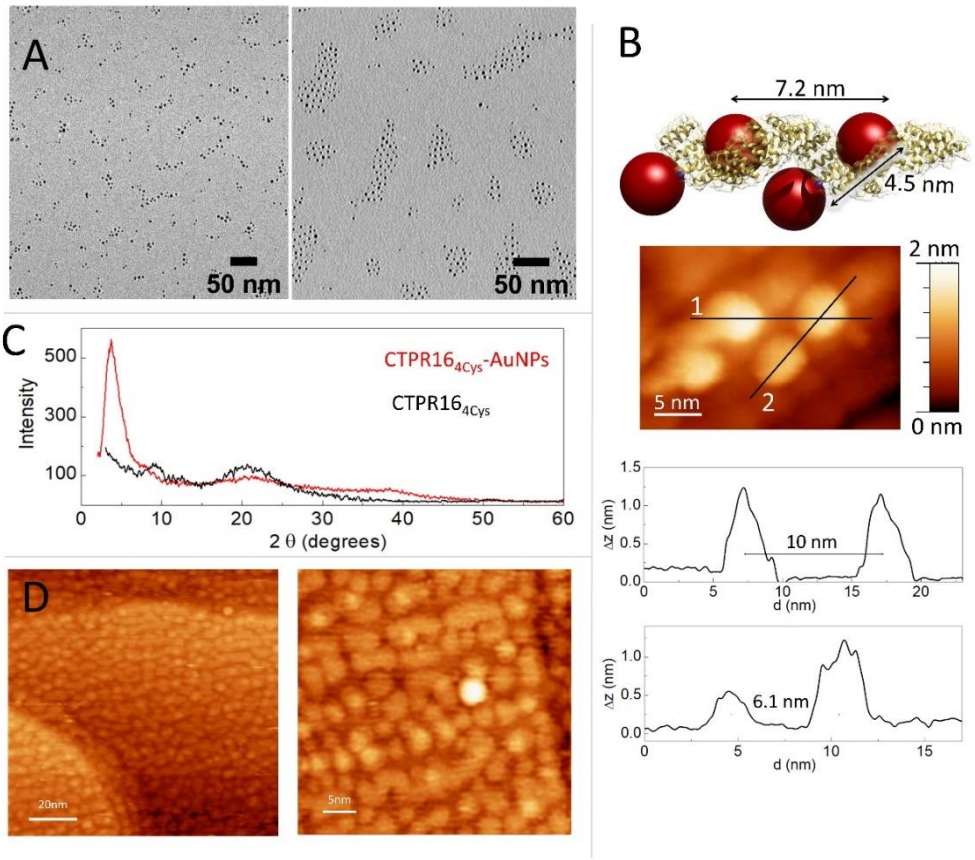

Figure 5.4. AuNPs arrangement within CTPR proteins. A) Left: TEM micrograph of CTPR16$_{4Cys}$-AuNPs conjugates in discrete groups. Right:

TEM micrograph of the PEGylated AuNPs in aggregates. B) Model structure of CTPR16$_{4Cys}$-AuNPs conjugate based on the crystal structure of CTPR20 and the location of the cysteine mutations in the CTPR protein. A STM image of one CTPR16$_{4Cys}$-AuNPs conjugate is shown with the profile plots of lines 1 and 2 shown below. C) Powder X-ray Diffraction (P-XRD) spectra of CTPR16$_{4Cys}$-AuNPs conjugate film in red and P-XRD spectra of the CTPR16 film in black. D) STM images of the CTPR16$_{4cys}$-AuNPs conjugates deposited on a gold surface at different magnifications.

The CTPR16$_{4Cys}$-AuNPs nanoscale structure was explored using scanning tunneling microscopy (STM) at bias voltages between 0.1 V and 1.5 V at room temperature (Figure 5.4B). Conjugated CTPR16$_{4Cys}$-AuNPs at 1 nM were deposited by drop-casting over a freshly flame-annealed gold surface. Groups of four AuNPs allocated in good agreement with the disposition of the four cysteine residues in the designed protein were observed. According to image profiles, the distances between gold nanoparticles are slightly larger than expected from the model based on the CTPR crystal structure, which can be explained by the flexibility of the CTPR spring-like backbone[339]. Moreover, since STM images are based on the current measured between the tip and the sample, the obtained STM images already confirm the conductivity of the AuNPs attached to the scaffold protein.

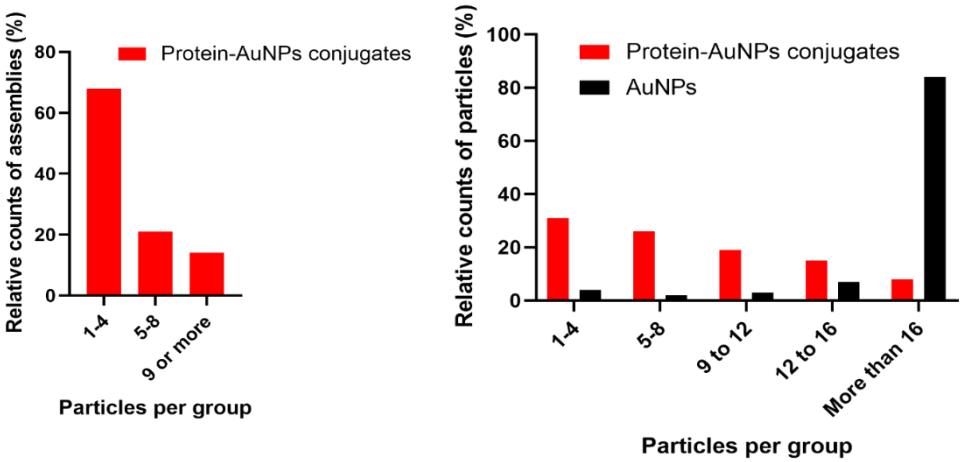

Figure 5.5. AuNPs analysis on TEM micrographs. Left) relative counts of assemblies divided by classes (1 to 4, 5 to 8 and 9 and more particles per group). Right) relative count of particles divided by classes (1 to 4, 5 to 8 and 9 and more particles per group).

5.3.3. Film formation and conduction measurements

CTPR16$_{4Cys}$ and CTPR16$_{4Cys}$-AuNPs solid-state assemblies were generated using CTPR protein intrinsic head-to-tail and side-to-side interactions[332]. A 300 µM protein solution was deposited into a planar surface, and a transparent solid film was formed after drop drying. X-ray diffraction (XRD) was used to check the internal order in the films (Figure 5.4C). The XRD spectrum of the CTPR16$_{4Cys}$ film showed two peaks at 2θ = 9.6° (001) and 20.0° (002), which could correspond to a lamellar packing of the protein with a periodical d-spacing of 9.1 Å, in agreement with previously described CTPR protein films[93]. CTPR16$_{4Cys}$-AuNPs films also showed a peak at 2θ = 20.1°, related to the protein packing. In addition, these AuNPs-doped films exhibited two peaks that are not present in the pure protein film. The first peak at 2θ = 37.7° is assigned to the crystal structure of AuNPs[340], whereas the second peak at 2θ = 3.6° corresponds

to a periodical d-spacing of 2.3 nm. This spacing is attributed to the arrangement of gold nanoparticles within the solid film. It suggests a tighter packing of the AuNPs in the 3D film than observed in a single molecule arrangement with STM (Figure 5.4B). To explore further the packing of the gold nanoparticles within the $CTPR16_{4Cys}$-AuNPs films, STM was performed (Figure 5.4D). A 1 µM solution of $CTPR16_{4Cys}$-AuNPs conjugates (1000 times higher than the previous concentration for single-molecule imaging) was deposited directly onto a gold surface. After solvent evaporation, a thin layer of $CTPR16_{4Cys}$AuNPs was formed. STM images of the formed layer showed rows of AuNPs homogeneously distributed within the film. AuNPs are closer than expected from linear protein packing, as the proteins intercrossed, minimizing AuNPs distances. The average inter-particle distance between AuNPs centers in the film is 4.2 ± 0.3 nm (Figure 5.4D), with a nanoparticle gap of ~ 0.6 nm. This smaller interparticle distance measured in the 2D film differs from the larger inter-particle distance determined for individual $CTPR16_{4Cys}$-AuNPs (Figure 5.4B) but agrees with tighter packing in the solid film previously determined by XRD (Figure 5.4C). However, the inter-particle distance in film reported by XRD (2.3 nm) and STM (4.2 nm) slightly differs since XRD reports on the 3D arrangement and STM on 2D surfaces.

Charge transport properties of both $CTPR16_{4Cys}$ protein and $CTPR16_{4Cys}$-AuNPs conjugate films were studied by measuring current-voltage (*I–V*) curves in the (−1 V, +1 V) interval (Figure 5.6). The absolute value of the applied bias was limited to 1 V, which is smaller than the thermoneutral voltage for water electrolysis.[57] Films were formed onto Si/SiO_2 wafers with interdigitated gold electrodes on top using different protein and conjugate batches to ensure reproducibility. The electrodes described a channel with a width *W* to length *L* ratio (*W/L*) of approximately 600, which minimized the effect of edge currents between the electrodes (see the Experimental

section 5.4.10 for details). Films showed an ohmic behavior (constant *G* in Figure 5.6B) at a low applied voltage interval (−0.3 V, 0.3 V). In this range, protein films showed an average conductivity value of 140 ± 19 nS m^{-1}, where the current was transported through 20 µm of protein film according to the inter-distance length (*L*) between the electrodes. Conductivity was calculated using the equation $\sigma = G \times L/(t \times W)$, where $G = I/V$ is the conductance obtained from the *I*–*V* curve slope. The thickness of each film (*t*) was measured by atomic force microscopy (AFM), and *W* and *L* were defined by the electrode design (*vide supra*). In the films doped with AuNPs, their conductivity increased by 4 orders of magnitude, with an average value of 1.37 ± 0.35 mS m^{-1} in the same applied voltage range. Measurements were performed across sets of independent batches of proteins and AuNP conjugates with high reproducibility of the current measurements when scaling the results by the film thickness (different curves in Figure 5.6A). To better compare the profile of the curves, Figure 5.6B shows the voltage dependence of the conductance normalized by its value in the low voltage regime (*G/Glow*). The *G/Glow-V* curves are symmetrical for the $CTPR16_{4Cys}$ and $CTPR16_{4Cys}$-AuNPs films. The conductance in the $CTPR16_{4Cys}$ films showed a significant increase with the applied voltage, different from the behavior observed for $CTPR16_{4Cys}$-AuNPs films. Assuming that, the edge resistivity is similar in the electrodes for all the films, these differences in the curve profile indicate differences in the main charge transport mechanism between the films with and without AuNPs. The normalized conductance of the $CTPR16_{4Cys}$ films showed an exponential increase at absolute values of voltage ≥ 0.4 V. This non-linear profile is consistent with the presence of charge-carrier blocking at the electrical contacts, which is characteristic of protonic conductivity[306,334]. This observation agrees with previously reported protonic charge transport for CTPR protein films[334]. On the contrary, the $CTPR16_{4Cys}$-AuNPs films showed a quasi-linear increase in conductance

for most of the explored voltage range (−1 V - 1 V), indicating a difference in their charge transport properties. The enhancement of the conductivity observed for the films with AuNPs is consistent with electron-like charge transport within the films. The inter-particle distance measured in the AuNP-doped films is compatible with hopping electron transfer between the AuNPs[341,342]. In addition, the described packing distance between consecutive layers within the protein films[332,343] is also compatible with hopping electron transfer between layers. These effects would facilitate electron transport, thus increasing the conductivity alongside the CTPR16$_{4Cys}$-AuNPs films. This hypothesis agrees with the observations extracted from the *G/Glow vs. V* curves. A precise characterization of the charge transport mechanism through the protein films with and without AuNPs would require deeper studies combining several techniques and analyzing the temperature and humidity dependence of the conductivity. However, the overall results shown here point to mainly protonic charge transport in the CTPRs films and the emergence of electronic charge transport in the CTPR16$_{4Cys}$-AuNPs films.

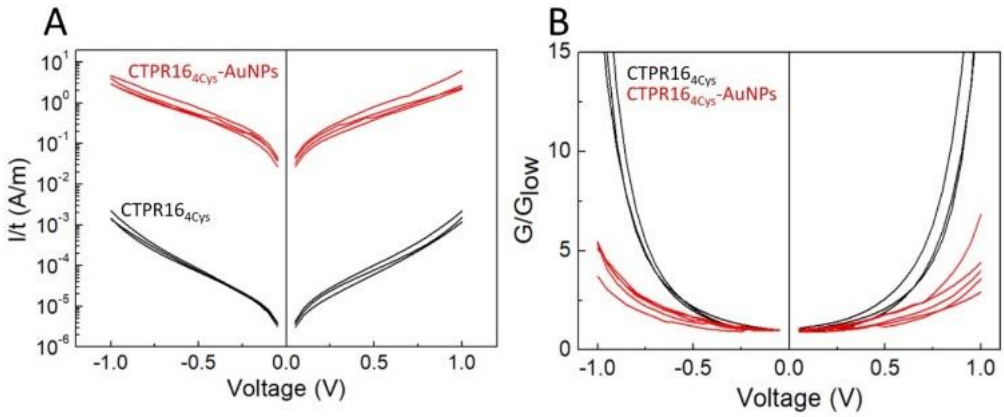

Figure 5.6. Transport properties of protein and protein-AuNPs thin films. A) Current intensity (I) vs applied voltage (V) plot obtained for different CTPR16 films in black and CTPR16$_{4Cys}$-AuNPs films in red. The Y axis shows the intensity corrected by the film thickness (t) in logarithmic

scale. B) Normalized conductance (*G*/*G*low) vs applied voltage (V) for CTPR16 films in black and CTPR16$_{4Cys}$-AuNPs film in red obtained from the curves of part A.

5.4. Conclusions

This work showed for the first time that gold nanoparticles, as an added electronic component, can be used to enhance the conductivity of protein-based films composed of engineered proteins. The main assets of this approach exploit (i) the rigid superhelical scaffold of CTPR proteins, (ii) their self-assembly properties, making it possible to form protein films, and (iii) the engineering of such proteins to form nanobioconjugates, enabling a strategy for controlled nanoparticles templating. Our study shows that a rigid superhelical scaffold, *i.e.*, the engineered CTPR protein, can be used to space up to 4 AuNPs per protein regularly. Solid protein films were then formed based on the self-assembly properties of CTPR proteins. Such films formed with pure protein or CTPR16$_{4Cys}$-AuNP conjugates exhibit long-range conductivity. CTPR16$_{4Cys}$-AuNPs films display a conductivity value of 1.37 ± 0.35 mS m^{-1}, four orders of magnitude larger than those measured for protein films.

Furthermore, AuNPs may promote a change in the charge transport properties, as reflected by differences in the *I*–*V* curve profiles. The results presented are consistent with different charge transfer mechanisms: a mainly protonic mechanism for the CTPR films and an additional electronic component for the AuNPs-doped films. The latter is favored by the short AuNP interparticle gap observed in the CTPR16$_{4Cys}$-AuNPs films (~0.6 nm), which is suitable for hopping electron transfer between AuNPs within the films. Although the conductive mechanisms along CTPR and CTPR16$_{4Cys}$-AuNPs films need further studies, our work opens the way to new designs

and understandings of long-range conductivity through protein, which is a fundamentally interesting and potentially significant development of bioelectronics materials. A generic approach for grafting any nanoparticle on the scaffold of the proteins without altering its structure is also demonstrated. Given the modular nature and the geometry of CTPR proteins, other inorganic nanomaterials could be arranged with adjustable inter-particle distances, making our approach a versatile tool for other applications such as optical coupling.

5.5. Experimental section

5.5.1. Materials

All chemical reagents were purchased from Aldrich and used without further purification. Ultrafiltration tubes used were Amicon Millipore with a regenerated cellulose membrane and a cut-off of 3 kDa. The cobalt NTA affinity resin used is ABT 6BCL-QHCo-100 (Agarose Bead Technology). Ultrapure reagent grade water (18.2 MΩ, Wasserlab at 25 °C) was used in all experiments. Gold(III) chloride hydrate ($HAuCl_4$, ≥99%), sodium citrate tribasic dihydrate (≥98%), sodium borohydride ($NaBH_4$, ≥96%), and amine-functionalized mercapto-poly-(ethyleneglycol) (HS-PEG2K-NH_2) were purchased from Sigma-Aldrich Merck. All glassware was washed with aqua regia, rinsed with Milli-Q water, and dried before use.

5.5.2. Measurements

UV-Vis and fluorescence spectra were recorded on a Synergy H1 microplate reader (Biotek) using 96-well plates. Fast Protein Liquid Chromatography (FPLC) was performed on a GE Life Science ÄKTA prime plus apparatus with a Superdex 75 column. Gel reader apparatus used was a Syngene G:Box Chemi XR5. Matrix-Assisted Laser Desorption/Ionization

Time Of Flight mass spectrometry (MALDI-TOF) was done by the National Center of Biotechnology (CNB) proteomic service in Madrid on an AB Sciex ABi 4800 MALDI TOF/TOF mass spectrometer. High-Resolution Transmission Electronic Microscopy (HR-TEM) measurements were done on a JEOL JEM 1400 Plus.

5.5.3. Gel filtration chromatography

Gel filtration chromatography was performed using an ÄKTA prime plus Fast Protein Liquid Chromatography (FPLC) equipment (GE Healthcare). After Ni-NTA column purification, the dialyzed elution fractions were injected into a Superdex 75 HR 10/30 size exclusion chromatography column (GE Healthcare) and run at 0.5 mL min^{-1} in PBS buffer with a detection UV absorption at 280 nm. The samples were collected in 0.5 mL fractions and stored at 4 °C.

5.5.4. High-resolution transmission electron microscopy (HR-TEM)

HR-TEM measurements were conducted on a JEOL JEM 1400 Plus microscope. The samples for HR-TEM were prepared by drop contact of the sample solution at 100 nM concentration of protein with a TEM grid and blotted to dry. The analysis of the images was performed using ImageJ software. The statistical analysis was performed using a Mann–Whitney non-parametrical test with GraphPad Prism software.

5.5.5. Scanning tunneling microscopy (STM)

STM images were obtained with a home-built Scanning Tunneling Microscope designed for room-temperature experiments[344]. All the images were recorded in ambient conditions using commercial gold substrates (Arrandee) cleaned before sample deposition by flame-annealing. Freshly cut gold wires (99.99%) were used as tips. Samples were prepared by the

drop-casting technique from an aqueous solution of $CTPR16_{4Cys}$-AuNPs. 0.1–10 nM concentrations for individual molecule imaging were used, while for layer formation, a 1 µM protein concentration was used. A drop of 200–300 µL of the solution was deposited over our 1 cm^2 gold substrates, which were rinsed with water several times after assembly periods of 10 to 30 minutes. The gold surface was then dried under N_2 flow. Images were recorded using bias voltage values between 0.1 V and 1.5 V and a setpoint current between 500 pA and 5 nA. The protein body could not be imaged in the range of voltages studied, reflecting its low electrical conductance. The typical apparent height of the AuNP was 0.4 nm, accounting for their expected poor coupling to the gold substrate. X-ray diffraction (XRD) was performed in a Panalytical X'Pert PRO diffractometer with Cu tube (lambda Kα = 1.54187 Å) operated at 45 kV, 40 mA, Ni beta filter, programmable divergence, and anti-scatter slits working in fixed mode, and fast linear detector (X'Celerator) working in scanning mode.

5.5.6. Gold nanoparticles synthesis

Gold nanoparticles (~3 nm) were prepared by fast reduction of $HAuCl_4$ (20 mL, 0.125 mM) with freshly prepared $NaBH_4$ (0.3 mL, 10 mM) in the presence of sodium citrate (0.25 mM) under vigorous stirring[345]. The solution color changed from yellow to reddish. After two minutes stirring, the seed solution was aged at 27 °C for 30 minutes before promoting sodium borohydride decomposition. Amine-functionalized mercapto-poly-(ethyleneglycol) with a molecular weight of 2000 g mol^{-1} was used for ligand exchange. An aqueous solution of HS-PEG2K-NH_2 (0.5 mL, 2.9 mM) was added dropwise to as-synthesized gold nanoparticles under vigorous stirring, and incubated for 2 h. PEG-modified gold nanoparticles were centrifuged using Millipore Amicon Centrifugal Filter Units (10 kDa) and finally dispersed in water.

5.5.7. Protein design and purification

Based on consensus CTPR16 protein, four cysteine residues were introduced in a loop position 33 of the CTPR repeats 2, 6, 10, and 14 to form $CTPR16_{4Cys}$ protein. The mutation was introduced in CTPR1 by quick-change site-directed mutagenesis. The $CTPR16_{4Cys}$ gene was generated from the CTPR1 wild type gene by sequential additions of CTPR1 wild type or mutated repeats, depending on the CTPR repetition number, and cloned into a pPro-EX-HTa vector. The protein was expressed as His-tagged fusion and purified using standard affinity chromatography methods as previously described[75]. The protein was dialyzed into PBS buffer (150 mM NaCl, 50 mM phosphate buffer pH 7.4) with 2 mM β-mercaptoethanol and stored frozen at −20 °C. The protein concentration was determined by UV-absorbance at 280 nm using the extinction coefficient calculated from the amino acid composition[346].

5.5.8. Modification of AuNPs and conjugation with $CTPR16_{4Cys}$

Protein 1 mL of amine-PEG AuNPs at 160 nM were incubated with 39 µL of freshly prepared 22.9 µM 4-(N-maleimidomethyl) cyclohexane-1-carboxylic acid 3-sulfo-N-hydroxysuccinimide ester (Sulfo-SMCC) dissolved in water in a microtube for 30 min at room temperature (final molar ratio Sulfo-SMCC : AuNPs = 5 : 1). The AuNPs concentration was calculated from their absorption at 510 nm using the following equation: $ln\ \varepsilon = 3.32111 \times ln\ D + 10.80505$, where ε is the molar extinction coefficient ($M^{-1}\ cm^{-1}$) and D is the nanoparticle core diameter in nm of the gold nanoparticles measured by TEM, according to Liu et al[347]. Protein cysteines were reduced using 5 mM dithiothreitol (DTT) for 45 minutes and purified using an Illustra NAP-5 desalting column equilibrated with a solution of 150 mM NaCl, 50 mM phosphate buffer pH 8.0. Before conjugation, the excess SulfoSMCC was removed from the AuNPs suspension by using an

ultrafiltration unit Amicon® Ultra – 0.5 mL with a 3000 Da molecular weight cut-off (MWCO) at 21 000 g for 5 min and by washing 5 times with 150 mM NaCl, 50 mM phosphate buffer pH 8.0. Purified AuNPs-SMCC were then incubated with 7.6 µL of 5.9 µM freshly reduced $CTPR16_{4Cys}$ at room temperature with 20 rpm spinning for 1 h (final molar ratio $CTPR16_{4Cys}$: AuNPs = 1 : 4). After nanoparticle conjugation, the reaction was blocked by adding 5 µL of 10 mM β-mercaptoethanol. After overnight incubation, $CTPR16_{4Cys}$-AuNPs conjugates were purified from the excess of unbound AuNPs and linker using protein His-Tag and Ni-NTA column. Free AuNPs were eluted in the flow-through, while $CTPR16_{4Cys}$-AuNPs conjugate was eluted from the nickel column with a 300 mM imidazole buffer solution.

5.5.9. Film formation

Protein solid ordered films were generated as previously described[332]. $CTPR16_{4Cys}$ protein alone and $CTPR16_{4Cys}$-AuNPs conjugates were diluted to 3% (w/v) protein concentration in 10 mM NaCl, 10 mM Na phosphate pH 7.0 buffer. The solutions were deposited on different surfaces, depending on the experiments to be performed. Quartz cuvette was used for circular dichroism (CD) analysis, glass surface for conductivity measurements, and silicon wafer for X-ray diffraction (XRD) analysis. The drop volumes also vary between 10 to 30 µL. The solvent was evaporated at room temperature for 12 hours, resulting in solid thin films.

5.5.10. Lithography of the electrodes

A pattern of interdigitated electrodes with a defined channel of 20 µm in length *L* and 11.8 mm in width *W* was fabricated through clean-room processes of “maskless” lithography (“Heidelberg DWL66fs” model) and thermal evaporation. A Si/ SiO_2 wafer was coated by 2 mm “AZ 1512HS” (MicroChemicals GmbH) positive resin and exposed to a λ = 405 nm laser that printed the designed electrode pattern. The wafer was then introduced

in an AZ351B developer (1 : 4 developer : water) to remove the resin parts exposed to the laser. To ensure that all the resin is removed, the wafer was further exposed to plasma (50 W) for 30 s. The revealed sample was introduced in a thermal evaporator (Nanosphere, de Oxford Vacuum Science model) where a chromium 5–10 nm thick layer was first evaporated to increase the adhesion to the substrate, followed by a 50 nm thick gold layer. Finally, a lift-off process was performed, introducing the sample in acetone to remove all the resin in the sample and obtain the desired pattern shown in Figure 5.7.

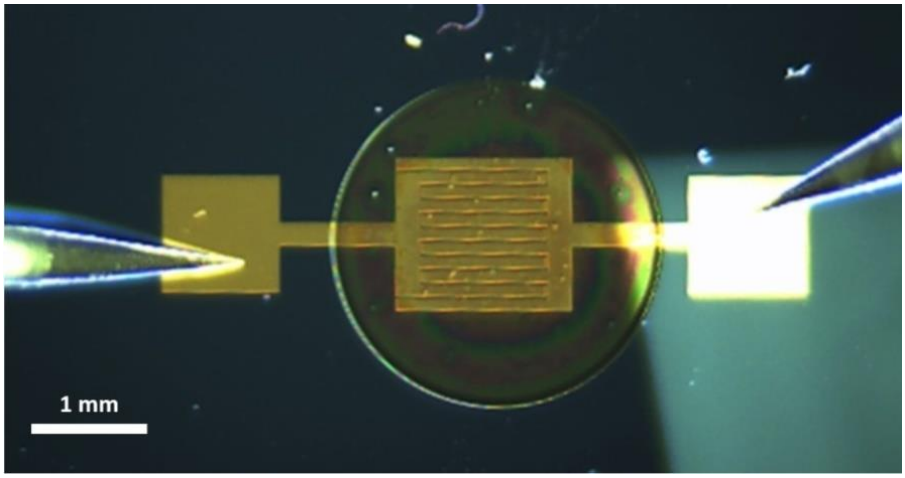

Figure 5.7. Set up used for conductive measurements. CTPR16$_{4Cys}$-AuNPs film deposited over silicon wafers with gold electrodes patterned over them.

5.5.11. Electrical conductivity measurements

To study the conductive properties of the CTPR16$_{4Cys}$ and CTPR6$_{4Cys}$-AuNPs, thin films of the protein and the conjugate devices were prepared over silicon wafers with gold electrodes patterned as described in the previous section (Figure 5.7). Using a Keithley 4200-SCS, current versus

voltage curves were recorded in the interval (−1 V, +1 V) for both the $CTPR16_{4Cys}$ protein and the $CTPR16_{4Cys}$-AuNPs conjugate. Olympus standard silicon nitride probes of 0.05 N m^{-1} and 18 kHz (OMCL-RC800PSA) were employed to contact the electrodes. The aspect ratio (*W/L*) of the interdigitated electrodes is 590, which allowed us to obtain measurable currents even for low conducting plain $CTPR16_{4Cys}$ films and reduce the effect of edge currents between the electrodes. The low conductance of $CTPR16_{4Cys}$ forced us to prepare a thicker film of this protein than the one with AuNP conjugate. Thus, 4–5 μm thick films for the protein and 20–100 nm thick films for the conjugate were prepared. The thickness of the films was measured using a profilometer for $CTPR16_{4Cys}$ films and an atomic force microscope (AFM) on jumping mode for the $CTPR16_{4Cys}$-AuNPs films.

6.GENERAL CONCLUSIONS

This thesis has focused on the design of protein and metallic nanomaterials hybrids. First, a systematic work using advanced spectroscopic techniques has been carried out for understanding the importance of metal coordinating residues within the protein for the fine tuning of the optical properties of gold nanoclusters. Then, several applications of designed CTPR proteins have been proved, in particular protein designs for sensing environmental parameters, correlative elemental-fluorescence imaging, and conductive biomaterials. In this sense, the initial hypothesis established at the beginning of this thesis, which states that repeat proteins, in particular the modular CTPR proteins, can be finely engineered in conjugation with metal nanoelements for their use in tailored applications, has been demonstrated in different scenarios. The conclusions regarding the objectives determined in the introductory chapter are detailed below:

- **Design of stable nanocluster-protein hybrids with optimized luminescent properties**. A careful investigation of the physicochemical phenomena rising photoluminescence in gold nanoclusters conjugated to precisely engineered CTPR proteins was performed. The role of metal coordination residues and protein stability were assessed using advance spectroscopical techniques. The interaction of uncapped nanoclusters with proteins carrying engineered metal coordination sites showed remarkable differences in PL emission wavelength and lifetime, depending on the chemical nature of those coordinating residues. Moreover, the described synthesis method offers an easy, green and quick way of developing photo-emissive NC-protein hybrids as an alternative to *in situ* nanocluster growth. Further studies can be

proposed to elucidate open questions, such as the molecular mechanisms implicated in the photoemission.

- **Design of photoactive nanocluster-protein hybrids that hold a specific environmental-sensing response.** In this chapter, CTPR proteins were evaluated as protein templates to direct the synthesis of different metal nanoclusters (Au, Ag and Cu), and those NC-protein hybrids tested as biosensors. The three metal NC-protein hybrids showed remarkable sensitivity and efficiency as temperature sensors. Furthermore, the AuNCs hybrids were able to detect nanomolar concentration of copper ions in solution and AgNCs detected the formation of ROS species.
- **Design of nanoclusters-protein hybrids for cellular and bioimaging applications**. Here, dual detection probes based on CTPR proteins were designed for correlative SXRFN and fluorescence microscopy. Three metallic NC templated by CTPR were assessed as SXRFN probes, AuNCs, NiNCs and CoNCs, of which AuNCs was the most stable and robust nano probe. Further fluorescence confocal microscopy of AuNCs-CTPR proteins carrying specific signal peptides was performed for evaluating AuNC-protein as fluorescent organelle-tags, which relies on external transfection agents for the cytosolic delivery of nanoclusters-CTPR proteins. Out of the different agents were tested, one showed promising results. Exciting work on developing correlative XRF-fluorescence microscopy organelle tags awaits in the future.
- **Design of CTPR protein scaffolds as templates for the stabilization and organization of gold nanoparticles to produce electroconductive biomaterials.** The work developed in this chapter showed that gold nanoparticles can be used to enhance four times the conductivity of pristine protein-based films. The careful design of CTPR protein allows to nanometric control the conjugation of AuNPs in a

desired pattern. Furthermore, AuNPs promote a change in the charge transport properties: a mainly protonic mechanism for the CTPR films and an additional electronic component for the AuNPs-doped films. The latter is favored by the short AuNP interparticle gap observed in the $CTPR16_{4Cys}$-AuNPs films, which is suitable for hopping electron transfer between AuNPs within the films. Thus, the methodology employed can act as a guide for ordering other interesting molecules in a controlled way onto protein films.

Overall, the studies carried out in this thesis are a demonstration of the synergistic use of modular protein design and the synthesis of metallic nanostructures to develop new hybrid tools for nanotechnological applications in several fields.

7.REFERENCES

1. Johnson, B. R. & Lam, S. K. Self-organization, Natural Selection, and Evolution: Cellular Hardware and Genetic Software. *Bioscience* **60**, 879–885 (2010).
2. Link, A. J., Mock, M. L. & Tirrell, D. A. Non-canonical amino acids in protein engineering. *Curr. Opin. Biotechnol.* **14**, 603–609 (2003).
3. Saad, S. & Jarosz, D. F. Protein self-assembly: A new frontier in cell signaling. *Curr. Opin. Cell Biol.* **69**, 62–69 (2021).
4. Chakrabortee, S. *et al.* Intrinsically Disordered Proteins Drive Emergence and Inheritance of Biological Traits. *Cell* **167**, 369-381.e12 (2016).
5. Walker, D. A., Kowalczyk, B., de la Cruz, M. O. & Grzybowski, B. A. Electrostatics at the nanoscale. *Nanoscale* **3**, 1316–1344 (2011).
6. Bishop, K. J. M., Wilmer, C. E., Soh, S. & Grzybowski, B. A. Nanoscale forces and their uses in self-assembly. *Small* **5**, 1600–1630 (2009).
7. Levy, Y. & Onuchic, J. N. Water and proteins: a love-hate relationship. *Proceedings of the National Academy of Sciences of the United States of America* vol. 101 3325–3326 (2004).
8. Papoian, G. A., Ulander, J., Eastwood, M. P., Luthey-Schulten, Z. & Wolynes, P. G. Water in protein structure prediction. *Proc. Natl. Acad. Sci. U. S. A.* **101**, 3352–3357 (2004).

9. Uebe, R. & Schüler, D. Magnetosome biogenesis in magnetotactic bacteria. *Nat. Rev. Microbiol.* **14**, 621–637 (2016).

10. Wegst, U. G. K., Bai, H., Saiz, E., Tomsia, A. P. & Ritchie, R. O. Bioinspired structural materials. *Nat. Mater.* **14**, 23–36 (2015).

11. Thomson, A. J. & Gray, H. B. Bio-inorganic chemistry. *Curr. Opin. Chem. Biol.* **2**, 155–158 (1998).

12. Putignano, V., Rosato, A., Banci, L. & Andreini, C. MetalPDB in 2018: a database of metal sites in biological macromolecular structures. *Nucleic Acids Res.* **46**, D459–D464 (2018).

13. Peters, J. W., Lanzilotta, W. N., Lemon, B. J. & Seefeldt, L. C. X-ray crystal structure of the Fe-only hydrogenase (CpI) from Clostridium pasteurianum to 1.8 angstrom resolution. *Science* **282**, 1853–1858 (1998).

14. Andreini, C., Cavallaro, G., Lorenzini, S. & Rosato, A. MetalPDB: a database of metal sites in biological macromolecular structures. *Nucleic Acids Res.* **41**, D312-9 (2013).

15. Mann, S. I., Heinisch, T., Ward, T. R. & Borovik, A. S. Coordination chemistry within a protein host: regulation of the secondary coordination sphere. *Chem. Commun.* **54**, 4413–4416 (2018).

16. Faraday, M. X. The Bakerian Lecture. —Experimental relations of gold (and other metals) to light. *Philosophical Transactions of the Royal Society of London* **147**, 145–181 (1857).

17. Chakraborty, I. & Pradeep, T. Atomically Precise Clusters of Noble Metals:

Emerging Link between Atoms and Nanoparticles. *Chem. Rev.* **117**, 8208–8271 (2017).

18. Watt, J., Cheong, S. & Tilley, R. D. How to control the shape of metal nanostructures in organic solution phase synthesis for plasmonics and catalysis. *Nano Today* **8**, 198–215 (2013).
19. Chakraborty, I. & Parak, W. J. Protein-induced shape control of noble metal nanoparticles. *Adv. Mater. Interfaces* **6**, 1801407 (2019).
20. Mori, T. & Hegmann, T. Determining the composition of gold nanoparticles: a compilation of shapes, sizes, and calculations using geometric considerations. *J. Nanopart. Res.* **18**, 295 (2016).
21. Klębowski, B., Depciuch, J., Parlińska-Wojtan, M. & Baran, J. Applications of Noble Metal-Based Nanoparticles in Medicine. *Int. J. Mol. Sci.* **19**, (2018).
22. Zhang, L. & Wang, E. Metal nanoclusters: New fluorescent probes for sensors and bioimaging. *Nano Today* **9**, 132–157 (2014).
23. Zhang, J. *et al.* Cargo loading within ferritin nanocages in preparation for tumor-targeted delivery. *Nat. Protoc.* **16**, 4878–4896 (2021).
24. Tao, Y., Li, M., Kim, B. & Auguste, D. T. Incorporating gold nanoclusters and target-directed liposomes as a synergistic amplified colorimetric sensor for HER2-positive breast cancer cell detection. *Theranostics* **7**, 899–911 (2017).
25. Kossatz, S. *et al.* Efficient treatment of breast cancer xenografts with

multifunctionalized iron oxide nanoparticles combining magnetic hyperthermia and anti-cancer drug delivery. *Breast Cancer Res.* **17**, 66 (2015).

26. Roudeau, S., Carmona, A., Perrin, L. & Ortega, R. Correlative organelle fluorescence microscopy and synchrotron X-ray chemical element imaging in single cells. *Anal. Bioanal. Chem.* **406**, 6979–6991 (2014).
27. Geng, X. & Grove, T. Z. Repeat protein mediated synthesis of gold nanoparticles: effect of protein shape on the morphological and optical properties. *RSC Adv.* **5**, 2062–2069 (2014).
28. Walsh, A. G. & Zhang, P. Thiolate-protected single-atom alloy nanoclusters: Correlation between electronic properties and catalytic activities. *Adv. Mater. Interfaces* **8**, 2001342 (2021).
29. Nikolaivits, E. *et al.* Versatile Fungal Polyphenol Oxidase with Chlorophenol Bioremediation Potential: Characterization and Protein Engineering. *Appl. Environ. Microbiol.* **84**, (2018).
30. Li, H., Zhu, W., Wan, A. & Liu, L. The mechanism and application of the protein-stabilized gold nanocluster sensing system. *Analyst* **142**, 567–581 (2017).
31. Arnold, F. H. Directed Evolution: Bringing New Chemistry to Life. *Angew. Chem. Int. Ed Engl.* **57**, 4143–4148 (2018).
32. Zastrow, M. L., Peacock, A. F. A., Stuckey, J. A. & Pecoraro, V. L. Hydrolytic catalysis and structural stabilization in a designed

metalloprotein. *Nat. Chem.* **4**, 118–123 (2011).

33. Wang, M. S., Hoegler, K. J. & Hecht, M. H. Unevolved De Novo Proteins Have Innate Tendencies to Bind Transition Metals. *Life* **9**, (2019).
34. Huang, P.-S., Boyken, S. E. & Baker, D. The coming of age of de novo protein design. *Nature* **537**, 320–327 (2016).
35. Jutz, G., van Rijn, P., Santos Miranda, B. & Böker, A. Ferritin: a versatile building block for bionanotechnology. *Chem. Rev.* **115**, 1653–1701 (2015).
36. Zang, J., Zheng, B., Zhang, X., Arosio, P. & Zhao, G. Design and site-directed compartmentalization of gold nanoclusters within the intrasubunit interfaces of ferritin nanocage. *J. Nanobiotechnology* **17**, 79 (2019).
37. Abe, S. *et al.* Control of the coordination structure of organometallic palladium complexes in an apo-ferritin cage. *J. Am. Chem. Soc.* **130**, 10512–10514 (2008).
38. Lu, Y. Metalloprotein and metallo-DNA/RNAzyme design: current approaches, success measures, and future challenges. *Inorg. Chem.* **45**, 9930–9940 (2006).
39. Zastrow, M. L. & Pecoraro, V. L. Designing functional metalloproteins: from structural to catalytic metal sites. *Coord. Chem. Rev.* **257**, 2565–2588 (2013).
40. Huang, P. *et al.* Dye-loaded ferritin nanocages for multimodal imaging and photothermal therapy. *Adv. Mater.* **26**, 6401–6408 (2014).
41. Romeo, M. V., López-Martínez, E., Berganza-Granda, J., Goñi-de-Cerio, F.

& Cortajarena, A. L. Biomarker sensing platforms based on fluorescent metal nanoclusters. *Nanoscale Advances* **3**, 1331–1341 (2021).

42. Gurruchaga-Pereda, J. *et al.* Flavin Bioorthogonal Photocatalysis Toward Platinum Substrates. *ACS Catal.* **10**, 187–196 (2020).
43. Gurruchaga-Pereda, J. *et al.* Enhancing the Photocatalytic Conversion of Pt(IV) Substrates by Flavoprotein Engineering. *J. Phys. Chem. Lett.* **12**, 4504–4508 (2021).
44. Lombardi, A., Nastri, F. & Pavone, V. Peptide-based heme-protein models. *Chem. Rev.* **101**, 3165–3189 (2001).
45. Lombardi, A. *et al.* Miniaturized metalloproteins: application to iron-sulfur proteins. *Proc. Natl. Acad. Sci. U. S. A.* **97**, 11922–11927 (2000).
46. Cochran, F. V. *et al.* Computational de novo design and characterization of a four-helix bundle protein that selectively binds a nonbiological cofactor. *J. Am. Chem. Soc.* **127**, 1346–1347 (2005).
47. Lu, Y. Design and engineering of metalloproteins containing unnatural amino acids or non-native metal-containing cofactors. *Curr. Opin. Chem. Biol.* **9**, 118–126 (2005).
48. Jantz, D. & Berg, J. M. Expanding the DNA-recognition repertoire for zinc finger proteins beyond 20 amino acids. *J. Am. Chem. Soc.* **125**, 4960–4961 (2003).
49. Zhang, P. *et al.* The Third Generation of Artificial Dye-Decolorizing Peroxidase Rationally Designed in Myoglobin. *ACS Catal.* **9**, 7888–7893

(2019).

50. Nastri, F. *et al.* Engineering Metalloprotein Functions in Designed and Native Scaffolds. *Trends Biochem. Sci.* **44**, 1022–1040 (2019).
51. Hosseinzadeh, P. & Lu, Y. Design and fine-tuning redox potentials of metalloproteins involved in electron transfer in bioenergetics. *Biochim. Biophys. Acta* **1857**, 557–581 (2016).
52. Shi, W. *et al.* Characterization of metalloproteins by high-throughput X-ray absorption spectroscopy. *Genome Res.* **21**, 898–907 (2011).
53. Shi, W. & Chance, M. R. Metalloproteomics: forward and reverse approaches in metalloprotein structural and functional characterization. *Curr. Opin. Chem. Biol.* **15**, 144–148 (2011).
54. Newberry, R. W. & Raines, R. T. Secondary Forces in Protein Folding. *ACS Chem. Biol.* **14**, 1677–1686 (2019).
55. Dill, K. A. & MacCallum, J. L. The protein-folding problem, 50 years on. *Science* **338**, 1042–1046 (2012).
56. Mayor, U., Johnson, C. M., Daggett, V. & Fersht, A. R. Protein folding and unfolding in microseconds to nanoseconds by experiment and simulation. *Proc. Natl. Acad. Sci. U. S. A.* **97**, 13518–13522 (2000).
57. Snow, C. D., Nguyen, H., Pande, V. S. & Gruebele, M. Absolute comparison of simulated and experimental protein-folding dynamics. *Nature* **420**, 102–106 (2002).
58. Schuler, B. & Hofmann, H. Single-molecule spectroscopy of protein folding

dynamics--expanding scope and timescales. *Curr. Opin. Struct. Biol.* **23**, 36–47 (2013).

59. Levinthal, C. How to fold graciously. *Mossbauer spectroscopy in biological systems* **67**, 22–24 (1969).
60. Dill, K. A. & Chan, H. S. From Levinthal to pathways to funnels. *Nat. Struct. Biol.* **4**, 10–19 (1997).
61. Whitford, P. C. & Onuchic, J. N. What protein folding teaches us about biological function and molecular machines. *Curr. Opin. Struct. Biol.* **30**, 57–62 (2015).
62. Norn, C. *et al.* Protein sequence design by conformational landscape optimization. *Proc. Natl. Acad. Sci. U. S. A.* **118**, e2017228118 (2021).
63. Berman, H., Henrick, K. & Nakamura, H. Announcing the worldwide Protein Data Bank. *Nat. Struct. Biol.* **10**, 980 (2003).
64. Jumper, J. *et al.* Highly accurate protein structure prediction with AlphaFold. *Nature* (2021).
65. Baek, M. *et al.* Accurate prediction of protein structures and interactions using a three-track neural network. *Science* **373**, 871–876 (2021).
66. Hassoun, S. *et al.* Artificial Intelligence for Biology. *Integr. Comp. Biol.* **61**, 2267–2275 (2022).
67. Artificial intelligence in structural biology is here to stay. *Nature* **595**, 625–626 (2021).
68. Skolnick, J., Gao, M., Zhou, H. & Singh, S. AlphaFold 2: Why It Works and

Its Implications for Understanding the Relationships of Protein Sequence, Structure, and Function. *J. Chem. Inf. Model.* **61**, 4827–4831 (2021).

69. Baldwin, C. Y. & Clark, K. B. Modularity in the Design of Complex Engineering Systems. in *Complex Engineered Systems: Science Meets Technology* (eds. Braha, D., Minai, A. A. & Bar-Yam, Y.) 175–205 (Springer Berlin Heidelberg, 2006).
70. Selivanovitch, E. & Douglas, T. Virus capsid assembly across different length scales inspire the development of virus-based biomaterials. *Curr. Opin. Virol.* **36**, 38–46 (2019).
71. Lunde, B. M., Moore, C. & Varani, G. RNA-binding proteins: modular design for efficient function. *Nat. Rev. Mol. Cell Biol.* **8**, 479–490 (2007).
72. Maervoet, V. E. T. & Briers, Y. Synthetic biology of modular proteins. *Bioengineered* **8**, 196–202 (2017).
73. Andrade, M. A., Perez-Iratxeta, C. & Ponting, C. P. Protein repeats: structures, functions, and evolution. *J. Struct. Biol.* **134**, 117–131 (2001).
74. Delucchi, M., Schaper, E., Sachenkova, O., Elofsson, A. & Anisimova, M. A New Census of Protein Tandem Repeats and Their Relationship with Intrinsic Disorder. *Genes* **11**, (2020).
75. Kajander, T., Cortajarena, A. L. & Regan, L. Consensus design as a tool for engineering repeat proteins. *Methods Mol. Biol.* **340**, 151–170 (2006).
76. Jäckel, C., Bloom, J. D., Kast, P., Arnold, F. H. & Hilvert, D. Consensus protein design without phylogenetic bias. *J. Mol. Biol.* **399**, 541–546 (2010).

77. Chakrabarty, B. & Parekh, N. DbStRiPs: Database of structural repeats in proteins. *Protein Sci.* **31**, 23–36 (2022).

78. Mosavi, L. K., Cammett, T. J., Desrosiers, D. C. & Peng, Z.-Y. The ankyrin repeat as molecular architecture for protein recognition. *Protein Sci.* **13**, 1435–1448 (2004).

79. Peifer, M., Berg, S. & Reynolds, A. B. A repeating amino acid motif shared by proteins with diverse cellular roles. *Cell* **76**, 789–791 (1994).

80. Parmeggiani, F. *et al.* Designed armadillo repeat proteins as general peptide-binding scaffolds: consensus design and computational optimization of the hydrophobic core. *J. Mol. Biol.* **376**, 1282–1304 (2008).

81. Stumpp, M. T., Forrer, P., Binz, H. K. & Plückthun, A. Designing repeat proteins: modular leucine-rich repeat protein libraries based on the mammalian ribonuclease inhibitor family. *J. Mol. Biol.* **332**, 471–487 (2003).

82. Scheufler, C. *et al.* Structure of TPR domain-peptide complexes: critical elements in the assembly of the Hsp70-Hsp90 multichaperone machine. *Cell* **101**, 199–210 (2000).

83. Burroughs, A. M. & Aravind, L. Identification of Uncharacterized Components of Prokaryotic Immune Systems and Their Diverse Eukaryotic Reformulations. *J. Bacteriol.* **202**, (2020).

84. López-Andarias, J. *et al.* Toward bioelectronic nanomaterials: Photoconductivity in protein–porphyrin hybrids wrapped around SWCNT. *Adv. Funct. Mater.* **28**, 1704031 (2018).

85. Sanchez-deAlcazar, D. *et al.* Engineered protein-based functional nanopatterned materials for bio-optical devices. *Nanoscale Adv.* **1**, 3980–3991 (2019).

86. Sánchez-deAlcázar, D., Velasco-Lozano, S., Zeballos, N., López-Gallego, F. & Cortajarena, A. L. Biocatalytic Protein-Based Materials for Integration into Energy Devices. *Chembiochem* **20**, 1977–1985 (2019).

87. Aires, A. *et al.* A Simple Approach to Design Proteins for the Sustainable Synthesis of Metal Nanoclusters. *Angew. Chem. Int. Ed Engl.* **58**, 6214–6219 (2019).

88. Aires, A., Fernández-Luna, V., Fernández-Cestau, J., Costa, R. D. & Cortajarena, A. L. White-emitting Protein-Metal Nanocluster Phosphors for Highly Performing Biohybrid Light-Emitting Diodes. *Nano Lett.* **20**, 2710–2716 (2020).

89. Aires, A., Möller, M. & Cortajarena, A. L. Protein Design for the Synthesis and Stabilization of Highly Fluorescent Quantum Dots. *Chem. Mater.* **32**, 5729–5738 (2020).

90. D'Andrea, L. D. & Regan, L. TPR proteins: the versatile helix. *Trends Biochem. Sci.* **28**, 655–662 (2003).

91. Mejias, S. H. *et al.* Assembly of designed protein scaffolds into monolayers for nanoparticle patterning. *Colloids Surf. B Biointerfaces* **141**, 93–101 (2016).

92. Couleaud, P. *et al.* Designed Modular Proteins as Scaffolds To Stabilize

Fluorescent Nanoclusters. *Biomacromolecules* **16**, 3836–3844 (2015).

93. Mejías, S. H. *et al.* Repeat protein scaffolds: Ordering photo- and electroactive molecules in solution and solid state. *Chem. Sci.* **7**, 4842–4847 (2016).
94. Mejias, S. H. *et al.* Repeat proteins as versatile scaffolds for arrays of redox-active FeS clusters. *Chem. Commun.* **55**, 3319–3322 (2019).
95. Geng, X., Roth, K. L., Freyman, M. C., Liu, J. & Grove, T. Z. Seed-mediated biomineralizaton toward the high yield production of gold nanoprisms. *Chem. Commun.* **52**, 9829–9832 (2016).
96. Geng, X. & Grove, T. Z. Synthesis of Triangular Silver and Gold Nanoprisms Using Consensus Sequence Tetratricopeptide Repeat Proteins. *Methods Mol. Biol.* **1798**, 141–153 (2018).
97. Mann, S. Molecular recognition in biomineralization. *Nature* **332**, 119–124 (1988).
98. Herman, A., Addadi, L. & Weiner, S. Interactions of sea-urchin skeleton macromolecules with growing calcite crystals— a study of intracrystalline proteins. *Nature* **331**, 546–548 (1988).
99. Meldrum, F. C., Wade, V. J., Nimmo, D. L., Heywood, B. R. & Mann, S. Synthesis of inorganic nanophase materials in supramolecular protein cages. *Nature* **349**, 684–687 (1991).
100. Douglas, T. *et al.* Synthesis and Structure of an Iron(III) Sulfide-Ferritin Bioinorganic Nanocomposite. *Science* **269**, 54–57 (1995).

101. Kramer, R. M., Li, C., Carter, D. C., Stone, M. O. & Naik, R. R. Engineered protein cages for nanomaterial synthesis. *J. Am. Chem. Soc.* **126**, 13282–13286 (2004).

102. Brown, S. Metal-recognition by repeating polypeptides. *Nat. Biotechnol.* **15**, 269–272 (1997).

103. Whaley, S. R., English, D. S., Hu, E. L., Barbara, P. F. & Belcher, A. M. Selection of peptides with semiconductor binding specificity for directed nanocrystal assembly. *Nature* **405**, 665–668 (2000).

104. Seker, U. O. S. *et al.* Adsorption behavior of linear and cyclic genetically engineered platinum binding peptides. *Langmuir* **23**, 7895–7900 (2007).

105. Naik, R. R., Stringer, S. J., Agarwal, G., Jones, S. E. & Stone, M. O. Biomimetic synthesis and patterning of silver nanoparticles. *Nat. Mater.* **1**, 169–172 (2002).

106. Dickerson, M. B. *et al.* Identification and design of peptides for the rapid, high-yield formation of nanoparticulate TiO2 from aqueous solutions at room temperature. *Chem. Mater.* **20**, 1578–1584 (2008).

107. Klem, M. T. *et al.* Bio-inspired synthesis of protein-encapsulated CoPt nanoparticles. *Adv. Funct. Mater.* **15**, 1489–1494 (2005).

108. Falkner, J. C. *et al.* Virus crystals as nanocomposite scaffolds. *J. Am. Chem. Soc.* **127**, 5274–5275 (2005).

109. Mo, X., Krebs, M. P. & Yu, S. M. Directed synthesis and assembly of nanoparticles using purple membrane. *Small* **2**, 526–529 (2006).

110. Scheibel, T. *et al.* Conducting nanowires built by controlled self-assembly of amyloid fibers and selective metal deposition. *Proc. Natl. Acad. Sci. U. S. A.* **100**, 4527–4532 (2003).

111. Lee, S.-K., Yun, D. S. & Belcher, A. M. Cobalt ion mediated self-assembly of genetically engineered bacteriophage for biomimetic Co-Pt hybrid material. *Biomacromolecules* **7**, 14–17 (2006).

112. Knez, M. *et al.* Biotemplate Synthesis of 3-nm Nickel and Cobalt Nanowires. *Nano Lett.* **3**, 1079–1082 (2003).

113. Slocik, J. M., Kim, S. N., Whitehead, T. A., Clark, D. S. & Naik, R. R. Biotemplated metal nanowires using hyperthermophilic protein filaments. *Small* **5**, 2038–2042 (2009).

114. Xie, J., Zheng, Y. & Ying, J. Y. Protein-directed synthesis of highly fluorescent gold nanoclusters. *J. Am. Chem. Soc.* **131**, 888–889 (2009).

115. Chiu, C.-Y. *et al.* Platinum nanocrystals selectively shaped using facet-specific peptide sequences. *Nat. Chem.* **3**, 393–399 (2011).

116. Kobayashi, M., Seki, M., Tabata, H., Watanabe, Y. & Yamashita, I. Fabrication of aligned magnetic nanoparticles using tobamoviruses. *Nano Lett.* **10**, 773–776 (2010).

117. Lee, S.-Y., Royston, E., Culver, J. N. & Harris, M. T. Improved metal cluster deposition on a genetically engineered tobacco mosaic virus template. *Nanotechnology* **16**, S435-41 (2005).

118. Kim, J.-W. *et al.* Cobalt oxide hollow nanoparticles derived by bio-

templating. *Chem. Commun.* 4101–4103 (2005).

119. Lee, I. H., Ahn, B., Lee, J. M., Lee, C. S. & Jung, Y. A facile synthesis of fluorescent silver nanoclusters with human ferritin as a synthetic and interfacing ligand. *Analyst* **140**, 3543–3550 (2015).
120. Lin, X. *et al.* Chimeric ferritin nanocages for multiple function loading and multimodal imaging. *Nano Lett.* **11**, 814–819 (2011).
121. Jin, R., Zeng, C., Zhou, M. & Chen, Y. Atomically Precise Colloidal Metal Nanoclusters and Nanoparticles: Fundamentals and Opportunities. *Chem. Rev.* **116**, 10346–10413 (2016).
122. You, Q. & Chen, Y. Ultrabright, highly heat-stable gold nanoclusters through functional ligands and hydrothermally-induced luminescence enhancement. *J. Mater. Chem.* **6**, 9703–9712 (2018).
123. Xiao, Y., Patolsky, F., Katz, E., Hainfeld, J. F. & Willner, I. “Plugging into Enzymes”: nanowiring of redox enzymes by a gold nanoparticle. *Science* **299**, 1877–1881 (2003).
124. Beloqui, A. & Cortajarena, A. L. Protein-based functional hybrid bionanomaterials by bottom-up approaches. *Curr. Opin. Struct. Biol.* **63**, 74–81 (2020).
125. Maity, B., Abe, S. & Ueno, T. Observation of gold sub-nanocluster nucleation within a crystalline protein cage. *Nat. Commun.* **8**, 14820 (2017).
126. Guével, X. L., Daum, N. & Schneider, M. Synthesis and characterization of human transferrin-stabilized gold nanoclusters. *Nanotechnology* **22**,

275103 (2011).

127. Sarikaya, M., Tamerler, C., Jen, A. K.-Y., Schulten, K. & Baneyx, F. Molecular biomimetics: nanotechnology through biology. *Nat. Mater.* **2**, 577–585 (2003).

128. Schaaff, T. G., Knight, G., Shafigullin, M. N., Borkman, R. F. & Whetten, R. L. Isolation and Selected Properties of a 10.4 kDa Gold:Glutathione Cluster Compound. *J. Phys. Chem. B* **102**, 10643–10646 (1998).

129. Le Guével, X., Trouillet, V., Spies, C., Jung, G. & Schneider, M. Synthesis of Yellow-Emitting Platinum Nanoclusters by Ligand Etching. *J. Phys. Chem. C* **116**, 6047–6051 (2012).

130. Shichibu, Y. *et al.* Extremely high stability of glutathionate-protected Au25 clusters against core etching. *Small* **3**, 835–839 (2007).

131. Luo, Z. *et al.* From aggregation-induced emission of Au(I)-thiolate complexes to ultrabright Au(0)@Au(I)-thiolate core-shell nanoclusters. *J. Am. Chem. Soc.* **134**, 16662–16670 (2012).

132. Xu, Y. *et al.* The role of protein characteristics in the formation and fluorescence of Au nanoclusters. *Nanoscale* **6**, 1515–1524 (2014).

133. Xu, Y., Palchoudhury, S., Qin, Y., Macher, T. & Bao, Y. Make conjugation simple: a facile approach to integrated nanostructures. *Langmuir* **28**, 8767–8772 (2012).

134. Aires, A., Sousaraei, A., Möller, M., Cabanillas-Gonzalez, J. & Cortajarena, A. L. Boosting the Photoluminescent Properties of Protein-Stabilized Gold

Nanoclusters through Protein Engineering. *Nano Lett.* **21**, 9347–9353 (2021).

135. Griep, M. H. & Bedford, N. M. Amino-acid conjugated protein–Au nanoclusters with tuneable fluorescence properties. *J. Phys. Mater.* **3**, 045002 (2020).
136. Zhang, L. X-Ray Absorption Spectroscopy of Metalloproteins. *Methods Mol. Biol.* **1876**, 179–195 (2019).
137. Londoño-Larrea, P., Vanegas, J. P., Cuaran-Acosta, D., Zaballos-García, E. & Pérez-Prieto, J. Water-Soluble Naked Gold Nanoclusters Are Not Luminescent. *Chemistry* **23**, 8137–8141 (2017).
138. Kajander, T., Cortajarena, A. L., Mochrie, S. & Regan, L. Structure and stability of designed TPR protein superhelices: unusual crystal packing and implications for natural TPR proteins. *Acta Crystallogr. D Biol. Crystallogr.* **63**, 800–811 (2007).
139. Main, E. R. G., Xiong, Y., Cocco, M. J., D'Andrea, L. & Regan, L. Design of stable alpha-helical arrays from an idealized TPR motif. *Structure* **11**, 497–508 (2003).
140. Wu, Z. *et al.* Unraveling the Impact of Gold(I)-Thiolate Motifs on the Aggregation-Induced Emission of Gold Nanoclusters. *Angew. Chem. Int. Ed Engl.* **59**, 9934–9939 (2020).
141. Zheng, J., Zhang, C. & Dickson, R. M. Highly fluorescent, water-soluble, size-tunable gold quantum dots. *Phys. Rev. Lett.* **93**, 077402 (2004).

142. Pyykkö, P. Structural properties: magic nanoclusters of gold. *Nat. Nanotechnol.* **2**, 273–274 (2007).

143. Chevrier, D. M., Chatt, A. & Zhang, P. Properties and applications of protein-stabilized fluorescent gold nanoclusters: short review. *J. of Nanophotonics* **6**, 064504 (2012).

144. Xu, S. *et al.* A visual sensor array for pattern recognition analysis of proteins using novel blue-emitting fluorescent gold nanoclusters. *Anal. Chem.* **86**, 11634–11639 (2014).

145. Peters, S., Peredkov, S., Neeb, M., Eberhardt, W. & Al-Hada, M. Size-dependent XPS spectra of small supported Au-clusters. *Surf. Sci.* **608**, 129–134 (2013).

146. Zhu, M., Aikens, C. M., Hollander, F. J., Schatz, G. C. & Jin, R. Correlating the crystal structure of a thiol-protected Au25 cluster and optical properties. *J. Am. Chem. Soc.* **130**, 5883–5885 (2008).

147. Zheng, J., Zhou, C., Yu, M. & Liu, J. Different sized luminescent gold nanoparticles. *Nanoscale* **4**, 4073–4083 (2012).

148. Wu, Z. & Jin, R. On the ligand's role in the fluorescence of gold nanoclusters. *Nano Lett.* **10**, 2568–2573 (2010).

149. Selvan, D. *et al.* Intrinsically fluorescent gold nanoclusters stabilized within a copper storage protein that follow the Irving-Williams trend in metal ion sensing. *Analyst* **144**, 3949–3958 (2019).

150. Yang, T. *et al.* P band intermediate state (PBIS) tailors photoluminescence

emission at confined nanoscale interface. *Communications Chemistry* **2**, 1–11 (2019).

151. Yang, X., Shi, M., Zhou, R., Chen, X. & Chen, H. Blending of HAuCl4 and histidine in aqueous solution: a simple approach to the Au10 cluster. *Nanoscale* **3**, 2596–2601 (2011).
152. Gatchell, M. *et al.* Complexes of gold and imidazole formed in helium nanodroplets. *Phys. Chem. Chem. Phys.* **20**, 7739–7745 (2018).
153. Mei, J., Leung, N. L. C., Kwok, R. T. K., Lam, J. W. Y. & Tang, B. Z. Aggregation-Induced Emission: Together We Shine, United We Soar! *Chem. Rev.* **115**, 11718–11940 (2015).
154. Pyo, K. *et al.* Ultrabright Luminescence from Gold Nanoclusters: Rigidifying the Au(I)-Thiolate Shell. *J. Am. Chem. Soc.* **137**, 8244–8250 (2015).
155. Yang, R. *et al.* New Insights on the Bonding Properties of BCC-like Au38S2(SR)20 Nanoclusters from X-ray Absorption Spectroscopy. *J. Phys. Chem. C* **122**, 22776–22782 (2018).
156. Chevrier, D. M. *et al.* Structure and formation of highly luminescent protein-stabilized gold clusters. *Chem. Sci.* **9**, 2782–2790 (2018).
157. Miller, J. T. *et al.* The effect of gold particle size on AuAu bond length and reactivity toward oxygen in supported catalysts. *J. Catal.* **240**, 222–234 (2006).
158. Chevrier, D. M. *et al.* Molecular-Scale Ligand Effects in Small Gold-Thiolate Nanoclusters. *J. Am. Chem. Soc.* **140**, 15430–15436 (2018).

159. Paramanik, B., Kundu, A., Chattopadhyay, K. & Patra, A. Study of binding interactions between MPT63 protein and Au nanocluster. *RSC Adv.* **4**, 35059–35066 (2014).

160. Guo, Y. *et al.* Histidine-mediated synthesis of chiral fluorescence gold nanoclusters: insight into the origin of nanoscale chirality. *RSC Adv.* **5**, 61449–61454 (2015).

161. Ravel, B. & Newville, M. ATHENA, ARTEMIS, HEPHAESTUS: data analysis for X-ray absorption spectroscopy using IFEFFIT. *J. Synchrotron Radiat.* **12**, 537–541 (2005).

162. Hulanicki, A., Glab, S. & Ingman, F. Chemical sensors: definitions and classification. *J. Macromol. Sci. Part A Pure Appl. Chem.* **63**, 1247–1250 (1991).

163. Pearce, J. M. S. A brief history of the clinical thermometer. *QJM* **95**, 251–252 (2002).

164. Whiteside, T. L. The tumor microenvironment and its role in promoting tumor growth. *Oncogene* **27**, 5904–5912 (2008).

165. Singh, I. S. & Hasday, J. D. Fever, hyperthermia and the heat shock response. *Int. J. Hyperthermia* **29**, 423–435 (2013).

166. Ginsberg, M. D. & Busto, R. Combating hyperthermia in acute stroke: a significant clinical concern. *Stroke* **29**, 529–534 (1998).

167. Repasky, E. A., Evans, S. S. & Dewhirst, M. W. Temperature matters! And why it should matter to tumor immunologists. *Cancer Immunol Res* **1**, 210–

216 (2013).

168. Dewhirst, M. W., Lee, C.-T. & Ashcraft, K. A. The future of biology in driving the field of hyperthermia. *Int. J. Hyperthermia* **32**, 4–13 (2016).
169. England, H. R. *et al.* The therapeutic application of hyperthermia in the bladder. *Br. J. Urol.* **47**, 849–852 (1975).
170. Xue, K. *et al.* A Sensitive and Reliable Organic Fluorescent Nanothermometer for Noninvasive Temperature Sensing. *J. Am. Chem. Soc.* **143**, 14147–14157 (2021).
171. Mohammed, L. J. & Omer, K. M. Carbon Dots as New Generation Materials for Nanothermometer: Review. *Nanoscale Res. Lett.* **15**, 182 (2020).
172. Donner, J. S., Thompson, S. A., Kreuzer, M. P., Baffou, G. & Quidant, R. Mapping intracellular temperature using green fluorescent protein. *Nano Lett.* **12**, 2107–2111 (2012).
173. Wang, C., Ling, L., Yao, Y. & Song, Q. One-step synthesis of fluorescent smart thermo-responsive copper clusters: A potential nanothermometer in living cells. *Nano Res.* **8**, 1975–1986 (2015).
174. Zhang, W. *et al.* Supramolecular Self-Assembly Bioinspired Synthesis of Luminescent Gold Nanocluster-Embedded Peptide Nanofibers for Temperature Sensing and Cellular Imaging. *Bioconjug. Chem.* **28**, 2224–2229 (2017).
175. Chen, X., Essner, J. B. & Baker, G. A. Exploring luminescence-based

temperature sensing using protein-passivated gold nanoclusters. *Nanoscale* **6**, 9594–9598 (2014).

176. Han, B., Hou, X., Xiang, R. & He, G. Synthesis of highly luminescent Cu/Ag bimetal nanoclusters and their application in a temperature sensor. *Anal. Methods* **9**, 4028–4032 (2017).
177. Espinosa, A. *et al.* Photoactivated Nanoscale Temperature Gradient Detection Using X-ray Absorption Spectroscopy as a Direct Nanothermometry Method. *Nano Lett.* **21**, 769–777 (2021).
178. Chen, Z.-H., Fan, Q.-X., Han, X.-Y., Shi, G. & Zhang, M. Design of smart chemical 'tongue' sensor arrays for pattern-recognition-based biochemical sensing applications. *Trends Analyt. Chem.* **124**, 115794 (2020).
179. Shellaiah, M. & Sun, K. W. Luminescent Metal Nanoclusters for Potential Chemosensor Applications. *Chemosensors* **5**, 36 (2017).
180. Zhang, L. *et al.* DNA-templated Ag nanoclusters as fluorescent probes for sensing and intracellular imaging of hydroxyl radicals. *Talanta* **118**, 339–347 (2014).
181. Li, J., Yu, J., Huang, Y., Zhao, H. & Tian, L. Highly Stable and Multiemissive Silver Nanoclusters Synthesized in Situ in a DNA Hydrogel and Their Application for Hydroxyl Radical Sensing. *ACS Appl. Mater. Interfaces* **10**, 26075–26083 (2018).
182. Li, M., Yang, D.-P., Wang, X., Lu, J. & Cui, D. Mixed protein-templated luminescent metal clusters (Au and Pt) for H2O2 sensing. *Nanoscale Res.*

Lett. **8**, 182 (2013).

183. Kawasaki, H., Hamaguchi, K., Osaka, I. & Arakawa, R. Ph-dependent synthesis of pepsin-mediated gold nanoclusters with blue green and red fluorescent emission. *Adv. Funct. Mater.* **21**, 3508–3515 (2011).
184. Liu, L., Jiang, H. & Wang, X. Design of dual metal ions/dual amino acids integrated photoluminescent logic gate by high-molecular weight protein-localized Au nanoclusters. *Nano Res.* **11**, 311–322 (2018).
185. Feng, J. *et al.* pH-Regulated Synthesis of Trypsin-Templated Copper Nanoclusters with Blue and Yellow Fluorescent Emission. *ACS Omega* **2**, 9109–9117 (2017).
186. Guo, W., Yuan, J. & Wang, E. Oligonucleotide-stabilized Ag nanoclusters as novel fluorescence probes for the highly selective and sensitive detection of the Hg2+ ion. *Chem. Commun.* 3395–3397 (2009).
187. Mattocks, J. A., Ho, J. V. & Cotruvo, J. A., Jr. A Selective, Protein-Based Fluorescent Sensor with Picomolar Affinity for Rare Earth Elements. *J. Am. Chem. Soc.* **141**, 2857–2861 (2019).
188. Strimbu, K. & Tavel, J. A. What are biomarkers? *Curr. Opin. HIV AIDS* **5**, 463–466 (2010).
189. Lim, M. L., Jungebluth, P. & Macchiarini, P. Chapter 32 - Regenerative Medicine for Diseases of the Respiratory System. in *Translational Regenerative Medicine* (eds. Atala, A. & Allickson, J. G.) 449–456 (Academic Press, 2015).

190. Dienstmann, R., Rodon, J. & Tabernero, J. Biomarker-driven patient selection for early clinical trials. *Curr. Opin. Oncol.* **25**, 305–312 (2013).

191. Song, C. *et al.* DNA-Templated Fluorescent Nanoclusters for Metal Ions Detection. *Molecules* **24**, 4189 (2019).

192. Capek, I. *DNA Engineered Noble Metal Nanoparticles: Fundamentals and State-of-the-art-of Nanobiotechnology*. 1–656 (John Wiley and Sons, Inc. ; Scrivener Publishing {LLC}, 2015).

193. Goswami, N. *et al.* Copper quantum clusters in protein matrix: potential sensor of Pb2+ ion. *Anal. Chem.* **83**, 9676–9680 (2011).

194. Wu, Y.-T., Shanmugam, C., Tseng, W.-B., Hiseh, M.-M. & Tseng, W.-L. A gold nanocluster-based fluorescent probe for simultaneous pH and temperature sensing and its application to cellular imaging and logic gates. *Nanoscale* **8**, 11210–11216 (2016).

195. Sun, J., Yang, F., Zhao, D., Chen, C. & Yang, X. Integrated logic gate for fluorescence turn-on detection of histidine and cysteine based on Ag/Au bimetallic nanoclusters-Cu^{2+} ensemble. *ACS Appl. Mater. Interfaces* **7**, 6860–6866 (2015).

196. Chen, C. *et al.* Logically Regulating Peroxidase-Like Activity of Gold Nanoclusters for Sensing Phosphate-Containing Metabolites and Alkaline Phosphatase Activity. *Anal. Chem.* **91**, 15017–15024 (2019).

197. Milyutin, Y. *et al.* Fabricating and printing chemiresistors based on monolayer-capped metal nanoparticles. *Nat. Protoc.* **16**, 2968–2990

(2021).

198. Yang, X., Yang, L., Dou, Y. & Zhu, S. Synthesis of highly fluorescent lysine-stabilized Au nanoclusters for sensitive and selective detection of Cu2+ ion. *J. Mater. Chem.* **1**, 6748–6751 (2013).
199. Deng, H.-H. *et al.* Methionine-directed fabrication of gold nanoclusters with yellow fluorescent emission for Cu2+ sensing. *Biosensors and Bioelectronics* **65**, 397–403 (2015).
200. Wang, C. *et al.* Protein-directed synthesis of pH-responsive red fluorescent copper nanoclusters and their applications in cellular imaging and catalysis. *Nanoscale* **6**, 1775–1781 (2014).
201. Lee, I. H., Ahn, B., Lee, J. M., Lee, C. S. & Jung, Y. A facile synthesis of fluorescent silver nanoclusters with human ferritin as a synthetic and interfacing ligand. *Analyst* **140**, 3543–3550 (2015).
202. Chen, X., Essner, J. B. & Baker, G. A. Exploring luminescence-based temperature sensing using protein-passivated gold nanoclusters. *Nanoscale* **6**, 9594 (2014).
203. Kajander, T., Cortajarena, A. L., Main, E. R. G., Mochrie, S. G. J. & Regan, L. A new folding paradigm for repeat proteins. *J. Am. Chem. Soc.* **127**, 10188–10190 (2005).
204. Cortajarena, A. L., Mochrie, S. G. J. & Regan, L. Modulating repeat protein stability: The effect of individual helix stability on the collective behavior of the ensemble: Modulating Repeat Protein Stability. *Protein Science* **20**,

1042–1047 (2011).

205. Durgadas, C. V., Sharma, C. P. & Sreenivasan, K. Fluorescent gold clusters as nanosensors for copper ions in live cells. *The Analyst* **136**, 933–940 (2011).

206. Valeur, B. & Berberan-Santos, M. N. *Molecular Fluorescence: Principles and Applications*. (John Wiley & Sons, 2012).

207. Cano, A., Acosta, M. & Arnao, M. B. A method to measure antioxidant activity in organic media: application to lipophilic vitamins. *Redox Rep.* **5**, 365–370 (2000).

208. Wang, L., Ding, L., Wang, Y., Zhang, Y. & Liu, J. Isolation and characterisation of in vitro and cellular free radical scavenging peptides from corn peptide fractions. *Molecules* **20**, 3221–3237 (2015).

209. Jonkman, J., Brown, C. M., Wright, G. D., Anderson, K. I. & North, A. J. Tutorial: guidance for quantitative confocal microscopy. *Nat. Protoc.* **15**, 1585–1611 (2020).

210. Hell, S. W., Dyba, M. & Jakobs, S. Concepts for nanoscale resolution in fluorescence microscopy. *Curr. Opin. Neurobiol.* **14**, 599–609 (2004).

211. Huang, B., Bates, M. & Zhuang, X. Super-Resolution Fluorescence Microscopy. *Annu. Rev. Biochem.* **78**, 993–1016 (2009).

212. Klar, T. A., Jakobs, S., Dyba, M., Egner, A. & Hell, S. W. Fluorescence microscopy with diffraction resolution barrier broken by stimulated emission. *Proc. Natl. Acad. Sci. U. S. A.* **97**, 8206–8210 (2000).

213. Betzig, E. *et al.* Imaging intracellular fluorescent proteins at nanometer resolution. *Science* **313**, 1642–1645 (2006).

214. Rust, M. J., Bates, M. & Zhuang, X. Sub-diffraction-limit imaging by stochastic optical reconstruction microscopy (STORM). *Nat. Methods* **3**, 793–795 (2006).

215. Balzarotti, F. *et al.* Nanometer resolution imaging and tracking of fluorescent molecules with minimal photon fluxes. *Science* **355**, 606–612 (2017).

216. Lorizate, M. *et al.* Super-Resolution Microscopy Using a Bioorthogonal-Based Cholesterol Probe Provides Unprecedented Capabilities for Imaging Nanoscale Lipid Heterogeneity in Living Cells. *Small Methods* **5**, e2100430 (2021).

217. Zessin, P. J. M., Finan, K. & Heilemann, M. Super-resolution fluorescence imaging of chromosomal DNA. *J. Struct. Biol.* **177**, 344–348 (2012).

218. Pereira, C. F., Rossy, J., Owen, D. M., Mak, J. & Gaus, K. HIV taken by STORM: super-resolution fluorescence microscopy of a viral infection. *Virol. J.* **9**, 84 (2012).

219. Holcman, D. *et al.* Single particle trajectories reveal active endoplasmic reticulum luminal flow. *Nat. Cell Biol.* **20**, 1118–1125 (2018).

220. Shao, L., Kner, P., Rego, E. H. & Gustafsson, M. G. L. Super-resolution 3D microscopy of live whole cells using structured illumination. *Nat. Methods* **8**, 1044–1046 (2011).

221. Yannone, S. M., Hartung, S., Menon, A. L., Adams, M. W. W. & Tainer, J. A. Metals in biology: defining metalloproteomes. *Curr. Opin. Biotechnol.* **23**, 89–95 (2012).

222. Wang, C., Zhang, R., Wei, X., Lv, M. & Jiang, Z. Metalloimmunology: The metal ion-controlled immunity. *Adv. Immunol.* **145**, 187–241 (2020).

223. Carter, K. P., Young, A. M. & Palmer, A. E. Fluorescent sensors for measuring metal ions in living systems. *Chem. Rev.* **114**, 4564–4601 (2014).

224. Ko, S.-K., Yang, Y.-K., Tae, J. & Shin, I. In vivo monitoring of mercury ions using a rhodamine-based molecular probe. *J. Am. Chem. Soc.* **128**, 14150–14155 (2006).

225. Domaille, D. W., Que, E. L. & Chang, C. J. Synthetic fluorescent sensors for studying the cell biology of metals. *Nat. Chem. Biol.* **4**, 168–175 (2008).

226. Silver, R. A., Whitaker, M. & Bolsover, S. R. Intracellular ion imaging using fluorescent dyes: artefacts and limits to resolution. *Pflugers Arch.* **420**, 595–602 (1992).

227. Sanchez-Cano, C., Alvarez-Puebla, R. A. & Abendroth, J. M. X-ray-based techniques to study the nano–bio interface. *ACS* (2021).

228. Jeevanandam, J., Barhoum, A., Chan, Y. S., Dufresne, A. & Danquah, M. K. Review on nanoparticles and nanostructured materials: history, sources, toxicity and regulations. *Beilstein J. Nanotechnol.* **9**, 1050–1074 (2018).

229. Kettiger, H., Schipanski, A., Wick, P. & Huwyler, J. Engineered

nanomaterial uptake and tissue distribution: from cell to organism. *Int. J. Nanomedicine* **8**, 3255–3269 (2013).

230. Sanchez-Cano, C. *et al.* X-ray-Based Techniques to Study the Nano-Bio Interface. *ACS Nano* **15**, 3754–3807 (2021).
231. Pushie, M. J., Pickering, I. J., Korbas, M., Hackett, M. J. & George, G. N. Elemental and chemically specific X-ray fluorescence imaging of biological systems. *Chem. Rev.* **114**, 8499–8541 (2014).
232. Hummer, A. A. & Rompel, A. The use of X-ray absorption and synchrotron based micro-X-ray fluorescence spectroscopy to investigate anti-cancer metal compounds in vivo and in vitro. *Metallomics* **5**, 597–614 (2013).
233. Sanchez-Cano, C., Romero-Canelón, I., Geraki, K. & Sadler, P. J. Microfocus x-ray fluorescence mapping of tumour penetration by an organo-osmium anticancer complex. *J. Inorg. Biochem.* **185**, 26–29 (2018).
234. Sanchez-Cano, C. *et al.* Synchrotron X-Ray Fluorescence Nanoprobe Reveals Target Sites for Organo-Osmium Complex in Human Ovarian Cancer Cells. *Chemistry* **23**, 2512–2516 (2017).
235. Matsuyama, S. *et al.* Trace element mapping of a single cell using a hard x-ray nanobeam focused by a Kirkpatrick-Baez mirror system. *Xray Spectrom.* **38**, 89–94 (2009).
236. Martínez-Criado, G. *et al.* ID16B: a hard X-ray nanoprobe beamline at the ESRF for nano-analysis. *J. Synchrotron Radiat.* **23**, 344–352 (2016).
237. Schroer, C. G. *et al.* Hard X-ray nanoprobe at beamline P06 at PETRA III.

Nucl. Instrum. Methods Phys. Res. A **616**, 93–97 (2010).

238. Cesar da Silva, J. *et al.* Efficient concentration of high-energy x-rays for diffraction-limited imaging resolution. *Optica* **4**, 492 (2017).
239. McRae, R., Bagchi, P., Sumalekshmy, S. & Fahrni, C. J. In situ imaging of metals in cells and tissues. *Chem. Rev.* **109**, 4780–4827 (2009).
240. Moore, K. L. *et al.* Combined NanoSIMS and synchrotron X-ray fluorescence reveal distinct cellular and subcellular distribution patterns of trace elements in rice tissues. *New Phytol.* **201**, 104–115 (2014).
241. Domart, F. *et al.* Correlating STED and synchrotron XRF nano-imaging unveils cosegregation of metals and cytoskeleton proteins in dendrites. *Elife* **9**, (2020).
242. Conesa, J. J. *et al.* Unambiguous Intracellular Localization and Quantification of a Potent Iridium Anticancer Compound by Correlative 3D Cryo X-Ray Imaging. *Angew. Chem. Int. Ed Engl.* **59**, 1270–1278 (2020).
243. Deng, J. *et al.* Correlative 3D x-ray fluorescence and ptychographic tomography of frozen-hydrated green algae. *Sci Adv* **4**, eaau4548 (2018).
244. Cagno, S. *et al.* Combined computed nanotomography and nanoscopic X-ray fluorescence imaging of cobalt nanoparticles in Caenorhabditis elegans. *Anal. Chem.* **89**, 11435–11442 (2017).
245. Gallagher-Jones, M. *et al.* Correlative cellular ptychography with functionalized nanoparticles at the Fe L-edge. *Sci. Rep.* **7**, 4757 (2017).
246. Carmona, A. *et al.* SLC30A10 Mutation Involved in Parkinsonism Results in

Manganese Accumulation within Nanovesicles of the Golgi Apparatus. *ACS Chem. Neurosci.* **10**, 599–609 (2019).

247. Yuan, Y. *et al.* Epidermal growth factor receptor targeted nuclear delivery and high-resolution whole cell X-ray imaging of Fe3O4@TiO2 nanoparticles in cancer cells. *ACS Nano* **7**, 10502–10517 (2013).
248. Thurn, K. T. *et al.* Labeling TiO2 nanoparticles with dyes for optical fluorescence microscopy and determination of TiO2-DNA nanoconjugate stability. *Small* **5**, 1318–1325 (2009).
249. Serpell, C. J. *et al.* Carbon nanotubes allow capture of krypton, barium and lead for multichannel biological X-ray fluorescence imaging. *Nat. Commun.* **7**, 13118 (2016).
250. Hostachy, S. *et al.* Graftable SCoMPIs enable the labeling and X-ray fluorescence imaging of proteins. *Chem. Sci.* **9**, 4483–4487 (2018).
251. Castillo-Michel, H. A., Larue, C., Pradas Del Real, A. E., Cotte, M. & Sarret, G. Practical review on the use of synchrotron based micro- and nano- X-ray fluorescence mapping and X-ray absorption spectroscopy to investigate the interactions between plants and engineered nanomaterials. *Plant Physiol. Biochem.* **110**, 13–32 (2017).
252. Victor, T. W. *et al.* Lanthanide-Binding Tags for 3D X-ray Imaging of Proteins in Cells at Nanoscale Resolution. *J. Am. Chem. Soc.* **142**, 2145–2149 (2020).
253. Corezzi, S. *et al.* Synchrotron-based X-ray fluorescence imaging of human

cells labeled with CdSe quantum dots. *Anal. Biochem.* **388**, 33–39 (2009).

254. Cortajarena, A. L., Yi, F. & Regan, L. Designed TPR modules as novel anticancer agents. *ACS Chem. Biol.* **3**, 161–166 (2008).
255. Aires, A. *et al.* Engineering multifunctional metal/protein hybrid nanomaterials as tools for therapeutic intervention and high-sensitivity detection. *Chem. Sci.* **12**, 2480–2487 (2020).
256. Silver, P. A. How proteins enter the nucleus. *Cell* **64**, 489–497 (1991).
257. Ray, M., Tang, R., Jiang, Z. & Rotello, V. M. Quantitative tracking of protein trafficking to the nucleus using cytosolic protein delivery by nanoparticle-stabilized nanocapsules. *Bioconjug. Chem.* **26**, 1004–1007 (2015).
258. Zanta, M. A., Belguise-Valladier, P. & Behr, J. P. Gene delivery: a single nuclear localization signal peptide is sufficient to carry DNA to the cell nucleus. *Proc. Natl. Acad. Sci. U. S. A.* **96**, 91–96 (1999).
259. Li, Z., Wang, Q., Xia, Y., Xun, L. & Liu, H. A Red Fluorescent Protein-Based Probe for Detection of Intracellular Reactive Sulfane Sulfur. *Antioxidants (Basel)* **9**, (2020).
260. Hu, X. *et al.* Developing Polysulfide-Sensitive GFPs for Real-Time Analysis of Polysulfides in Live Cells and Subcellular Organelles. *Anal. Chem.* **91**, 3893–3901 (2019).
261. Capitani, M. & Sallese, M. The KDEL receptor: new functions for an old protein. *FEBS Lett.* **583**, 3863–3871 (2009).
262. Lopez-Martinez, E. *et al.* Tuning the optical properties of Au nanoclusters

by designed proteins. *Adv. Opt. Mater.* **10**, 2101332 (2022).

263. Solé, V. A., Papillon, E., Cotte, M., Walter, P. & Susini, J. A multiplatform code for the analysis of energy-dispersive X-ray fluorescence spectra. *Spectrochim. Acta Part B At. Spectrosc.* **62**, 63–68 (2007).
264. Akishiba, M. *et al.* Cytosolic antibody delivery by lipid-sensitive endosomolytic peptide. *Nat. Chem.* **9**, 751–761 (2017).
265. Piccolino, M. Luigi Galvani and animal electricity: two centuries after the foundation of electrophysiology. *Trends Neurosci.* **20**, 443–448 (1997).
266. Delmar, M. Bioelectricity. *Heart Rhythm* **3**, 114–119 (2006).
267. Kalmijn, A. J., Gonzalez, I. F. & McClune, M. C. The physical nature of life. *J. Physiol. Paris* **96**, 355–362 (2002).
268. Levin, M. Molecular bioelectricity: how endogenous voltage potentials control cell behavior and instruct pattern regulation in vivo. *Mol. Biol. Cell* **25**, 3835–3850 (2014).
269. Borgens, R. B., Vanable, J. W., Jr & Jaffe, L. F. Bioelectricity and regeneration: large currents leave the stumps of regenerating newt limbs. *Proc. Natl. Acad. Sci. U. S. A.* **74**, 4528–4532 (1977).
270. Sundelacruz, S., Li, C., Choi, Y. J., Levin, M. & Kaplan, D. L. Bioelectric modulation of wound healing in a 3D in vitro model of tissue-engineered bone. *Biomaterials* **34**, 6695–6705 (2013).
271. Pitcairn, E. & McLaughlin, K. A. Bioelectric signaling coordinates patterning decisions during embryogenesis. *Trends Dev. Biol.* **9**, 1–9 (2016).

272. Srivastava, P., Kane, A., Harrison, C. & Levin, M. A Meta-Analysis of Bioelectric Data in Cancer, Embryogenesis, and Regeneration. *Bioelectricity* **3**, 42–67 (2021).

273. Pullar, C. E. *The Physiology of Bioelectricity in Development, Tissue Regeneration and Cancer*. (CRC Press, 2016).

274. Silver, B. B. & Nelson, C. M. The Bioelectric Code: Reprogramming Cancer and Aging From the Interface of Mechanical and Chemical Microenvironments. *Front Cell Dev Biol* **6**, 21 (2018).

275. Weisenseel, M. H. & Meyer, A. J. Bioelectricity, gravity and plants. *Planta* **203**, S98-106 (1997).

276. Baluška, F. & Mancuso, S. Ion channels in plants: from bioelectricity, via signaling, to behavioral actions. *Plant Signal. Behav.* **8**, e23009 (2013).

277. Lu, Z. *et al.* Power-generating trees: Direct bioelectricity production from plants with microbial fuel cells. *Appl. Energy* **268**, 115040 (2020).

278. Azri, Y. M., Tou, I., Sadi, M. & Benhabyles, L. Bioelectricity generation from three ornamental plants: Chlorophytum comosum, Chasmanthe floribunda and Papyrus diffusus. *Int. J. Green Energy* **15**, 254–263 (2018).

279. Jeon, E., Baek, S., Choi, S., Park, K. S. & Lee, J. Real-Time Monitoring of Electroconductivity in Plants with Microscale Needle Probes. *Environ. Control. Biol.* **56**, 131–135 (2018).

280. Wellman, N., Fortun, S. M. & McLeod, B. R. Bacterial biofilms and the bioelectric effect. *Antimicrob. Agents Chemother.* **40**, 2012–2014 (1996).

281. Uma Maheswari, R., Mohanapriya, C., Vijay, P., Rajmohan, K. S. & Gopinath, M. Bioelectricity production and desalination of Halomonas sp. – the preliminary integrity approach. *Biofuels* **10**, 355–363 (2019).

282. Wang, L. *et al.* Response characteristics of nitrifying bacteria and Archaea community involved in nitrogen removal and bioelectricity generation in integrated tidal flow constructed wetland-microbial fuel cell. *Front. Microbiol.* **11**, 1385 (2020).

283. Zhao, C. & Liu, Y. Direct Interspecies Electron Transfer Between Archaea and Bacteria. in *Biocommunication of Archaea* (ed. Witzany, G.) 27–40 (Springer International Publishing, 2017).

284. Ohnishi, T. Structural biology: Piston drives a proton pump. *Nature* vol. 465 428–429 (2010).

285. Srivastava, R. The Role of Proton Transfer on Mutations. *Front Chem* **7**, 536 (2019).

286. Weinberg, D. R. *et al.* Proton-coupled electron transfer. *Chem. Rev.* **112**, 4016–4093 (2012).

287. Reece, S. Y. & Nocera, D. G. Proton-coupled electron transfer in biology: results from synergistic studies in natural and model systems. *Annu. Rev. Biochem.* **78**, 673–699 (2009).

288. Berlin, Y. A. & Ratner, M. A. Intra-molecular electron transfer and electric conductance via sequential hopping: Unified theoretical description. *Radiat. Phys. Chem.* **74**, 124–131 (2005).

289. Winkler, J. R. & Gray, H. B. Long-range electron tunneling. *J. Am. Chem. Soc.* **136**, 2930–2939 (2014).

290. Kumar, K. S., Pasula, R. R., Lim, S. & Nijhuis, C. A. Long-Range Tunneling Processes across Ferritin-Based Junctions. *Adv. Mater.* **28**, 1824–1830 (2016).

291. Xin, H. *et al.* Quantum biological tunnel junction for electron transfer imaging in live cells. *Nat. Commun.* **10**, 3245 (2019).

292. Voityuk, A. A. Long-range electron transfer in biomolecules. Tunneling or hopping? *J. Phys. Chem. B* **115**, 12202–12207 (2011).

293. Grozema, F. C., Berlin, Y. A. & Siebbeles, L. D. A. Mechanism of Charge Migration through DNA: Molecular Wire Behavior, Single-Step Tunneling or Hopping? *J. Am. Chem. Soc.* **122**, 10903–10909 (2000).

294. Xiang, L. *et al.* Intermediate tunnelling-hopping regime in DNA charge transport. *Nat. Chem.* **7**, 221–226 (2015).

295. Gray, H. B. & Winkler, J. R. Electron Flow through Proteins. *Chem. Phys. Lett.* **483**, 1–9 (2009).

296. Warren, J. J., Ener, M. E., Vlček, A., Jr, Winkler, J. R. & Gray, H. B. Electron hopping through proteins. *Coord. Chem. Rev.* **256**, 2478–2487 (2012).

297. Zhang, B., Ryan, E., Wang, X., Song, W. & Lindsay, S. Electronic Transport in Molecular Wires of Precisely Controlled Length Built from Modular Proteins. *ACS Nano* (2022) doi:10.1021/acsnano.1c10830.

298. Lindsay, S. Ubiquitous Electron Transport in Non-Electron Transfer Proteins. *Life* **10**, (2020).

299. Ing, N. L., El-Naggar, M. Y. & Hochbaum, A. I. Going the Distance: Long-Range Conductivity in Protein and Peptide Bioelectronic Materials. *J. Phys. Chem. B* **122**, 10403–10423 (2018).

300. Gray, H. B. & Winkler, J. R. Long-range electron transfer. *Proc. Natl. Acad. Sci. U. S. A.* **102**, 3534–3539 (2005).

301. Cordes, M. & Giese, B. Electron transfer in peptides and proteins. *Chem. Soc. Rev.* **38**, 892–901 (2009).

302. Gray, H. B. & Winkler, J. R. Electron tunneling through proteins. *Q. Rev. Biophys.* **36**, 341–372 (2003).

303. Skourtis, S. S., Balabin, I. A., Kawatsu, T. & Beratan, D. N. Protein dynamics and electron transfer: electronic decoherence and non-Condon effects. *Proc. Natl. Acad. Sci. U. S. A.* **102**, 3552–3557 (2005).

304. Blumberger, J. Recent Advances in the Theory and Molecular Simulation of Biological Electron Transfer Reactions. *Chem. Rev.* **115**, 11191–11238 (2015).

305. Ordinario, D. D. *et al.* Bulk protonic conductivity in a cephalopod structural protein. *Nat. Chem.* **6**, 596–602 (2014).

306. Glasser, L. Proton conduction and injection in solids. *Chem. Rev.* **75**, 21–65 (1975).

307. Silberbush, O., Amit, M., Roy, S. & Ashkenasy, N. Significant enhancement

of proton transport in bioinspired peptide fibrils by single acidic or basic amino acid mutation. *Adv. Funct. Mater.* **27**, 1604624 (2017).

308. Amit, M. *et al.* Hybrid proton and electron transport in peptide fibrils. *Adv. Funct. Mater.* **24**, 5873–5880 (2014).
309. Zhang, J., Zhou, K., Zhang, Y., Du, M. & Wang, Q. Precise Self-Assembly of Nanoparticles into Ordered Nanoarchitectures Directed by Tobacco Mosaic Virus Coat Protein. *Adv. Mater.* **31**, e1901485 (2019).
310. Carloni, P., Andreoni, W. & Parrinello, M. Self-Assembled Peptide Nanotubes from First Principles. *Phys. Rev. Lett.* **79**, 761–764 (1997).
311. Jishi, R. A., Braier, N. C., White, C. T. & Mintmire, J. W. Peptide nanotubes: An inert environment. *Phys. Rev. B Condens. Matter* **58**, R16009–R16011 (1998).
312. Lee, J. S. *et al.* Self-assembly of semiconducting photoluminescent peptide nanowires in the vapor phase. *Angew. Chem. Int. Ed Engl.* **50**, 1164–1167 (2011).
313. Akdim, B., Pachter, R. & Naik, R. R. Self-assembled peptide nanotubes as electronic materials: An evaluation from first-principles calculations. *Appl. Phys. Lett.* **106**, 183707 (2015).
314. Moser, C. C., Chobot, S. E., Page, C. C. & Dutton, P. L. Distance metrics for heme protein electron tunneling. *Biochim. Biophys. Acta* **1777**, 1032–1037 (2008).
315. Ron, I., Pecht, I., Sheves, M. & Cahen, D. Proteins as solid-state electronic

conductors. *Acc. Chem. Res.* **43**, 945–953 (2010).

316. Ron, I. *et al.* Proteins as electronic materials: electron transport through solid-state protein monolayer junctions. *J. Am. Chem. Soc.* **132**, 4131–4140 (2010).
317. Shi, Z., Phillips, G. O. & Yang, G. Nanocellulose electroconductive composites. *Nanoscale* **5**, 3194–3201 (2013).
318. Shateri-Khalilabad, M. & Yazdanshenas, M. E. Preparation of superhydrophobic electroconductive graphene-coated cotton cellulose. *Cellulose* **20**, 963–972 (2013).
319. Han, T. H. *et al.* Peptide/graphene hybrid assembly into core/shell nanowires. *Adv. Mater.* **22**, 2060–2064 (2010).
320. Mosa, I. M. *et al.* Ultrathin Graphene-Protein Supercapacitors for Miniaturized Bioelectronics. *Adv Energy Mater* **7**, (2017).
321. Kiyotake, E. A., Martin, M. D. & Detamore, M. S. Regenerative rehabilitation with conductive biomaterials for spinal cord injury. *Acta Biomater.* **139**, 43–64 (2022).
322. Dong, R., Ma, P. X. & Guo, B. Conductive biomaterials for muscle tissue engineering. *Biomaterials* **229**, 119584 (2020).
323. Green, R. A. *et al.* Conductive hydrogels: mechanically robust hybrids for use as biomaterials. *Macromol. Biosci.* **12**, 494–501 (2012).
324. Dominguez-Alfaro, A. *et al.* Tailored Methodology Based on Vapor Phase Polymerization to Manufacture PEDOT/CNT Scaffolds for Tissue

Engineering. *ACS Biomater Sci Eng* **6**, 1269–1278 (2020).

325. Braun, G. *et al.* Gold nanoparticle decoration of DNA on silicon. *Langmuir* **21**, 10699–10701 (2005).
326. Baei, P. *et al.* Electrically conductive gold nanoparticle-chitosan thermosensitive hydrogels for cardiac tissue engineering. *Mater. Sci. Eng. C Mater. Biol. Appl.* **63**, 131–141 (2016).
327. Shevach, M., Fleischer, S., Shapira, A. & Dvir, T. Gold nanoparticle-decellularized matrix hybrids for cardiac tissue engineering. *Nano Lett.* **14**, 5792–5796 (2014).
328. Ranjana, R. *et al.* Fabrication and characterization of conductive silk fibroin–gold nanocomposite films. *J. Mater. Sci.: Mater. Electron.* **31**, 249–264 (2020).
329. Mejias, S. H., Aires, A., Couleaud, P. & Cortajarena, A. L. Designed Repeat Proteins as Building Blocks for Nanofabrication. in *Protein-based Engineered Nanostructures* (eds. Cortajarena, A. L. & Grove, T. Z.) vol. 940 61–81 (Springer International Publishing, 2016).
330. Behrens, S., Habicht, W., Wagner, K. & Unger, E. Assembly of nanoparticle ring structures based on protein templates. *Adv. Mater.* **18**, 284–289 (2006).
331. Chen, C.-L., Zhang, P. & Rosi, N. L. A new peptide-based method for the design and synthesis of nanoparticle superstructures: construction of highly ordered gold nanoparticle double helices. *J. Am. Chem. Soc.* **130**, 13555–

13557 (2008).

332. Grove, T. Z., Regan, L. & Cortajarena, A. L. Nanostructured functional films from engineered repeat proteins. *J. R. Soc. Interface* **10**, 20130051 (2013).
333. Carter, N. A. & Grove, T. Z. Protein Self-Assemblies That Can Generate, Hold, and Discharge Electric Potential in Response to Changes in Relative Humidity. *J. Am. Chem. Soc.* **140**, 7144–7151 (2018).
334. Carter, N. A. & Grove, T. Z. Functional protein materials: beyond elastomeric and structural proteins. *Polym. Chem.* **10**, 2952–2959 (2019).
335. Abad, J. M., Gass, M., Bleloch, A. & Schiffrin, D. J. Direct electron transfer to a metalloenzyme redox center coordinated to a monolayer-protected cluster. *J. Am. Chem. Soc.* **131**, 10229–10236 (2009).
336. Jensen, P. S. *et al.* Gold Nanoparticle Assisted Assembly of a Heme Protein for Enhancement of Long-Range Interfacial Electron Transfer. *J. Phys. Chem. C* **111**, 6124–6132 (2007).
337. Guterman, T. *et al.* Electrical Conductivity, Selective Adhesion, and Biocompatibility in Bacteria-Inspired Peptide-Metal Self-Supporting Nanocomposites. *Adv. Mater.* **31**, e1807285 (2019).
338. Pena-Francesch, A. *et al.* Programmable Proton Conduction in Stretchable and Self-Healing Proteins. *Chem. Mater.* **30**, 898–905 (2018).
339. Cohen, S. S. *et al.* Probing the Molecular Origin of Native-State Flexibility in Repeat Proteins. *J. Am. Chem. Soc.* **137**, 10367–10373 (2015).
340. Lu, Y. & Chen, W. Sub-nanometre sized metal clusters: from synthetic

challenges to the unique property discoveries. *Chem. Soc. Rev.* **41**, 3594–3623 (2012).

341. Gilbert, M. & Albinsson, B. Photoinduced charge and energy transfer in molecular wires. *Chem. Soc. Rev.* **44**, 845–862 (2015).
342. Li, C., Xu, C., Cahen, D. & Jin, Y. Unprecedented efficient electron transport across Au nanoparticles with up to 25-nm insulating SiO2-shells. *Sci. Rep.* **9**, 18336 (2019).
343. Carter, N. A. & Grove, T. Z. Repeat-proteins films exhibit hierarchical anisotropic mechanical properties. *Biomacromolecules* **16**, 706–714 (2015).
344. González, M. T. *et al.* Stability of single- and few-molecule junctions of conjugated diamines. *J. Am. Chem. Soc.* **135**, 5420–5426 (2013).
345. Pérez-Juste, J., Liz-Marzán, L. M., Carnie, S., Chan, D. Y. C. & Mulvaney, P. Electric-field-directed growth of gold nanorods in aqueous surfactant solutions. *Adv. Funct. Mater.* **14**, 571–579 (2004).
346. Pace, C. N., Vajdos, F., Fee, L., Grimsley, G. & Gray, T. How to measure and predict the molar absorption coefficient of a protein. *Protein Sci.* **4**, 2411–2423 (1995).
347. Liu, X., Atwater, M., Wang, J. & Huo, Q. Extinction coefficient of gold nanoparticles with different sizes and different capping ligands. *Colloids Surf. B Biointerfaces* **58**, 3–7 (2007).

8.ACKNOWLEDGEMENTS

First and foremost, I would like to thank Prof. Aitziber L. Cortajarena and Dr. Carlos Sánchez-Cano for their support, patience, and advice. I am very grateful for all these years under your supervision and all the opportunities to learn, grow and share with you. Your commitment to boosting and diversifying different aspects of my early career is truly appreciated.

Second, I'm very grateful to all the great people working at the Biomolecular Nanotechnology Lab and former members. Especially to Antonio, Sara, and Dani, 'la vieja guardia de Madrid'; all people from whom I learned a lot since the very beginning of my master's period. I always think of you guys when my motivation needs a little boost. I want to thank all the members, postdocs and students alike, for their scientific and emotional support, especially Idoia, Laura M, Laura P, Kepa, Aitor, Max, Liher, Dina, Edu, Antonio D and Gunnar.

I'm also really thankful to all the people working in CIC biomaGUNE, from platform managers, technicians, maintenance, to admin employers. Your work is key to advancing experiments and making the workplace functional and enjoyable.

Finally, I would like to thank my loved ones, family and friends, for all your kindness, patience and support. I will need personal time with you to thank you properly. This adventure was also possible because you pushed me when I couldn´t move. I'm especially thankful to my parents, Pilar and Juanma, my partner in life Alex, my friends from The Fellowship of the Beer and the friends I met in Donosti. Thank you, a lot.

CIC biomaGUNE

CENTER FOR COOPERATIVE RESEARCH IN BIOMATERIALS

eman ta zabal zazu

Universidad del País Vasco

Euskal Herriko Unibertsitatea